

Technische Universität München

Department Chemie

Fachgebiet Theoretische Chemie

**Theoretical Studies of
Catalytic Transformations
of Hydrocarbons over Transition Metals**

Duygu Başaran

Vollständiger Abdruck der von der Fakultät für Chemie der Technischen Universität München zur Erlangung des akademischen Grades eines

Doktors der Naturwissenschaften (Dr. rer. nat.)

genehmigten Dissertation.

Vorsitzender: **Univ.-Prof. Dr. M. Nest**

Prüfer der Dissertation:

1. Univ.-Prof. Dr. Dr. h.c. N. Rösch (i. R.)

2. Univ.-Prof. Dr. K. Köhler

Die Dissertation wurde am 24.06.2013 bei der Technischen Universität München eingereicht und durch die Fakultät für Chemie am 11.07.2013 angenommen.

Acknowledgments

I would like to express my gratitude to my doctoral thesis supervisor, my Doktorvater, Prof. Dr. Dr. h.c. N. Rösch. I thank him for the opportunity he provided me to perform my doctoral studies in his research group. I value his insightful suggestions and generous help throughout the research and writing periods of this thesis very much.

I am thankful to Dr. A. Genest, whose guidance helped me shape my research project and who assisted me even from Singapore, through every communication device in possession. I thank Dr. S Krüger who has always been there from the first moment to reply all my scientific and administrative questions. I am also grateful to Ass. Prof. Dr. H. Aleksandrov for assisting me during the earlier years of my research and teaching me how to handle the problems from the first moment. I thank my heterogeneous catalysis comrades, Dr. Z.-J. Zhao and C.-c. Chiu, not only for the discussions that stimulated new research and new calculations but also for the entertaining times during the conferences. I would like to thank my office mate Dr. A. Nikodem for both the company and the scientific help she provided. I also thank Dr. M. Häberle, Dr. A. Mirescu, B. Asam, E. Wurm, R. Mösch, and A. Meinel for their help in many administrative issues I encountered.

The past and present members of this group made coming to work every day the last five years a pleasure with the interesting discussions and the pleasant environment they provided; I thank Dr. A. Matveev, Dr. V. Karttunen, T. Soini, Dr. W. Eger, Dr. I. Chiorescu, Y. Wu, Dr. K. Damianos, B. Li, Dr. R.S. Ray, Dr. R. Ramakrishnan, S. Parker, Dr. J. Santana, Dr. B. Martorell, Dr. E. Vladimirov and Dr. R. Marchal.

I am especially thankful to my not-yet-mentioned colleague but more importantly my very talented friend Dr. Alena Kremleva for her presence. I thank Michael Banck and Daniel Opalka for the traditional Friday nights, and their extensions to the other days. I am grateful to Dominic Schupke for his support and help in keeping me sane, especially during the last times of this work. I also thank Moritz Kiese for his infinite wisdom in infinite topics that distracted me during tough times.

Without the love and the support of my family, none of this would have been possible. I look up to you and try to deserve everything you provide me with. I am indebted to you.

To my parents...

TABLE OF CONTENTS

| | | |
|------|--|----|
| I. | Introduction | 1 |
| II. | Computational Details and Models | 5 |
| 1. | Computational details | 5 |
| 2. | Modeling of the aqueous phase | 8 |
| III. | PART I - Comparative Study of Ethylene Decomposition on Close-Packed Surfaces of Transition Metals | 11 |
| 3. | Background | 11 |
| 4. | Systematic decomposition of ethylene | 14 |
| 4.1. | Adsorption Complexes and Energetics of the Intermediates | 14 |
| 4.2. | Reaction energetics for decomposition of ethylene C ₂ H ₄ over M(111) (M = Pt, Pd, Rh, Ni) | 25 |
| 5. | Discussion | 36 |
| 5.1. | Binding energies | 36 |
| 5.2. | Barriers and reaction energies | 40 |
| 5.3. | Relationship between reaction energies and activation barriers | 43 |
| 5.4. | Coverage effect | 45 |
| 5.5. | Limitations of the models used | 45 |
| 6. | Conclusions | 46 |
| IV. | PART II - Conversion of Simple Alcohols on Platinum Surfaces | 49 |
| 7. | The choice of hydrogen as an energy carrier | 49 |
| 7.1. | Chemical background on hydrogen production | 49 |
| 7.2. | Hydrogen from biomass via aqueous phase reforming (APR) | 55 |
| 8. | Dehydrogenation of 1- and 2-propanol | 60 |
| 8.1. | Adsorption complexes | 60 |
| 8.2. | Reactions | 67 |
| 8.3. | Aqueous medium modeling | 75 |

| | | |
|-----------------------------------|--|-----|
| 8.4. | Conclusions on the dehydrogenation behavior of 1- and 2-propanol | 79 |
| 9. | Conversion of propionyl to CO ₂ and ethane | 80 |
| 9.1. | Adsorption complexes on the flat (111) and on the stepped (221) surfaces | 82 |
| 9.2. | Reactions | 94 |
| 9.3. | Overview over the reaction pathways | 112 |
| V. | Summary | 127 |
| APPENDIX A: Microkinetic modeling | | 131 |
| References | | 133 |

LIST OF ABBREVIATIONS

| | |
|--------|---|
| APR | Aqueous phase reforming |
| BE | Binding energy |
| BEP | Brønsted – Evans – Polanyi |
| DFT | Density functional theory |
| FS | Final state |
| GGA | Generalized gradient approximation |
| HREELS | High resolution electron energy loss spectroscopy |
| IS | Initial state |
| kMC | Kinetic Monte Carlo |
| LEED | Low-energy electron diffraction |
| M | Metal |
| Me | Methyl group, CH ₃ |
| NEXAFS | Near-edge X-ray absorption fine structure |
| SR | Steam reforming |
| TPD | Temperature programmed desorption |
| TS | Transition state |
| WGS | Water-gas shift |
| WS | Water splitting |
| XPS | X-ray photoelectron spectroscopy |
| ZPE | Zero point energy |

I. INTRODUCTION

The energy consumption has been increasing every year by 2.6% on average since 1965.¹ The average consumption in the last ten years increased at almost the same rate (2.7%), however at the same period, 2001-2011, the fossil fuel production increased 2.2% yearly on average. Recent models predict that the reserves for oil, gas and coal will be depleted in 2040, 2042 and 2112, respectively.² One should also consider the changes in price of the fossil-based fuels, which may occur very abruptly for several reasons, including political instabilities in the major production countries or regions and the fact that the production limit is almost reached, making it harder to compensate production fluctuations. The financial crisis in 2008 caused a slight decrease in the energy consumption in 2009, which was compensated with an increase of ~5.1% in 2010. In 2011, 87% of the primary energy consumption was supplied from oil, natural gas and coal, while renewables (i.e., wind, solar, geothermal, biomass and waste) only accounted for 1.6% of energy consumption, see Figure I.1 for the distribution of energy sources in 2010 and 2011.¹ In 2011 Germany ranked fifth in the world in renewable energy consumption per person;^{3,4} 10.9% of 13354 PJ energy consumption was supplied through renewable sources listed above.⁵ Through the use of renewables Germany saved ~1516 PJ of primary energy on fossil fuels and transportation costs combined in 2010.⁶ Among renewables, the role of biomass is increasing in importance as a clean energy source, even claimed as the only sustainable source of organic fuels, chemicals and materials as the net carbon emission to the atmosphere is decreased via planting new feedstock.⁷

Until the fossil-fuel based, i.e., coal dependent industrial revolution in the 18th century, biomass based organic fuels were the dominant energy source of the world, solely via burning the plant biomass directly.⁸ The introduction of fossil fuels decreased the use of biofuels until after the World War II; but with the increase in the population along with the increase of energy consumption per person in the after-war era, the demand for energy increased, causing different energy sources such as biomass to be investigated. New routes were introduced to replace the direct combustion method, which produces heat with a limited efficiency as the energy density of biomass raw material is very low compared to crude oil; the energy density of dry wood is highest among many biomass resources but it is still only 40% of that of crude oil.⁹ Thermochemical routes such as pyrolysis and gasification convert the biomass into gas or liquid fuels, to be used further in energy generation. Chemical routes such as hydrolysis of fats produce biodiesel, and bacteria, enzymes and yeasts take part in the

biochemical route to convert sugar-based biomass into gaseous and liquid fuels.¹⁰ The listed methods are used excessively in the industry nowadays; however the efficiency of the processes is not satisfactory.¹¹ Thus, increasing the efficiency of biomass conversion processes is a high priority to maximize the benefits and to minimize the ecosystem and societal costs.¹²

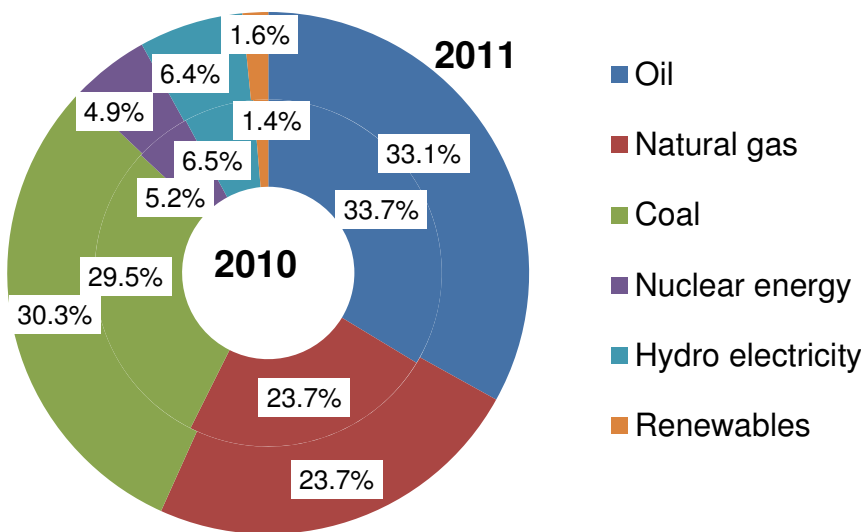


Figure I.1 Primary energy consumption distribution to energy types in 2010 and 2011, inside and outside the ring, respectively. Adapted from Ref. 1.

Hydrogen is an attractive energy carrier that produces only water as end-product. However the current widespread production processes rely heavily on nonrenewable natural gas or other petroleum products,¹³ the reserves of which are limited. Other possibilities of H₂ production are water splitting and using biomass feedstock for conversion. Biomass conversion to hydrogen includes: directly from gasification coupled by water-gas shift (WGS), conversion of biomass in aqueous phase at high temperatures and pressures,¹⁴ pyrolysis, biochemical conversion, or indirectly from biomass-derived pyrolysis oils, methanol, and ethanol.¹⁵ These methods listed have shortcomings; they have too low production rates or too many complex steps during the production that makes researchers look for feasible novel processes that overcome the efficiency and cost issues.

Recently Dumesic et al. introduced the aqueous phase reforming (APR) process as an efficient method for converting carbohydrates produced from biomass, such as sugars and polyols, into primarily H₂ and CO₂.¹⁶ The process occurs at temperatures ~500 K and pressures typically ~15–50 bar. The reaction conditions are also suitable for the WGS reaction, which enables generation of H₂ with less CO content in a single reactor. The lower temperatures in comparison to steam reforming, which is currently the most prominent

process for H₂ production, decrease the probability of any side reactions the carbohydrates may undergo. The reaction is easier to control and is said to have a lower energy requirement as the effluent does not need to be vaporized.¹⁷ The listed major advantages of APR processing over steam reforming of alkanes make this process a feasible alternative for H₂ production. The selectivity is a major issue as the main products of the process, H₂ and CO₂, tend to form methane at the reaction conditions. Hence the examination of the detailed reaction routes on various catalysts to find the most appropriate one is of great importance, appealing both to experimentalists and theoreticians.

Before investigating a complex system consisting of several reactions and side reactions, including C–C and C–H bond scissions, a detailed understanding of a simpler system that consists of only dehydrogenation reactions of ethylene on the close-packed (111) surfaces of several different transition metals, i.e., Pt, Pd, Rh and Ni, was investigated in the first part of the thesis, namely a comparative study of ethylene decomposition on close-packed surfaces of transition metals. A systematic decomposition of ethylene, comprising of four dehydrogenation reactions and a C–C bond scission of the final H-free C₂ structure, is employed to understand how different these metals perform thermodynamically and kinetically under the same conditions. The reactions studied are of relevance in several processes, e.g., ethylene conversion to ethylidyne,^{18–22} hydrogenation of acetylene,²³ and graphene formation from C atoms.²⁴

In the second part of the thesis the conversion of simple alcohols to produce H₂ was studied to exemplify the conversion of biomass feedstock on two surfaces of Pt, the flat Pt(111) surface and the stepped Pt(221) surface. 1- and 2- propanol were used as alcohol feedstock as they are simple candidates that show the selectivity of catalytic processes. These studies provide a first insight into reactions of sugars and lead to results that might be extendable to polyols. The conversion route is divided into two parts. One part solely comprises dehydrogenation reactions that are expected to take place before C–C bond scission reactions based on previous studies.²² Afterwards C–C bond breaking reactions were addressed to answer the question whether the decarbonylation or the decarboxylation is the dominating mechanism of deoxygenation.²⁵

II. COMPUTATIONAL DETAILS AND MODELS

1. Computational details

Periodical slab calculations were performed with a plane-wave based technology as implemented in Vienna Ab initio Simulation Package (VASP) to solve the Kohn-Sham equation of density functional theory (DFT).²⁶⁻²⁹ The projector augmented wave (PAW) method^{30,31} was employed to describe the interactions between the electrons and ions. The gradient corrected form (generalized gradient approximation – GGA) of the exchange and correlation functional was employed as suggested by Perdew and Wang (PW91).^{32,33} Plane waves up to a kinetic energy of 400 eV were included in the basis set. The Brillouin zone was sampled by a $5 \times 5 \times 1$ k points Monkhorst-Pack grid³⁴ along with first-order Methfessel–Paxton smearing³⁵ with a 0.15 smearing width to accelerate the convergence; energies extrapolated to no smearing were used. The calculations were performed spin-polarized for the Ni(111) surface and the gas phase open-shell species. In all other cases, non-spin-polarized calculations were carried out.

The surfaces of M = Pt, Pd, Rh, and Ni were modeled in a supercell geometry by slab models periodic in two dimensions and repeated in the third dimension, separated with a vacuum spacing of at least 1 nm between two slabs, lying in the direction of the surface normal vector to prevent interaction. The flat surfaces of M(111) were modeled by slabs of four layers in the ethylene decomposition study, and by slabs of five layers in the alcohol conversion part. Stepped Pt(221) surfaces were also employed in the alcohol conversion studies. The (221) surface of Pt comprises of (111) terraces, four atomic rows wide, connected by (111) steps of monatomic height. Formally, these surfaces were modeled as 20 mathematical layers in 221 direction, which makes up five physical layers in [111] direction. The adsorbates were placed on one side of the slab models and dipole corrections were employed as implemented in VASP.³⁶ The adsorbates and the first two “upper” layers of the surfaces (eight mathematical layers in 221 direction in the case of the stepped surface) were relaxed during geometry optimizations and transition state searches. The two/three “bottom” layers of (111) terraces were kept fixed at their theoretically calculated bulk-terminated geometries where the distances between M–M atoms are 282, 280, 272 and 248 pm for Pt, Pd, Rh and Ni, respectively. The atoms were allowed to relax so that the forces acting on them in each direction were less than 2×10^{-4} eV/pm. Three coverages were investigated regarding the adsorption of the hydrocarbon species in the ethylene decomposition study; a $(\sqrt{3} \times \sqrt{3})R30^\circ$ unit cell for 1/3 coverage, a (2×2) unit cell for 1/4 coverage and a (3×3) unit

cell for 1/9 coverage, as shown in Figure 1.1. The reactions were investigated on the lowest coverage, 1/9. The shortest lateral distances at this coverage between two structures in adjacent cells are 478 pm in the ethylene decomposition part and 394 pm in the alcohol conversion part. In alcohol conversion study only one coverage, 1/9 represented by the same (3×3) unit cell, was considered on the flat surface and the stepped surface is modeled as a (3×1) unit cell, corresponding to 1/12 coverage, Figure 1.1. The energies and geometries of gas phase species are calculated in a cubic box with dimensions of $1.5 \times 1.5 \times 1.5$ nm³. A single k-point was used for all calculations on isolated molecular species and spin polarization

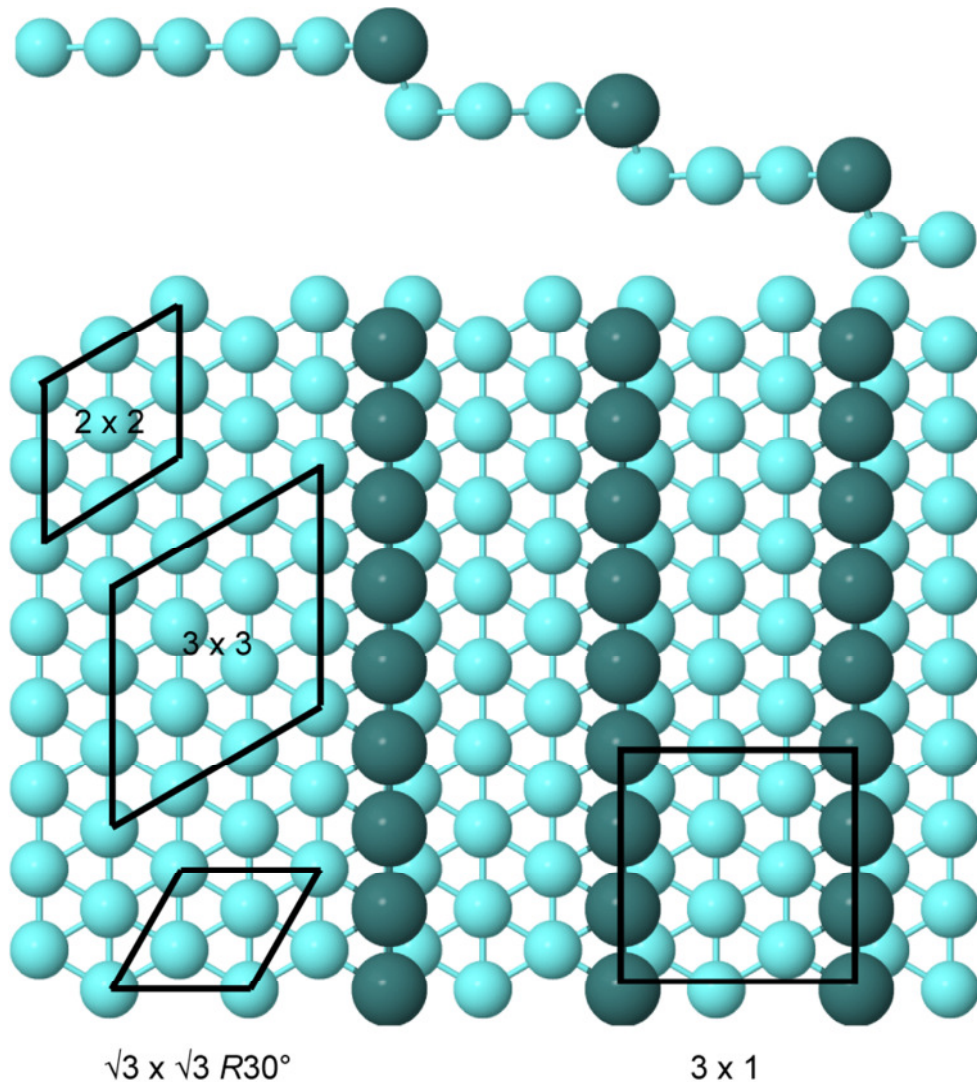


Figure 1.1 Three different coverages employed on the flat (111) surfaces of M (M = Pt, Pd, Rh, Ni): $\sqrt{3} \times \sqrt{3}$ unit cell for 1/3 coverage, a 2×2 unit cell for 1/4 coverage and a 3×3 unit cell for 1/9 coverage, represented together with the coverage employed stepped surface (221) a 3×1 unit cell for 1/12 coverage. The step-edge atoms are represented with a bigger radius to facilitate the separation.

was employed in the case of radical species.

Binding energies (BE) were calculated as $\text{BE} = E_{\text{ad}} + E_{\text{sub}} - E_{\text{ad/sub}}$, where E_{ad} is the total energy of the adsorbate in the gas phase (ground state), E_{sub} is the total energy of the clean surface, and $E_{\text{ad/sub}}$ is the total energy of the adsorbate on the surface in the optimized geometry. With this definition of the binding energy, positive values imply a favorable interaction, i.e., a release in energy upon adsorption.

Reaction energies E_r were calculated as the change of total energies when the reactant structure is converted to the final structure, if there are more than one species in any of the said structures they are taken to be in close proximity; $E_r(\mathbf{r}_1+\mathbf{r}_2 \rightarrow \mathbf{p}_1+\mathbf{p}_2) = E([\mathbf{p}_1+\mathbf{p}_2]/M) - E_r([\mathbf{r}_1+\mathbf{r}_2]/M)$. In addition to the reaction energies calculated in this way, the reaction energies were determined for the species in structures formally at “infinite separation”. As in infinite separation there will be no lateral interactions with the other species, the change in the total energies of each individual species was taken as reference; $E_r^{\text{inf}} = [E(\mathbf{p}_1)/M + E(\mathbf{p}_2)/M - E(M)] - [E(\mathbf{r}_1)/M + E(\mathbf{r}_2)/M - E(M)]$. The presence of the energy of the surface, $E(M)$, in this equation is to keep the number of surfaces on both sides of the equation equal, e.g., if there are two products adsorbed on the surface but only one reactant species adsorbed on the surface, the clean surface is actually the second reactant, “latent reactant”. Activation energies were calculated as the difference between total energies of transition and initial states; $E_a = E(\text{TS})/M - E([\mathbf{p}_1+\mathbf{p}_2]/M)$.

Transition states (TSs) were located by employing the dimer method³⁷ and the nudged elastic band (NEB)^{38,39} method. In the latter case, eight images were generated in between the reactant and the product states to represent a discrete approximation to a reaction path. An estimate to a transition state was thus found. Afterwards, the estimated TS was used as a starting point for a refinement with the “dimer” method. The transition state structures were refined until the forces on atomic centers were at most 2×10^{-4} eV/pm, as in the case of minima search, i.e., for the intermediates. The vibrational analysis was carried out for each stationary point, in order to confirm that there are no imaginary frequencies in the case of intermediates and there is exactly one imaginary frequency that corresponds to the breaking or forming of the bonds of interest in the case of TS structures. The energies were not corrected to zero point energies (ZPE); ~~or~~ the calculations on Pd(111) had shown that the effect on the barriers is only a reduction by $\sim 10\text{--}15$ kJ mol⁻¹ for C–H bond breaking and $\sim 5\text{--}8$ kJ mol⁻¹ for C–C bond breaking reactions.²² For C–H reactions on Rh(111) Li et al.¹⁹ estimated at most 18 kJ mol⁻¹ reduction in the barriers and on Ni(111) Nave et al.⁴⁰ reported $\sim 10\text{--}14$ kJ mol⁻¹ corrections for the zero point energy.

2. Modeling of the aqueous phase

When modeling systems in an aqueous environment, a simpler slab model was employed. The (111) surface of Pt was modeled in a supercell geometry as two-layer slab with a spacing of at least 1 nm in-between two slabs. The relaxation was applied only for the adsorbates; the Pt atoms were kept fixed at their theoretically calculated bulk-terminated geometries. For systems in the gas phase, this simple model provides adequate results for the BE values of the intermediates. The BE values of the structures calculated in this way differ at most by 10 kJ mol⁻¹ from the corresponding values obtained by the more elaborate model described in Chapter 1.

The aqueous phase over the metal surface was modeled as one layer of water molecules. The number of water molecules in one layer was determined using molecular dynamics calculations in VASP. The spacing between two slabs was filled with 24 water molecules according to density of water ($\sim 1 \text{ g/cm}^3$). The system was structurally relaxed using a microcanonical ensemble at 300 K for 1 ps. Afterwards the system was cooled down to 0 K in ~ 3 ps via simulated annealing. From the resulting structure it was concluded that there are eight water molecules in the first layer at the 3×3 unit cell. The resulting surface

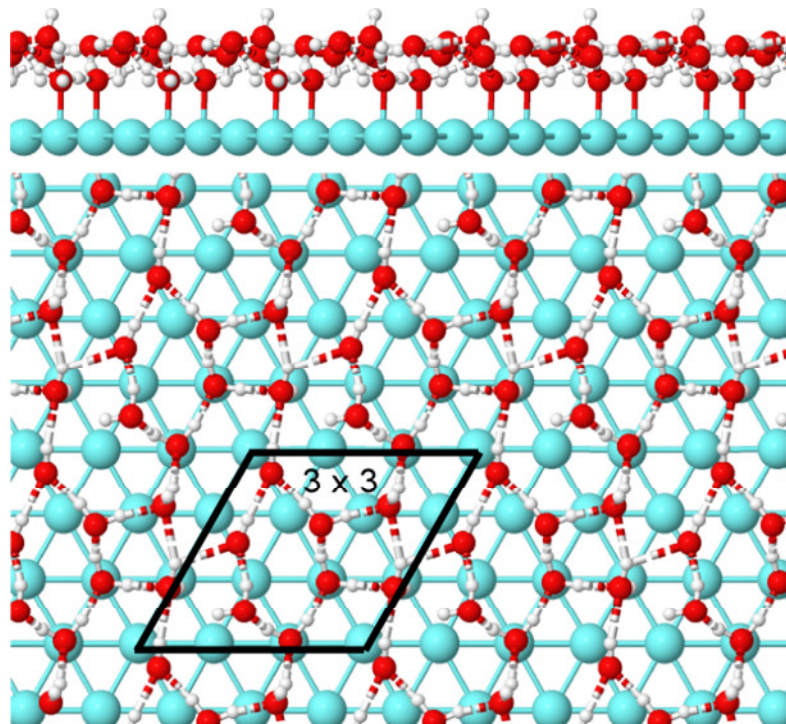


Figure 2.1 Top and side views of the water network forming over the surface formed from eight water molecules. Hydrogen bonds in between the water molecules are also represented. The 3×3 unit cell employed is marked.

along with the eight water molecules was optimized further with the criteria presented in computational details and is displayed in Figure 2.1. The structure of the water layer has an average O–O bond length of 285.5 pm, which is the same as the value determined from X-ray radial distribution function for liquid water structure.⁴¹

III. PART I - COMPARATIVE STUDY OF ETHYLENE DECOMPOSITION ON CLOSE-PACKED SURFACES OF TRANSITION METALS

3. Background

Olefins constitute an important class of organic compounds with a wide range of applications in petrochemistry, organic and polymer chemistry due to their high reactivity and the diversity of valuable products.⁴² At an industrial scale, transformations of olefins usually occur on transition metal catalysts; therefore research has focused on understanding the interaction of alkenes at transition metal surfaces.⁴³ As the first member of the unsaturated hydrocarbon series, ethylene has received a fair share of attention, from both experimentalists and theoreticians about its interaction with several transition metal surfaces.^{18,43-55} Especially dehydrogenation-hydrogenation reactions are of great interest in petroleum industry in the production of ethane and acetylene.⁵⁶⁻⁶⁰

The discussion of the adsorption mode of ethylene on transition metals has been a hot topic for many years.⁶¹⁻⁶⁸ Two adsorption modes have been observed: a π adsorbed mode that undergoes hydrogenation,^{60,69} and a more stable di- σ adsorbed mode.^{18,19,70,71} However, more recently, a study by Okada et al.⁷² found that on the Pt(111) surface both forms coexist and interconvert easily. These authors also suggested an explanation for the fact that Cremer et al.⁶⁹ observed only the π adsorbed mode under hydrogenation conditions; accordingly, di- σ adsorbed ethylene is quickly removed from the surface through hydrogenation.

Ethylene that is adsorbed on transition metal surfaces may undergo several conversions as dehydrogenation, hydrogenation, 1,2-hydrogen shift and C–C scission. A schematic of the complex reaction network comprising such reactions is represented in the work by Chen et al., Figure 3.1.²² As the individual steps of conversions are hard to be determined through experiments, it is a widely employed strategy to examine via computational methods the probable networks that include observed intermediates and products. For example, ethylene has been previously studied computationally on Pt(111),^{21,73,74} Pd(111),^{18,20,22,56,70,71,75,76} Rh(111),¹⁹ and Ni(111)⁵⁵ surfaces. Chen et al.²² presented the intermediates and transition states of the complete network of ethylene conversion on Pd(111) surface from computational results. These results suggested C–C bond breaking reactions over the metal to have mostly higher barriers than C–H bond breaking reactions. Only species with minor H content, ethynyl (CHC), and carbon dimer (C₂), have comparable/lower activation barriers for the cleavage of the C–C bond. Hence, the likely

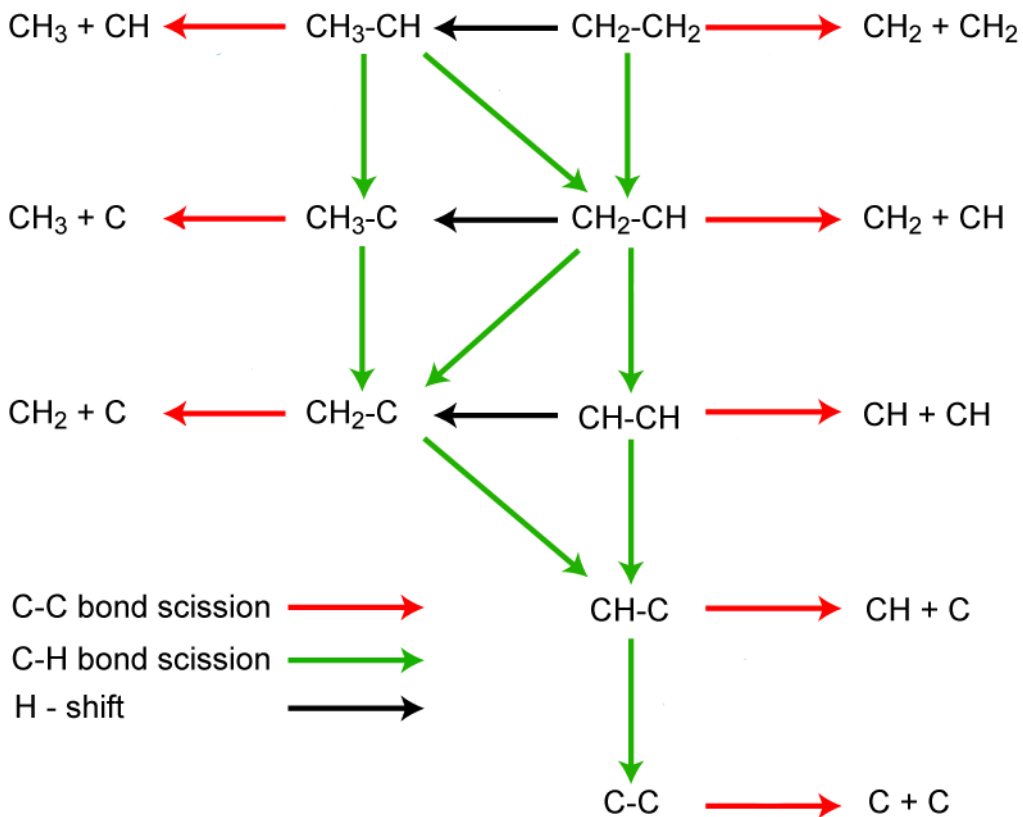


Figure 3.1 Overview of the reaction network of transformations of ethylene including dehydrogenation, C–C bond scission, and 1,2-H shift. Adapted from Ref. 22.

precursors of C_1 species deposited on catalyst surfaces in transformations of unsaturated hydrocarbons are these C_2 species with low H content.

Experimental studies found that on (111) surfaces of Pt, Pd, and Rh, the adsorbed ethylene converts to ethylidyne at room temperature.^{45,48,77-80} On the Ni(111) surface, the conversion product is acetylene and gaseous H_2 .^{50,58,81} Previous theoretical studies dealt with the conversion of ethylene to ethylidyne on Pt(111)^{21,82} and Pd(111)^{18,20,82} surfaces. According to these calculations, the activation barriers of the dehydrogenation/hydrogenation reactions on Pd(111) surfaces are 5–25 kJ mol⁻¹ higher than those on Pt(111). One important point is that the activation barrier of the rate limiting step on Pt(111) is also lower than that of Pd(111), which is in line with the experimentally detected faster conversion on Pt surfaces than on Pd surfaces.⁸³ Andersin et al. investigated computationally the ethylene conversion to ethylidyne⁷¹ as well as the complete decomposition of ethylene to C and H on the surface⁷⁶ on flat Pd(111) and stepped Pd(211) surfaces. Analogous dehydrogenation/hydrogenation reactions show similar barrier heights on both surfaces. Also Li et al. calculated the reactions

for the conversion of ethylene to ethylidyne on Rh(111)¹⁹ to show that the plausible pathway is the same as on Pd(111) surface, but the rate limiting step is different.

Although some of the transition metal systems are known to exhibit rather similar reactivities, there can be differences in specific reaction steps, as in the case of Pt(111) and Pd(111).²¹ Thus, ethylene and other C₂H_x species might behave differently on different transition metal surfaces. Hence a comprehensive study of their adsorption properties and reactivities in dehydrogenation and C–C bond breaking reactions is of interest with a comparison of such metals in mind. Goda et al.⁸⁴ used density functional theory to study the binding of hydrogen, ethylene, acetylene, ethyl, and vinyl on monometallic and bimetallic transition-metal surfaces and determined that the binding energies correlate with the energies of the d-band centers (relative to the Fermi level) of these surfaces. They also reported on the activation barriers of ethyl dehydrogenation to ethylene and vinyl dehydrogenation to acetylene; however these values were obtained from bond order conservation (BOC) theory. Medlin and Allendorf⁸⁵ employed the same surfaces – (111) surfaces of Pt, Pd, Rh, and Ni – to model acetylene and H adsorption, but did not calculate the reactions. Their results show that acetylene adsorbs preferentially above threefold hollow sites on Pt(111), Pd(111), and Rh(111) surfaces, and above two neighboring hollow sites on Ni(111).

In the work reported in this part of the thesis, the aim is to model in a systematic fashion the total decomposition of ethylene by investigating the behavior of C₂H_x ($x = 0 - 4$) species (e.g., ethylene, vinyl, acetylene, ethynyl, and carbon dimer) and to compare the results for (111) surfaces of four metals M, M = Pt, Pd, Rh, and Ni. The present work does not cover the complete reaction network starting from ethylene as presented by Chen et al.²² because the network comprises a large number of reactions. Rather, the present comparison focuses in a systematic way on a chain of dehydrogenation reactions; it comprises of dehydrogenation only from the carbon group with the higher number of H atoms, followed by the C–C bond breaking of the species when there is no C–H bond left. Hence the reactions of interest in this study are: CH₂CH₂ → CH₂CH → CHCH → CHC → CC → C + C. The decomposition step of the carbon dimer is significant as it is the reverse reaction of coke formation, which is an important issue in the loss of the activity of the catalysts.^{86,87} The small C₂ species can also be considered as the precursors of graphene formation.²⁴ As H-shift reactions are not surface-mediated, they have to go over higher barriers^{18,19,21,71,74} than the other types of reactions, hence they are not part of this work.

4. Systematic decomposition of ethylene

4.1. Adsorption Complexes and Energetics of the Intermediates

The adsorption geometries of the six species involved in the reaction route, CH_2CH_2 (ethylene) $\rightarrow \text{CH}_2\text{CH}$ (vinyl) $\rightarrow \text{CHCH}$ (acetylene) $\rightarrow \text{CHC}$ (ethynyl) $\rightarrow \text{CC}$ (carbon dimer) $\rightarrow \text{C} + \text{C}$ on the close-packed (111) surfaces of four transition metals – Pt, Pd, Rh and Ni – along with the relevant energy changes will be described in the following. Figure 4.1 shows representative optimized adsorption modes calculated in this reaction study for each adsorbate.

4.1.1. Ethylene, CH_2CH_2

As mentioned earlier, ethylene adsorption on Group VII metal surfaces occurs in two modes with two different hybridizations of the C atom: in the π mode the carbon is sp^2 hybridized whereas the di- σ mode, depicted in Figure 4.1 as $\eta^1\eta^1$ ethylene, is sp^3 hybridized. As the latter mode^{18,19,60,67,69-72,88} is more stable and active in dehydrogenation reactions it is chosen as the default ethylene adsorption mode on all surfaces. In this mode, the molecule is connected to the surface with two C–M bonds, keeping the C–C axis parallel to the surface at a bridge site. The only exception to this mode among the metals and coverages inspected in this work is the adsorption complex on the Ni(111) surface at the highest coverage (1/3). On this surface, the molecule is adsorbed with one of the carbon atoms having one C–M bond and the other one bonded to three metal atoms of the surface, depicted as $\eta^1\eta^3$ in Figure 4.1. When ethylene molecules are calculated in such an adsorption geometry over the Ni surface at 1/3 coverage, the closest distance between two adjacent molecules – the distance between one of the H atoms of the CH_2 group with the other H of its mirror image – is determined at 199 pm, which is very similar to the corresponding value for the same coverage on other metals (Pt, Pd, Rh) adsorbed at a bridge position in an $\eta^1\eta^1$ mode (190–199 pm). However, when the molecule is forced to adsorb at the bridge position at 1/3 coverage on Ni(111) surface, the closest distance drops to 155 pm, which causes very high repulsive forces. Zhu and White⁵⁰ have observed that at high coverages such a weakly bound mode, different from di- σ exists where the molecule is tilted with one pair of hydrogen atoms closer to the surface, as in the $\eta^1\eta^3$ mode in Figure 4.1. As listed in Table 4.1, the high coverage binding energy is 30 kJ mol⁻¹ less than that of the low coverage one, in line with that observation. Based on the investigations with high resolution X-ray photoelectron spectroscopy (XPS), Lorenz et al.⁸⁹ also proposed an adsorption complex with one C atom at the threefold site while the other is

positioned atop a Ni atom in the $\eta^1\eta^3$ mode, although they have conducted their experiments for a 2×2 structure.

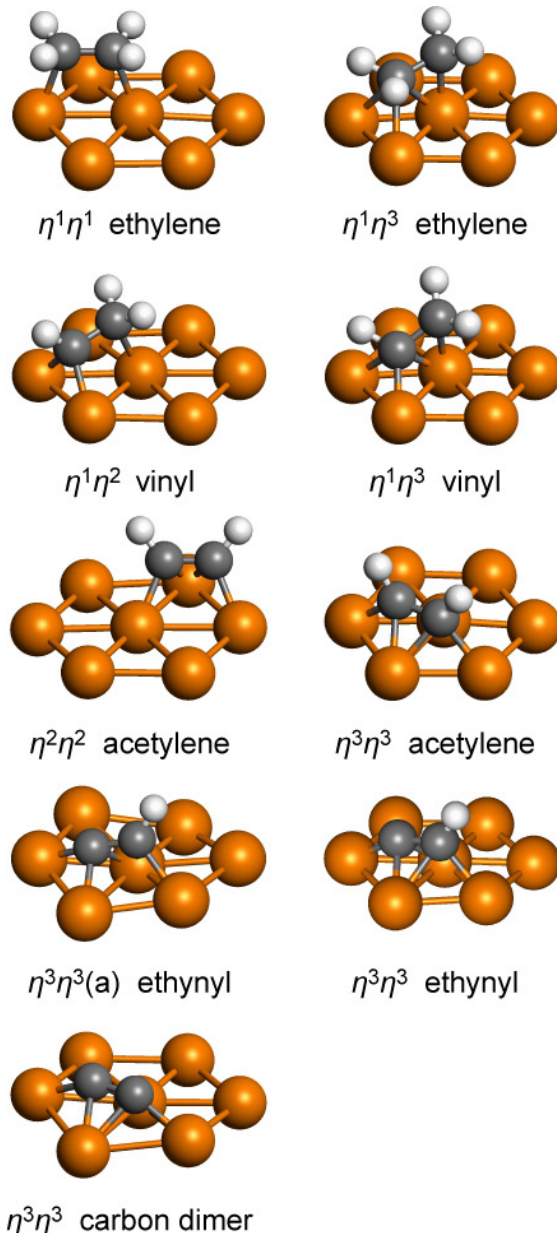


Figure 4.1 Various modes of optimized structures for C_2H_x ($x = 0 - 4$) species on M(111) (M = Pt, Pd, Rh, Ni) surfaces.

The C–C distance is calculated longest for that adsorbed on Pt(111) surface, 149 pm at each coverage as listed in Table 4.1, elongated by 16 pm from the calculated gas phase value. Experimentally, Stöhr et al.⁹⁰ have determined this bond as 149 ± 3 pm from near-edge X-ray absorption fine structure (NEXAFS) spectra, and also in previous calculations very similar values, 148–149 pm, were obtained.^{21,53,54,84,91,92} The C–C bonds get a bit shorter for the molecule adsorbed on Rh and Pd, 146 pm and 145 pm, respectively, (Figure 4.1), as also

Table 4.1 Optimized structure^a (pm) and energy (kJ mol⁻¹) characteristics of ethylene on M(111) (M= Pt, Pd, Rh, and Ni) at various coverages θ .

| metal | θ | C-C | C-H | C-M ^b | BE ^c |
|-------|----------|-----|-----|--------------------|-----------------|
| Pt | 1/3 | 149 | 110 | 211;211 | 94 |
| | 1/4 | 149 | 110 | 211;211 | 103 |
| | 1/9 | 149 | 110 | 212;212 | 109 |
| Pd | 1/3 | 144 | 110 | 212;213 | 74 |
| | 1/4 | 145 | 110 | 212;212 | 80 |
| | 1/9 | 145 | 110 | 212;212 | 94 |
| Rh | 1/3 | 146 | 110 | 213;214 | 70 |
| | 1/4 | 147 | 110 | 213;213 | 83 |
| | 1/9 | 147 | 110 | 214;214 | 86 |
| Ni | 1/3 | 143 | 110 | 216, 220, 226; 197 | 33 |
| | 1/4 | 146 | 110 | 199;200 | 58 |
| | 1/9 | 145 | 110 | 201;201 | 63 |

^a A–B, distance between atoms A and B. ^b The C atom that binds to more surface atoms is listed first. ^c Binding energy (BE) of ethylene (see text).

calculated earlier.^{19,54,67,70,84} A low-energy electron diffraction (LEED) study⁶⁸ reported the latter value as 142±9 pm when ethylene is adsorbed at 80 K on Pd(111). For the $\eta^1\eta^3$ adsorbed C₂H₄ at 1/3 coverage on Ni(111) surface, the C–C bond is 143 pm, 2–3 pm shorter than its $\eta^1\eta^1$ counterpart on lower coverages.

On the (111) surfaces of Pt, Pd, and Rh, the C–M distances are very close, in the range of 211–214 pm (Table 4.1). The values for Pt again agree with previously determined values.^{53,91,92} Goda et al.⁸⁴ calculated the same structures on Pt(111) and Pd(111) surfaces for 1/4 coverage and determined longer C–M distances, Pt: 215 pm and Pd: 218 pm. The values on Pd(111) surface match very well the values reported by Ge and Neurock.⁹³ The C–Rh distances are 213–214 pm, consistent with previously calculated result of 213 pm for 1/4 coverage.¹⁹ For Ni(111) surface, except for the differently adsorbed mode, the C–M distances were 10–15 pm shorter than on the other three transition metals. This difference is in line with the difference of M–M distances of these four surfaces. While the M–M distances of Pt, Pd, and Rh are close to each other, 272–282 pm (Chapter 1), that of Ni is shorter, 248 pm.

For all of these surfaces, binding energies decrease with increasing coverage due to increasing repulsive lateral interactions when the unit cells get smaller. Ethylene is bound

most strongly on the Pt(111) surface, binding energies ranging from 94 kJ mol⁻¹ on the highest coverage to 109 kJ mol⁻¹ on the lowest coverage, followed by the similar strength on Pd, 74–94, and Rh surfaces, 70–86 kJ mol⁻¹. Previous theoretical studies, employing the same exchange-correlation functional, PW91, calculated the binding energy on Pt(111) surface as 100 kJ mol⁻¹ at 1/9 coverage;⁹⁴ as 99,⁸⁴ 101,⁷³ 106,⁵⁴ and 117⁹² kJ mol⁻¹ at 1/4 coverage. For Pd(111) surface the value determined at 1/4 coverage, 80 kJ mol⁻¹, is also very close to the ones calculated by previous theoretical studies, 81–84.^{54,67,84,95} Experimentally, from a combination of microcalorimetric and in situ infrared spectroscopic measurements for the adsorption of ethylene on Pt/SiO₂ and Pt/Sn/SiO₂ catalysts at temperatures from 173 K to 233 K, a heat of adsorption of 125 kJ mol⁻¹ was measured for a mixture of π and di- σ bonded ethylene.⁹⁶

4.1.2. Vinyl, CHCH₂

On Pt, Pd, and Rh(111) surfaces, vinyl is adsorbed such that the sp³ configuration is still intact for both carbon atoms. The C atom of the CH group interacts with the surface through two metal atoms whereas the other carbon atom is bound to one metal center on the surface in a perpendicular bridge form. This $\eta^1\eta^2$ configuration of vinyl is shown in Figure 4.1. Vinyl is adsorbed at an fcc hollow site as the most stable site for the three surfaces. As listed in Table 4.2, the C–M distances for the carbon atom that is bound to two surface atoms are shorter than the C–M distance of the singly bound carbon, by up to 2 pm in the case of Pt and 3–6 pm in the case of Pd and Rh than the C–M distance of the singly bound carbon. Jacob and Goddard⁹⁷ determined C–Pt distances of 205 and 207 pm, 2 pm different from the results of the present study, on a Pt(111) surface modeled with a Pt₃₅ cluster. On Pd(111) the values calculated, 203–205 and 208–209 pm, agree within 2 pm with those of the previous theoretical studies,^{18,70,95} although Sheth et al.⁹⁵ calculated a C–C distance 5–6 pm longer than those of the present and other theoretical studies.^{18,67,70} Li et al.¹⁹ determined very similar C–Rh values, 206–211, as obtained in the present study, 206–212 pm.

Table 4.2 Optimized structure^a (pm) and energy (kJ mol⁻¹) characteristics of vinyl on M(111) (M= Pt, Pd, Rh, and Ni) at various coverages θ .

| metal | θ | C-C | C-H | C-M ^b | BE ^c |
|-------|----------|-----|-----|-------------------|-----------------|
| Pt | 1/3 | 147 | 110 | 208, 208;210 | 289 |
| | 1/4 | 147 | 110 | 207, 207;209 | 304 |
| | 1/9 | 147 | 110 | 207, 207;209 | 309 |
| Pd | 1/3 | 145 | 110 | 204, 205;209 | 255 |
| | 1/4 | 145 | 110 | 204, 204;208 | 263 |
| | 1/9 | 145 | 110 | 203, 203;208 | 281 |
| Rh | 1/3 | 146 | 110 | 206, 207;210 | 279 |
| | 1/4 | 146 | 110 | 206, 207;212 | 286 |
| | 1/9 | 146 | 110 | 206, 206;210 | 293 |
| Ni | 1/3 | 141 | 110 | 188, 198, 205;210 | 247 |
| | 1/4 | 142 | 110 | 189, 200, 202;206 | 271 |
| | 1/9 | 145 | 110 | 189, 200, 201;206 | 280 |

^a A–B, distance between atoms A and B. ^b The C atom that binds to more surface atoms is listed first. ^c Binding energy (BE) of vinyl (see text).

The adsorption complex of vinyl on Ni(111) is totally different from the complexes on the other three metals investigated. Previously, with ethylene, the adsorption mode was calculated to be different only at the highest coverage, see Section 4.1.1, whereas with vinyl the adsorption site is the same one as on the other three metals – fcc hollow site – but the adsorption geometry is different in that the carbon of the CH group is bound to three Ni surface atoms, overall in a $\eta^1\eta^3$ fashion (Figure 4.1). As the Ni–Ni distance is 24–34 pm shorter than the M–M distances of the other metals in consideration, when the CH group gets closer to the surface, the carbon atom starts to interact with an additional surface atom. Interestingly, the hydrogen of the same group also starts interacting with the surface, possibly due to weakened C–H bond. This C–H bond is elongated 5–7 pm from its value in the gas phase; this may be compared to the complexes on the other three metals, where that distance is elongated by 1 pm when adsorbed. The present configuration is in line with the structure calculated by Vang et al.⁵⁵ The distance between the H atom of the CH group and the closest Ni atom ranges between 177 and 181 pm depending on the coverage. Also the C–C bond distance changes with coverage, from 141 pm at the highest coverage to 145 pm at the lowest coverage.

The adsorption of vinyl on the four surfaces is significantly stronger than that of ethylene. The highest binding energies occur on Pt(111) surface, 289–309 kJ mol⁻¹, followed by those on Rh(111) surface, 279–293 kJ mol⁻¹ (Table 4.2). The strength of vinyl adsorption on Pd(111) and Ni(111) surfaces is almost the same at the lowest coverage, at 1/4 coverage the adsorption on Ni is 8 kJ mol⁻¹ stronger, and at 1/3 coverage it is on Pd surface that vinyl adsorbs 8 kJ mol⁻¹ stronger. The value calculated for Pd(111) at 1/4 coverage, 263 kJ mol⁻¹ (Table 4.2) is very close to previously calculated values 274 kJ mol⁻¹ and 267 kJ mol⁻¹.^{18,20,95} For the Rh(111) surface, Li et al.¹⁹ calculated the adsorption energy of vinyl at an fcc hollow site at 1/4 coverage as 278 kJ mol⁻¹, again very close to 286 kJ mol⁻¹ at the same site and coverage determined in the present work.

4.1.3. Acetylene, CHCH

The adsorption mode of acetylene on the (111) surfaces of Pt, Pd, and Rh follows the principle of bond order conservation for the C atoms, such that each C atom forms four σ bonds. The species is adsorbed at an fcc hollow site, interacting with three metal atoms of the surface, one of the surface atoms being shared by both carbon atoms, denoted as M²–C², while the other two interact with individual carbon atoms, M¹–C². In this nomenclature, the upper index denotes the number of metal(carbon) atoms with which each carbon(metal) atom is bound to. This results in the parallel-bridge mode shown in Figure 4.1 as $\eta^2\eta^2$, and has been presented as being the most stable adsorption geometry both experimentally^{62,98-101} and theoretically^{54,85,102,103} on Pt(111) and Pd(111). Dubois et al.⁴⁷ suggested an adsorbed metastable structure of acetylene on Rh(111) surface with its C–C axis parallel to the surface and C-C-H moiety no longer linear. Also for the Rh surface, Medlin and Allendorf⁸⁵ calculated that hcp parallel bridge mode is 36 kJ mol⁻¹ more favorable than the fcc parallel bridge mode, where they calculated the binding energy as 222 kJ mol⁻¹ at 1/4 coverage in comparison to 237 kJ mol⁻¹ in this study, which is only 3 kJ mol⁻¹ less stable than when acetylene is adsorbed at an hcp site. Experimentally, Mate et al.¹⁰⁴ also proposed such a di- σ + π coordinated acetylene on the Rh(111) surface being stable up to 270 K based on high resolution electron energy loss spectroscopy (HREELS) spectra.

Table 4.3 Optimized structure^a (pm) and energy (kJ mol⁻¹) characteristics of acetylene on M(111) (M= Pt, Pd, Rh, and Ni) at various coverages θ .

| metal | θ | C-C | C-H | C-M ^b | BE ^c |
|-------|----------|-----|-----|-----------------------------|-----------------|
| Pt | 1/3 | 139 | 109 | 202, 221;202, 221 | 195 |
| | 1/4 | 139 | 109 | 201, 221;201, 221 | 216 |
| | 1/9 | 139 | 109 | 201, 221;201, 221 | 220 |
| Pd | 1/3 | 136 | 109 | 201, 219;201, 220 | 179 |
| | 1/4 | 136 | 109 | 200, 220;201, 219 | 180 |
| | 1/9 | 137 | 109 | 200,218;200,218 | 202 |
| Rh | 1/3 | 138 | 110 | 203, 216;203, 217 | 224 |
| | 1/4 | 139 | 110 | 203, 217;203, 217 | 237 |
| | 1/9 | 139 | 110 | 202, 217;202, 217 | 240 |
| Ni | 1/3 | 139 | 109 | 197, 201, 201;197, 201, 202 | 203 |
| | 1/4 | 140 | 110 | 195, 200, 201;195, 200, 201 | 239 |
| | 1/9 | 140 | 110 | 195, 201, 201;195, 201,201 | 251 |

^a A–B, distance between atoms A and B. ^b The C atom that binds to more surface atoms is listed first. ^c Binding energy (BE) of acetylene (see text).

The gas phase C–C bond in acetylene is calculated at 121 pm, close to the value determined experimentally.⁹⁰ On Pt(111) surface, this bond elongates to 139 pm at all coverages investigated (Table 4.3). The same degree of elongation is valid on Rh(111) surface, 138–139 pm, and on Pd(111) the C–C bond ranges between 136 and 137 pm. Sesselmann et al.⁹⁸ measured the C–C bond on Pd(111) from a photoelectron diffraction (PhD) study as 134±10 pm. Thus, the calculated results lie within the confidence interval. M²–C² bonds are normally 15–20 pm longer than M¹–C² bonds. Similar values have been obtained by the previous calculations.^{54,84,85,95,100,102}

On the Ni(111) surface, the adsorption mode of acetylene differs. Acetylene prefers to adsorb in $\eta^3\eta^3$ geometry over a long bridge site, where the two carbon atoms occupy nonequivalent hollow sites (Figure 4.1). This mode is in accordance with earlier experimental^{58,81,105} and theoretical^{55,100} results. In this adsorption geometry, six bonds are formed between two carbon atoms and four metal atoms of the surface, two of them via M²–C³, two of them via M¹–C³; the M²–C³ bonds are 4–6 pm longer than the M¹–C³ bonds (Table 4.3). The C–Ni distances agree within 3 pm with values previously calculated by Medlin and

Allendorf.⁸⁵ The optimized C–C bond distance is 139–140 pm, which is ~5 pm shorter than the experimental results, measured at 144±10 pm⁸¹ and 145±3 pm⁹⁰.

In terms of the binding energies, Ni(111) and Rh(111) appear this time as the metals where acetylene binds strongest, 203–251 and 224–240 kJ mol⁻¹, respectively (Table 4.3). Following is the adsorption on Pt(111) surface, in the range of 195–220 kJ mol⁻¹. The experimentally estimated adsorption energy of acetylene on Pt black at 173 K,⁴³ 210 kJ mol⁻¹, falls nicely into this range. The previously calculated BE values of acetylene on Pd(111) surface at 1/4 coverage by Sheth et al.,⁹⁵ 172 kJ mol⁻¹, and Goda et al.,⁸⁴ 181 kJ mol⁻¹, are also very close to the result of the present study, 180 kJ mol⁻¹.

However, comparison of the current results with those obtained in a previous theoretical study, employing the same metals at 1/4 coverage,⁸⁵ shows notable differences. First of all, as mentioned before, in Ref. 85 adsorption on the hcp parallel bridge site was determined to be preferred over that on the fcc parallel bridge site by 36 kJ mol⁻¹ on Rh(111). The binding energy at the most stable site, hcp parallel, was 258 kJ mol⁻¹, whereas it was 222 kJ mol⁻¹ on the fcc parallel adsorption mode.⁸⁵ The value obtained in the current study for the latter adsorption mode is 237 kJ mol⁻¹, 15 kJ mol⁻¹ higher. For the other metals, the most stable adsorption sites are the same but the energies differ. The adsorption energies of the previous study were 13 kJ mol⁻¹, 37 kJ mol⁻¹, and 46 kJ mol⁻¹ higher on Pt, Pd, and Ni, respectively. The differences might be caused by the employment of smaller cut-off energies ranging from 280 to 340 eV depending on the metal, employed in the previous study,⁸⁵ compared to 400 eV used in the present work.

4.1.4. Ethynyl, CHC

Ethynyl adsorbs on the metal surfaces in such a way that the carbon atoms are in two nonequivalent hollow sites, the C atom of the CH group on an hcp site and the other one on an fcc site. However, depending on the metal and the coverage, the bonding of the species differ so that two variants of $\eta^3\eta^3$ mode are obtained, depicted as $\eta^3\eta^3$ and $\eta^3\eta^3(a)$ in Figure 4.1. On the Ni(111) surface at all coverages studied, the regular version of the $\eta^3\eta^3$ mode is most stable. Also on Rh(111) at 1/4 and 1/9 coverages and on Pd(111) at 1/9 coverage that same mode is observed. On Pt(111) at all coverages, on Pd(111) at 1/3 and 1/4 coverages and on Rh(111) at 1/3 coverage, the modified version of the $\eta^3\eta^3$ adsorption mode, $\eta^3\eta^3(a)$, is found. The modification implies an elongation of one of the C–M bonds of the CH group and the CH group moves slightly towards a bridge site, finally stabilizing at an intermediate mode between $\eta^3\eta^3$ and $\eta^3\eta^2$, as seen in Figure 4.1; the bond that elongates is of M²–C³ character.

As a result of this elongation, the longest C–M distance increases to 279 pm on the Pt(111) surface at 1/3 coverage, see Table 4.4. For both variants of this mode, C–M bonds are shorter for the single C atom, hence the C–C bond is not parallel to surface.

Table 4.4 Optimized structure^a (pm) and energy (kJ mol⁻¹) characteristics of ethynyl on M(111) (M= Pt, Pd, Rh, and Ni) at various coverages θ .

| metal | θ | C-C | C-H | C-M ^b | BE ^c |
|-------|----------|-----|-----|-----------------------------|-----------------|
| Pt | 1/3 | 140 | 109 | 203, 200, 216;210, 215, 279 | 457 |
| | 1/4 | 141 | 109 | 198, 201, 214;209, 212, 273 | 433 |
| | 1/9 | 141 | 109 | 198, 202, 212;211, 211, 269 | 454 |
| Pd | 1/3 | 135 | 109 | 205, 198, 211;214, 218, 273 | 450 |
| | 1/4 | 136 | 109 | 198, 201, 209;213, 217, 256 | 435 |
| | 1/9 | 137 | 109 | 197, 201, 201;212, 229, 229 | 474 |
| Rh | 1/3 | 139 | 109 | 200, 198, 206;213, 215, 257 | 512 |
| | 1/4 | 136 | 109 | 192, 213, 213;216, 216, 260 | 519 |
| | 1/9 | 139 | 109 | 196, 205, 205;221, 221, 223 | 522 |
| Ni | 1/3 | 135 | 109 | 180, 189, 190;198, 214, 217 | 493 |
| | 1/4 | 136 | 110 | 181, 191, 192;201, 208, 208 | 513 |
| | 1/9 | 137 | 109 | 181, 191, 191;200, 208, 208 | 527 |

^a A–B, distance between atoms A and B. ^b The C atom that binds to more surface atoms is listed first. ^c Binding energy (BE) of ethynyl (see text).

The binding energies of ethynyl, 433–527 kJ mol⁻¹, on these four metals are higher than those of the rest of the hydrocarbon species addressed in this work. Due to this strong interaction, a perturbation occurs on the first layer of the metal atoms, especially for those at higher coverage, 1/3. One of the metal atoms that the molecule is bound to rises by 80, 66, 47, and 30 pm above the crystal plane in the cases of Pt, Pd, Rh, and Ni, respectively. At other coverages the maximum upward movement of the atom is smaller, e.g., on Pd(111) surface, at 1/4 and 1/9 coverages the maximum shifts are 25 and 22 pm, respectively. Those metals with perturbed upper layers interact stronger with CH₂ species, since the M–M bonds with atoms of the second layer are strongly elongated and these first layer atoms now have lower coordination numbers. On the Pt(111) and Pd(111) surfaces where the perturbation is the most prominent, the BE values at the highest coverage, 1/3, are higher than those at 1/4 coverage. The BE values on Ni(111), 493–527 kJ mol⁻¹, and Rh(111), 512–522 kJ mol⁻¹, are by more

than 50 kJ mol⁻¹ higher than those on Pt(111), 433–457 kJ mol⁻¹ and Pd(111), 435–474 kJ mol⁻¹, Table 4.4.

4.1.5. Carbon dimer, C₂

The adsorption mode of the carbon dimer is the same for all of metals and coverages investigated. As for ethynyl, the carbon atoms are adsorbed above two nonequivalent hollow sites, each connected to the surface via three C-M bonds, shown in Figure 4.1 as $\eta^3\eta^3$ carbon dimer. The formation of these three bonds with the surface is via two M²–C³ and one M¹–C³ interaction, M²–C³ bonds being 10–35 pm longer than M¹–C³ bond, see Figure 4.1 and Table 4.5. The C–C distances are in the range of 131–138 pm, with shorter bonds at higher coverages.

Table 4.5 Optimized structure^a (pm) and energy (kJ mol⁻¹) characteristics of carbon dimer on M(111) (M= Pt, Pd, Rh, and Ni) at various coverages θ .

| metal | θ | C-C | C-M ^b | BE ^c |
|-------|----------|-----|------------------------------|-----------------|
| Pt | 1/3 | 132 | 192, 220, 220; 193, 226, 226 | 609 |
| | 1/4 | 137 | 203, 214, 214; 200, 214, 214 | 587 |
| | 1/9 | 136 | 198, 213, 213; 198, 214, 214 | 619 |
| Pd | 1/3 | 132 | 196, 216, 216; 197, 222, 222 | 599 |
| | 1/4 | 135 | 202, 213, 213; 199, 214, 214 | 592 |
| | 1/9 | 135 | 199, 211, 211; 198, 213, 213 | 635 |
| Rh | 1/3 | 134 | 193, 211, 212; 192, 216, 217 | 691 |
| | 1/4 | 137 | 201, 211, 211; 202, 214, 214 | 689 |
| | 1/9 | 138 | 200, 210, 210; 200, 213, 213 | 698 |
| Ni | 1/3 | 131 | 178, 199, 199; 178, 201, 201 | 664 |
| | 1/4 | 134 | 184, 197, 197; 183, 199, 199 | 691 |
| | 1/9 | 134 | 185, 198, 198; 184, 199, 199 | 708 |

^a A–B, distance between atoms A and B. ^b The C atom that binds to more surface atoms is listed first. ^c Binding energy (BE) of carbon dimer (see text)

Among all species of the type C₂H_x ($x = 0 – 4$) investigated, the binding energies are highest for the carbon dimer on all surfaces, ranging from 587 to 708 kJ mol⁻¹. As a tendency, the binding strength decreases in the order Ni(111) > Rh(111) > Pd(111) > Pt(111). The order is completely reversed from the case of ethylene adsorption. As in the case of ethynyl, the strong interaction with the surface causes the surface to distort so the metal atoms of the

uppermost layer, connected in M¹–C³, fashion move up. This effect is most pronounced at 1/3 coverage as these surface atoms are shared by adjacent adsorbates, hence these surface atoms also have M²–C³ bonds. The upward shifts are 76, 57, 59, and 42 pm on Pt, Pd, Rh, and Ni(111), respectively, so that linear chains composed of -C-C-M-C-C-M- are formed. The C–M bonds formed by these displaced atoms are ~10 pm shorter than the corresponding values at lower coverages. The C–C bond distances of these structures are also 3–5 pm shorter at 1/3 coverages, Table 4.5. The binding energies at the (111) surfaces of Pt, Pd, and Rh, at 1/3 coverage, are higher than those at lower coverages; hence, this strong C–M interaction overcomes the repulsion due to lateral interactions. At lower coverages than 1/3, the upward shifts of the surface atoms are significantly smaller, e.g., on Pd(111) the maximum rise of the atoms is 28 pm for both 1/4 and 1/9 coverages. The energies calculated for C₂ adsorption on Pt(111) at 1/9 coverage, 619 kJ mol⁻¹, and on Pd(111) at 1/4 coverage, 592 kJ mol⁻¹, are in agreement with recent theoretical studies.^{24,106}

4.1.6. Atomic carbon, C

When a carbon atom is adsorbed on an M(111) surface, it prefers high coordinated threefold-hollow sites, fcc or hcp, depending on the metal. On Pt(111), with decreasing coverage, the hcp site becomes more stable, ranging from 4–17 kJ mol⁻¹, Table 4.6. This preference was previously documented by other theoretical studies.^{97,107} On Pd surface both sites are equally stable with a slight preference for the hcp site, especially at the 1/4 coverage; this result also agrees well with previous studies.^{24,108} On Rh(111) surface, the preference of hcp sites over fcc sites is significant, by 20–28 kJ mol⁻¹. Mavrikakis et al.¹⁰⁹ also stated the preference of hcp sites over fcc by 32 kJ mol⁻¹ on Rh at 1/4 coverage. The values calculated for Ni(111) surface are close to that obtained experimentally^{110,111} and suggest that adsorption on hcp hollow site is preferred by ~7 kJ mol⁻¹, which is also calculated by Zhang et al.¹¹² and Xu and Saeys.¹¹³ However, the theoretical study of Klinke et al.¹¹⁴ differs from the former works in that the fcc site is preferred by almost 70 kJ mol⁻¹.

Table 4.6 Optimized structure^a (pm) and energy (kJ mol⁻¹) characteristics of carbon atom on M(111) (M= Pt, Pd, Rh, and Ni) at various coverages θ .

| metal | θ | | C-M | BE ^b | metal | θ | | C-M | BE ^b |
|-------|----------|-----|-----|-----------------|-------|----------|-----|-----|-----------------|
| Pt | 1/3 | fcc | 191 | 672 | Rh | 1/3 | fcc | 191 | 671 |
| | 1/4 | | 192 | 683 | | 1/4 | | 191 | 680 |
| | 1/9 | | 191 | 695 | | 1/9 | | 190 | 690 |
| | 1/3 | hcp | 193 | 668 | | 1/3 | hcp | 190 | 699 |
| | 1/4 | | 193 | 675 | | 1/4 | | 191 | 704 |
| | 1/9 | | 192 | 678 | | 1/9 | | 191 | 709 |
| Pd | 1/3 | fcc | 188 | 662 | Ni | 1/3 | fcc | 176 | 661 |
| | 1/4 | | 189 | 664 | | 1/4 | | 176 | 664 |
| | 1/9 | | 187 | 684 | | 1/9 | | 176 | 668 |
| | 1/3 | hcp | 189 | 663 | | 1/3 | hcp | 176 | 667 |
| | 1/4 | | 190 | 675 | | 1/4 | | 176 | 671 |
| | 1/9 | | 188 | 684 | | 1/9 | | 176 | 674 |

^a A–B, distance between atoms A and B. ^b Binding energy (BE) of the C atom (see text).

4.2. Reaction energetics for decomposition of ethylene C₂H₄ over M(111) (M = Pt, Pd, Rh, Ni)

This section will present a systematic account of the decomposition of C₂H₄, namely in each step a dehydrogenation at the C atom that has the higher number of H substituents and the final C–C bond breaking. Both the energetics of the reactions and the geometric properties of the transition states will be discussed. Although the adsorption of the species was calculated at three different coverages, the reactions (i.e., the transition structures) were only modeled at the lowest coverage, 1/9. The same type of adsorption sites were considered separately for the initial and the final states. This also means that in rare cases, not the most stable species, but species with a similar adsorption geometry, at the same site, were considered. Also the leaving H atom was coadsorbed at the same type of sites at corresponding final states. The diffusion of H atom was not considered as it occurs easily on metal surfaces. The properties of the transition state structures as well as the reaction energies and corresponding activation barriers are summarized in Table 4.7.

4.2.1. Ethylene dehydrogenation, TS1

The first reaction is hydrogen extraction from the di- σ bound ethylene species on the metal surface. As listed in Table 4.1, the C–H bond is 110 pm for the adsorbed species. In the transition state, it elongates to 155–174 pm depending on the metal (Table 4.7). As depicted in Figure 4.2, the dissociating H atom interacts with a neighboring metal atom of the surface

Table 4.7 Optimized structure^a (pm) and energy (kJ mol⁻¹) characteristics of transition states^b during the model ethylene decomposition on M(111), M = Pd, Pt, Rh, and Ni, at 1/9 coverage.

| | | E_r | E_r^{inf} | E_a^b | C-C | C-H ^c | C-M ^d | M-H ^c |
|------------------|----|-------|-------------|---------|-----|------------------|------------------------------|------------------|
| TS1 ^e | Pt | 25 | 13 | 81 | 148 | 155 | 209, 220; 209 | 162 |
| | Pd | 25 | 9 | 99 | 145 | 174 | 207, 210; 208 | 159 |
| | Rh | -1 | 1 | 45 | 147 | 164 | 210, 211; 210 | 161 |
| | Ni | -7 | -15 | 47 | 142 | 173 | 190, 202, 207; 203 | 149 |
| TS2 ^e | Pt | 14 | 3 | 85 | 140 | 148 | 200, 221; 212, 221 | 162 |
| | Pd | -11 | -24 | 76 | 138 | 160 | 201, 215; 205, 231 | 163 |
| | Rh | -37 | -38 | 21 | 140 | 152 | 201, 216; 208, 218 | 162 |
| | Ni | -58 | -68 | 50 | 143 | 143 | 193, 218, 220; 190, 192, 245 | 153 |
| TS3 ^e | Pt | 83 | 79 | 143 | 141 | 159 | 197, 211, 214; 210, 211, 275 | 166 |
| | Pd | 31 | 25 | 119 | 137 | 176 | 197, 201, 207; 210, 217, 258 | 159 |
| | Rh | 27 | 28 | 96 | 139 | 162 | 196, 202, 203; 222, 224, 225 | 165 |
| | Ni | 29 | 26 | 111 | 136 | 177 | 179, 189, 189; 200, 211, 211 | 149 |
| TS4 ^e | Pt | 85 | 73 | 143 | 136 | 159 | 198, 215, 215; 201, 214, 214 | 165 |
| | Pd | 72 | 61 | 154 | 134 | 181 | 200, 214, 214; 197, 212, 212 | 158 |
| | Rh | 60 | 58 | 131 | 137 | 164 | 197, 210, 210; 202, 212, 212 | 164 |
| | Ni | 57 | 46 | 131 | 134 | 176 | 181, 195, 196; 186, 199, 200 | 149 |
| TS5 ^f | Pt | -46 | -101 | 135 | 188 | | 192, 197, 237; 193, 204, 205 | |
| | Pd | 1 | -63 | 121 | 194 | | 190, 199, 204; 190, 199, 204 | |
| | Rh | -16 | -50 | 113 | 224 | | 185, 192, 205; 182, 194, 237 | |
| | Ni | 71 | 29 | 142 | 199 | | 177, 183, 185; 177, 183, 185 | |

^a A–B, distance between atoms A and B in the transition state. ^b Activation energy. ^c Distance characterizing a bond that forms or breaks during the reaction. ^d The C atom that binds to more surface atoms is listed first. ^e Transition state of a dehydrogenation reaction. ^f Transition state of C–C scission.

and at the transition state, it is bound at an atop position with an H–M distance of 149–162 pm. The carbon from which the H atom dissociated gets closer to the surface, forming new C–M bonds, one in the cases of Pt, Pd, and Rh, and two in the case of Ni. In the final state the hydrocarbon species assume their corresponding vinyl structures with H atom adsorbed at a nearby threefold site, as shown in the second column of Figure 4.2. As the structure at the transition state resembles that of the final state, one can say that this transition complex has a “late” character.

The abstraction of the first hydrogen is energetically comparable on Pt(111) and Pd(111), endothermic by 25 kJ mol⁻¹. On Rh(111), it is thermoneutral and on Ni(111) slightly exothermic, see Table 4.7. The activation barriers on the latter two surfaces are very similar, 45 and 47 kJ mol⁻¹, respectively. Compared to values for Pt(111) and Pd(111), these barriers are significantly smaller, as on Pt(111) the barrier is 81 kJ mol⁻¹ and on Pd(111) it is almost 100 kJ mol⁻¹. This points to easier dehydrogenation of ethylene in the case of Rh(111) and Ni(111) under similar conditions.

Several computational studies previously dealt with ethylene dehydrogenation on the transition metals studied here.^{18–22,55,70,71,74,76} The results of Pt(111) and Pd(111) surfaces from these studies, where five layers were employed instead of four layers as in the present work, are in complete accordance with our model;^{18,20–22} differences amount to at most 6 kJ mol⁻¹ on Pt(111) and 1 kJ mol⁻¹ on Pd(111). Pallassana et al.⁷⁰ carried out calculations for the dehydrogenation of ethylene on Pd(111) at 1/3 coverage and calculated the reaction energy as 73 kJ mol⁻¹ and the barrier as 151 kJ mol⁻¹. Although the geometry optimized for the transition state is very close to the one presented here, the energies are far too different. Moskaleva et al.¹⁸ discussed the discrepancy in detail, presenting the importance of coverage for reaction energies. Also the criteria applied to reach convergence in Pallassana et al.’s work⁷⁰ are not very tight: the forces in all directions are converged to 2×10^{-2} eV/pm compared to 2×10^{-4} eV/pm employed in the present work (see computational details). The results of the current study for Pt(111) agree with those calculated by Chen and Vlachos⁷⁴ who found the reaction energy as 2 kJ mol⁻¹ with the products at infinite distance, which is 13 kJ mol⁻¹ in the present calculations, and the barrier as 81 kJ mol⁻¹. For Rh(111) surface Li et al.¹⁹ used a three-layer model at 1/4 coverage to show the reaction is also thermoneutral, 2 kJ mol⁻¹, over a similar barrier, 50 kJ mol⁻¹. Here, the difference in the coverage might be the cause of the slight difference in energies, keeping in mind that for Rh(111), coverage effect is much less prominent than on Pd(111), see Tables 4.2, 4.3, 4.4, 4.5, and 4.6. The results obtained by Vang et al.⁵⁵ for Ni(111) surface are, however, different from the ones reported

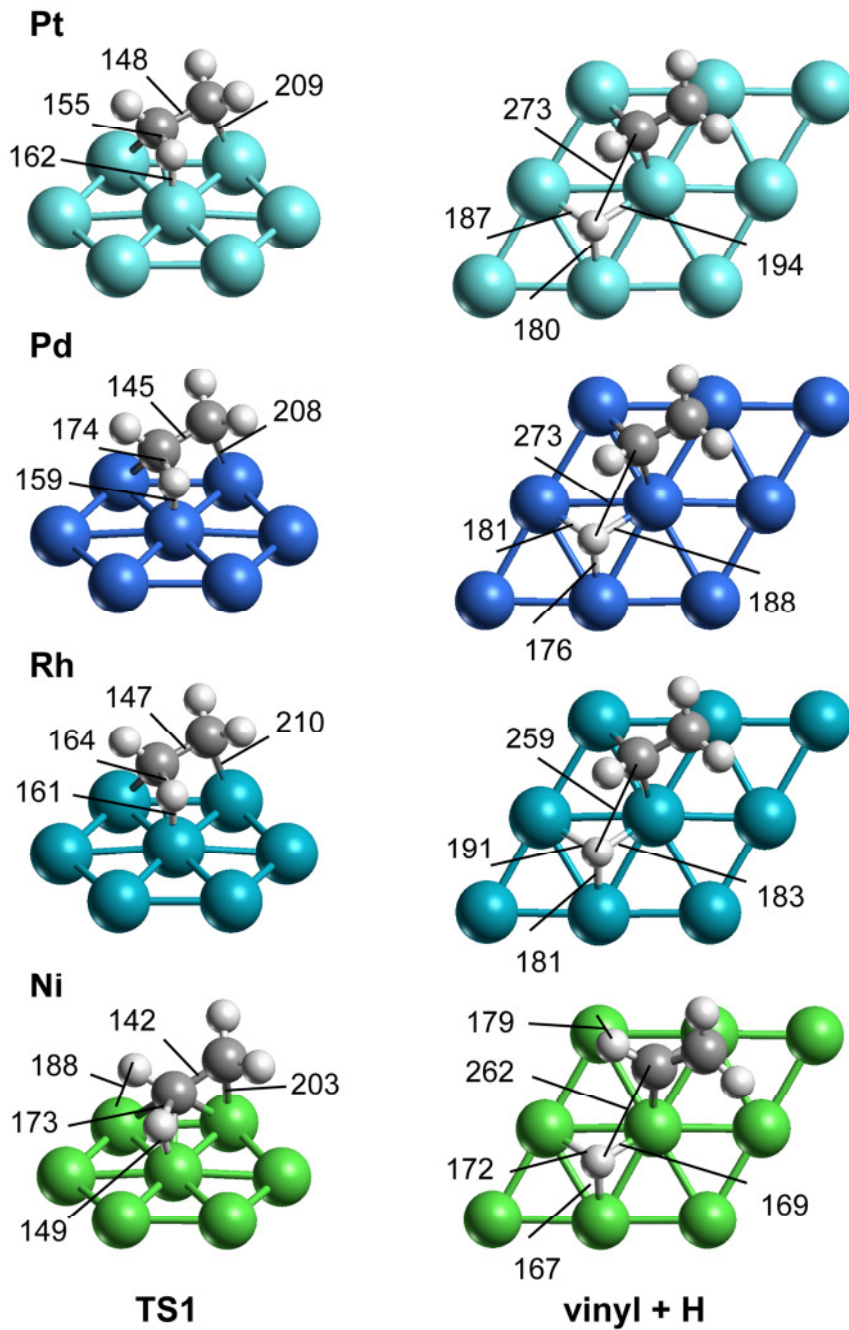


Figure 4.2 Structures of transition and final states at 1/9 coverage of ethylene dehydrogenation to vinyl step on four (111) transition metal surfaces: Pt, Pd, Rh and Ni.

here. They reported that, at 1/6 coverage, the reaction is endothermic by 20 kJ mol⁻¹ over a barrier of 60 kJ mol⁻¹. The main reason for the deviating results is the different initial state of the reaction. Vang et al.⁵⁵ calculated top adsorption, in the form of π adsorbed C₂H₄, on Ni(111) surface as the most stable mode, with a binding energy of 15 kJ mol⁻¹, which is 43–48 kJ mol⁻¹ lower than the binding energy calculated in the present work for the bridge di- σ mode. Assuming that the energy of the product, adsorbed similarly as in the present work, is

similar to the value obtained also in this work, a lower energy of the initial state structure would result in an endothermic reaction, as reported by Vang et al.⁵⁵ The change in the activation barrier is harder to anticipate as the transition state structure of the dehydrogenation of π adsorbed C₂H₄, as calculated by Vang et al.,⁵⁵ might be different than that of the dehydrogenation of bridge di- σ mode adsorbed C₂H₄.

4.2.2. Vinyl dehydrogenation, TS2

In this systematic study, dehydrogenation from the H rich group is investigated, so here the focus is on the dehydrogenation from the CH₂ group of vinyl to acetylene. As in the case of ethylene, the C–H bond of the CH₂ moiety is also 110 pm. This C–H bond elongates to 143–160 pm in the TS structure, similar to the case of ethylene (see Table 4.7 and Figure 4.3). In general the C–H bond is shorter in TS2 than in TS1, 7–14 pm in the case of Pt, Pd, and Rh, however, in the case of Ni, for TS1 the elongation is 63 pm whereas for TS2 it is only 33 pm. The dissociating H atom approaches a surface atom that is already bound to the C atom of the CH₂ group, as can be seen in Figure 4.3. In the TS structure, the H–M bond has shrunk to 153–163 pm. Simultaneously, on Pt(111), Pd(111), and Rh(111), the C atom of the CH₂ group also moves, forming a second bond with the surface. In this way it occupies on these surfaces the most stable site of acetylene adsorption, a hollow fcc site in a $\eta^2\eta^2$ fashion. Indeed, this transition state geometry is very close to the one discussed earlier for the hydrogenation of acetylene on Pd(111) surface.¹⁰³ On Ni(111), the C atom moves again in such a way that it forms two additional bonds with the surface, to reach the adsorption mode of acetylene in $\eta^3\eta^3$ fashion on the Ni surface as depicted in Figure 4.3.

Concerning the thermodynamics, the dehydrogenation of vinyl to acetylene is a more favorable process compared to the previous dehydrogenation step. Except on Pt(111), where the reaction is still endothermic by 14 kJ mol⁻¹, the reaction is exothermic by -11, -37, and -58 kJ mol⁻¹ on Pd(111), Rh(111) and Ni(111), respectively (Table 4.7). The change in the activation barriers, however, does not have a clear trend. In the case of Pt(111), the barrier is almost the same as that of the previous dehydrogenation step whereas for Pd(111) it has decreased by 23 kJ mol⁻¹. Although the geometry of the TS structure is very close to the one calculated by Sheth et al.¹⁰³ on Pd(111), the energetics do not match at all, probably due to the lower plane-wave cutoff energies and less number of layers employed in their study. Calculations by Chen and Vlachos⁷⁴ on Pt(111) resulted in a transition state passing over a barrier of 99 kJ mol⁻¹, which is 14 kJ mol⁻¹ higher than the one presented here. However, they had used a 2 × 2 unit cell. They also reported that calculations for a 3 × 3 unit cell showed

$\sim 10 \text{ kJ mol}^{-1}$ lower reaction barrier,⁷⁴ bringing the activation barrier closer to that determined in this study. The large decrease in the barrier height is also valid in the case of vinyl dehydrogenation on the Rh(111) where the barrier drops down to 21 kJ mol^{-1} . This is the smallest barrier among the four dehydrogenation reactions and the one C-C bond scission on the four metals covered in this work.

On the Ni(111) surface, as on Pt(111) surface, the barrier is almost the same as that of

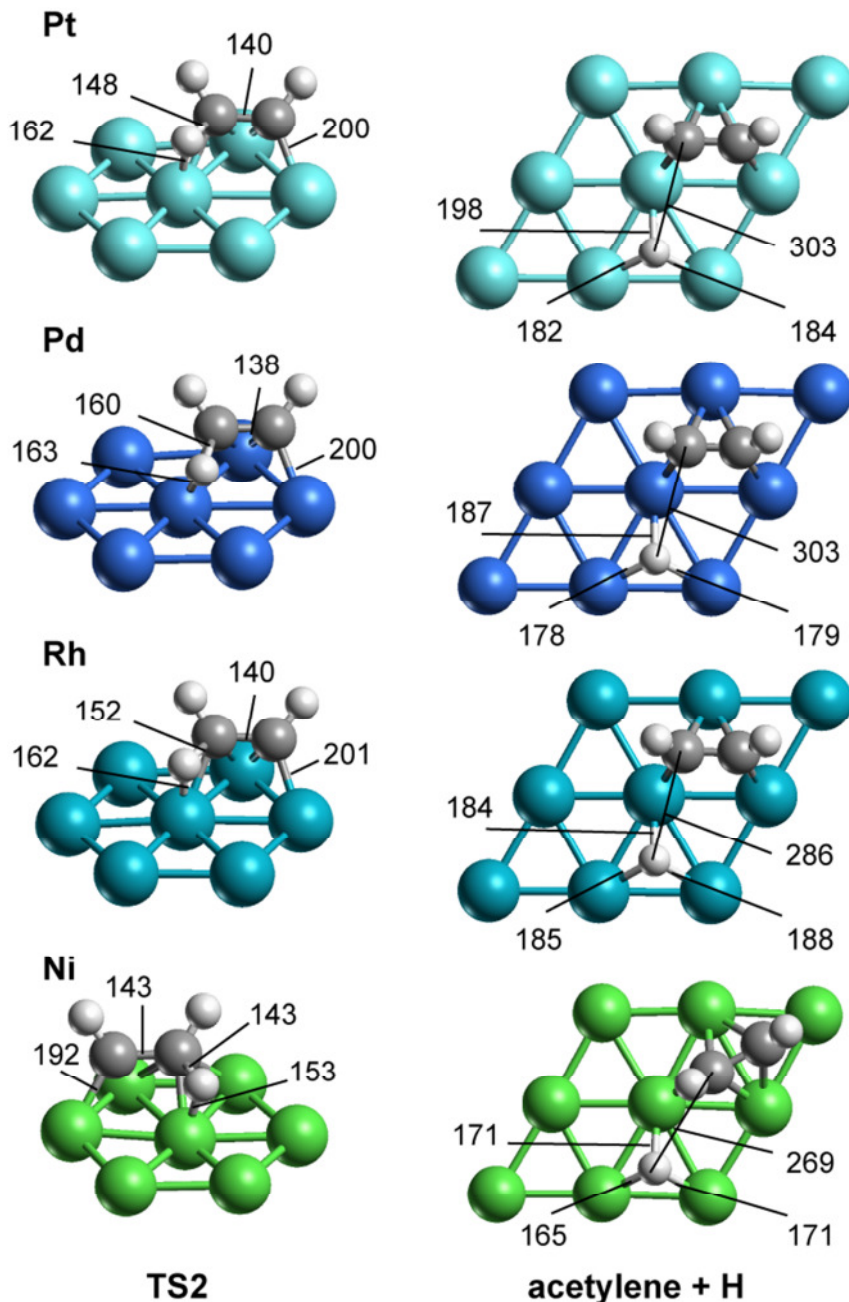


Figure 4.3 Structures of transition and final states at 1/9 coverage of vinyl dehydrogenation to acetylene step on four (111) transition metal surfaces: Pt, Pd, Rh and Ni.

ethylene dehydrogenation. The value calculated by Vang et al.⁵⁵ for this reaction on Ni(111) is not as far off as it was in the case of ethylene dehydrogenation, as the initial state and the final state in this case are similar to those of the present work.

4.2.3. Acetylene dehydrogenation, TS3

The optimized TS structures for acetylene dehydrogenation are shown in Figure 4.4. The geometry and adsorption modes were found to be similar on the (111) surfaces of the four metals investigated. The H atom forms a bond with a surface atom; the C atom, from which this H atom is subtracted, starts to interact with the same surface atom. At the transition state, the H–M bond is ~149–166 pm with H atop the metal atom and the incipient C–M bond is 179–197 pm, see Table 4.7. At the TS, the CH moiety is also bound to three metal atoms of the surface as in the case of ethynyl rather than in the case of acetylene.

The conversion of acetylene adsorbed on a (111) surface of a late transition metal has been examined in various experimental studies.^{50,104,115,116} Vinylidene, ethynyl, methylidyne, ethylidyne, and surface carbon have been observed at low temperatures. On Pd(111) and Rh(111) dehydrogenation to ethynyl was observed, whereas on Pt(111) acetylene converts preferentially to vinylidene. On Ni(111) it undergoes C–C bond cleavage. When the reaction energies and activation barriers of dehydrogenation to ethynyl are calculated, this difference of behavior is easily explained by the high barrier and endothermicity of this reaction on the Pt(111) surface. The reaction energies of dehydrogenation are 27–31 kJ mol⁻¹ and the barriers 96–119 kJ mol⁻¹ for Pd, Rh, and Ni surfaces, in contrast to the reaction energy of 83 kJ mol⁻¹ and the corresponding barrier of 143 kJ mol⁻¹ on the Pt surface. Another experimental study¹¹⁷ proposed vinylidene as product of acetylene conversion on Pd(111) surface; however calculations²² showed that this conversion occurs via the formation of ethynyl, which afterwards is hydrogenated to vinylidene.

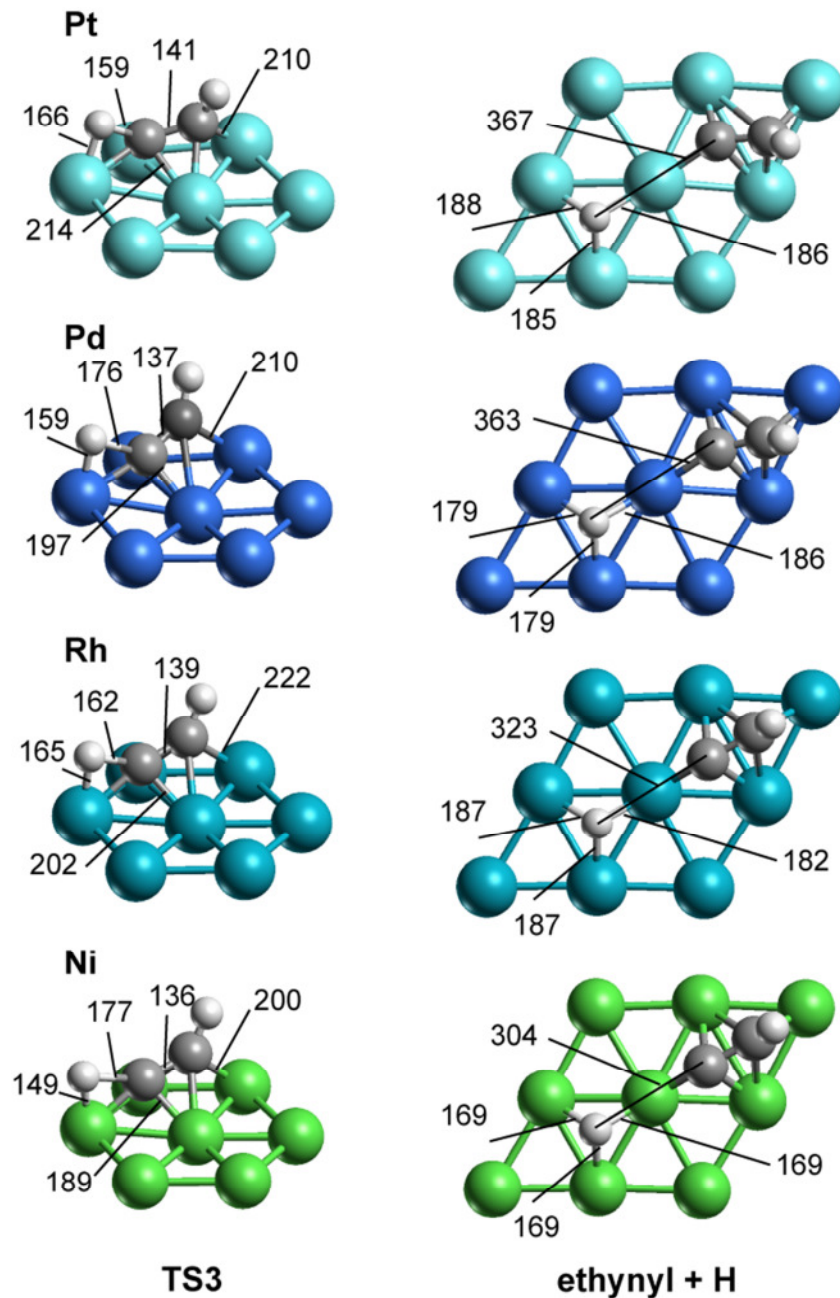


Figure 4.4 Structures of transition and final states at 1/9 coverage of acetylene dehydrogenation to ethynyl step four (111) transition metal surfaces: Pt, Pd, Rh and Ni.

4.2.4. Ethynyl dehydrogenation, TS4

In this step the only remaining H atom is removed from the adsorbate. The H atom interacts with the surface metal atom to which the C atom is bound in M¹-C³ mode (Figure 4.5). In the transition state the H-M bond is 149–165 pm, see Table 4.7. The C-H distances in the TS vary between 159 and 181 pm depending on the metal; the values are very close to those of the previous dehydrogenation steps on the respective metals, except for the transition state structures of vinyl dehydrogenation. At the transition state, the adsorbate has reached

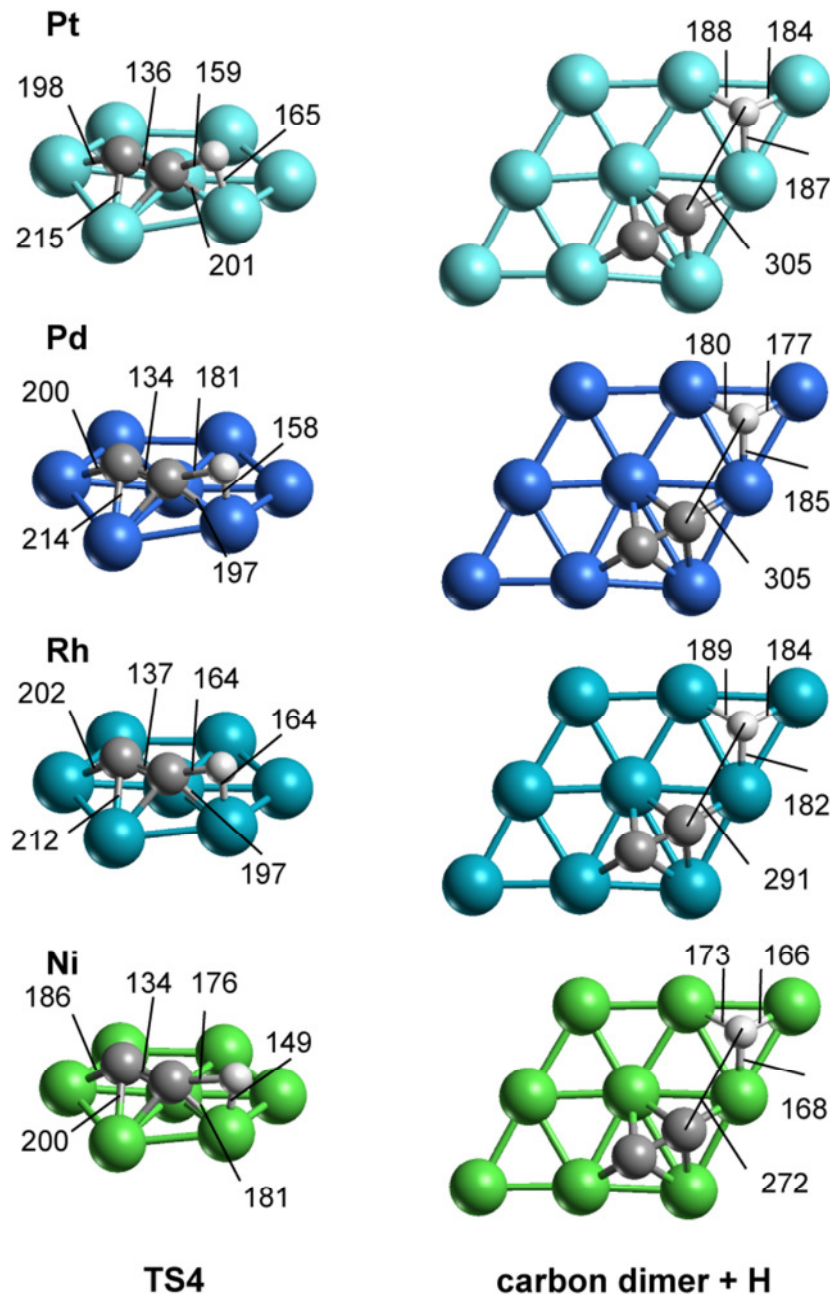


Figure 4.5 Structures of transition and final states at 1/9 coverage of ethynyl dehydrogenation to carbon dimer step on four (111) transition metal surfaces: Pt, Pd, Rh and Ni.

almost the final state structure of the carbon dimer, as the C atom of the original CH moiety gets closer to the surface.

The energy required to remove the last hydrogen from the hydrocarbon is the highest among all calculated dehydrogenation reactions on the four transition metals of interest. The dehydrogenation of ethynyl is exclusively endothermic, by 57–85 kJ mol⁻¹, over a high barrier, 131–154 kJ mol⁻¹ (Table 4.7). The reaction energy on Pt(111) surface, 85 kJ mol⁻¹, is

again the highest among all with a value close to that of acetylene dehydrogenation. However, differently from the case of acetylene dehydrogenation, the other values are rather close, at 72, 60, and 57 kJ mol⁻¹ on Pd(111), Rh(111), and Ni(111), respectively. For the latter three metals, the values are ~28 kJ mol⁻¹ higher than those of acetylene dehydrogenation. As for the activation barriers, the one calculated on Pd(111) takes the lead, 154 kJ mol⁻¹, which is also the highest activation barrier in this series of reactions, including the C–C bond scission that is yet to be covered. The value on Pt(111) is only 11 kJ mol⁻¹ lower, followed by 131 kJ mol⁻¹ on both Rh(111) and Ni(111) surfaces.

4.2.5. Carbon dimer dissociation, TS5

After removing all hydrogen atoms from ethylene in a systematic fashion, a carbon dimer is left on the surface, as already explained in Chapter 4. In this step, the C–C bond is broken while one of the atoms migrates to a neighboring fcc-threefold site. The TS structures are similar on Pt(111), Pd(111), and Ni(111) surfaces; both carbon atoms are located at bridge positions. In general, an adsorbate at a bridge position is bound to two surface atoms; however, as the surface is distorted through strong C–M interaction, each of the C atoms binds to three surface atoms in these TS structures. On these surfaces, the C–C distance elongates from 134–136 pm in the initial state (Table 4.5) to 188–199 pm in the transition state (Table 4.7). On Rh(111) only one of the C atoms moves significantly to a bridge site while the other one remains almost at its initial position. In this latter case, the C–C bond is longer than on the other three metals, 224 pm in the transition state. Subsequently, the C atom at the bridge position moves toward an fcc position. This difference of transition state geometry might be due to the difference of site choice of C atom on the Rh surface; see Table 4.6. The hcp site is preferred by almost 20 kJ mol⁻¹ on Rh(111) and by only 6 kJ mol⁻¹ on Ni(111) whereas on Pt(111) the fcc site is preferred by 17 kJ mol⁻¹ and hcp and fcc sites are isoenergetic on Pd(111).

On Pt(111), the surface with the highest endothermicity for the dehydrogenation reactions occurs, C–C bond scission is a favorable process, releasing 46 kJ mol⁻¹. C–C bond breaking is also exothermic on Rh(111), -16 kJ mol⁻¹, energetically neutral on Pd(111), 1 kJ mol⁻¹, and highly endothermic on Ni(111), 71 kJ mol⁻¹. In fact, this transformation is the most endothermic reaction on Ni(111) surface encountered in this study. Although the reactions on Pt, Pd, and Rh(111) surfaces are mostly exothermic, the barriers are still high, comparable with vinyl dehydrogenation. The barrier of the C–C bond scission on Ni(111), 142 kJ mol⁻¹, is the highest among the reactions studied here for this surface. In a previous

theoretical work⁷⁶ the reaction energy of C–C bond scission on Pd(111) was calculated at 28 kJ mol⁻¹ for 1/6 coverage and at 138 kJ mol⁻¹ for the corresponding activation barrier.

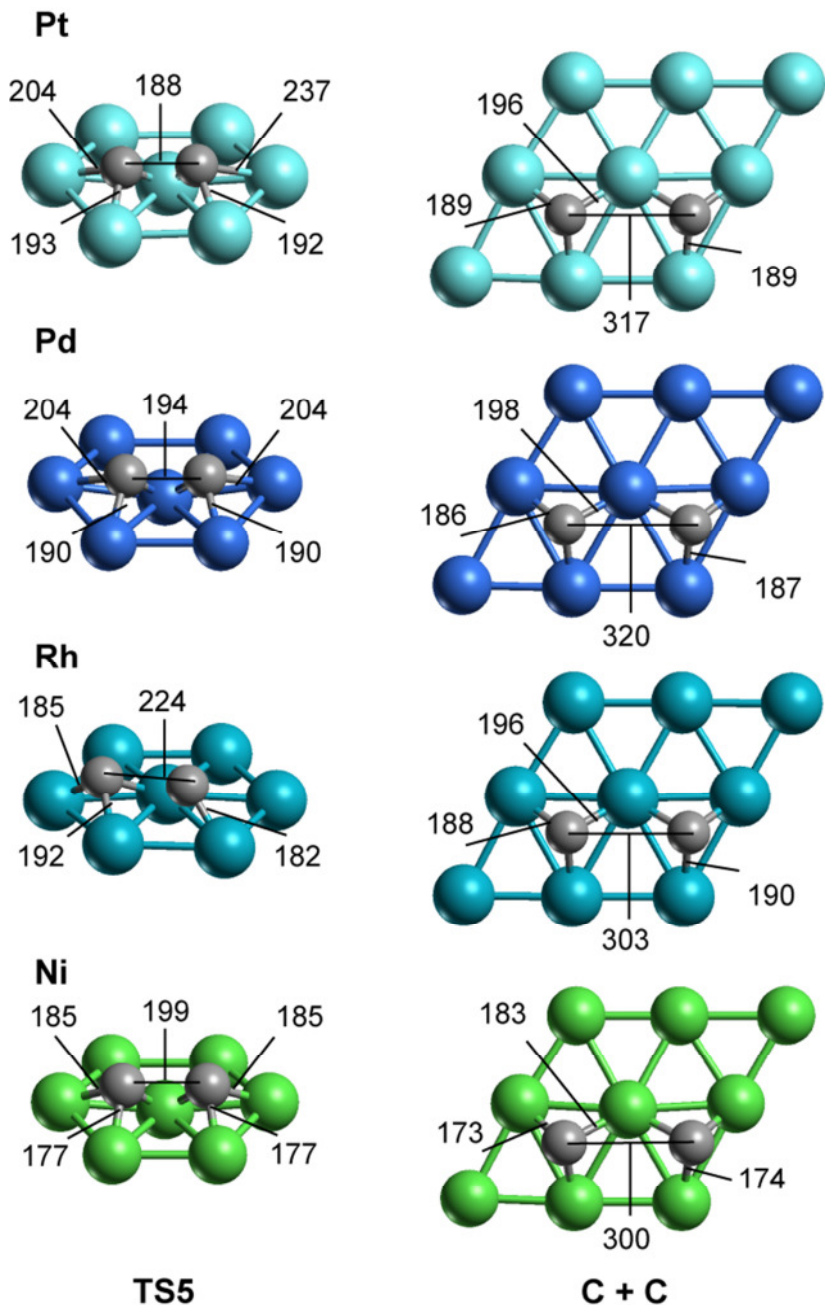


Figure 4.6 Structures of transition and final states at 1/9 coverage of C–C bond scission of the carbon dimer step on four (111) transition metal surfaces: Pt, Pd, Rh and Ni.

5. Discussion

Next, binding energies and reaction energetics as well as activation barriers will be analyzed and compared among the four metals. Also the effect of the coverage and the well-known Brønsted–Evans–Polanyi (BEP) relationship^{102,103} will be discussed.

5.1. Binding energies

The binding energies of the species C_2H_x ($x = 0 - 4$) calculated on the surfaces M(111) of four late transition metals (M = Pt, Pd, Rh, and Ni) at 1/9 coverage are shown in Figure 5.1. For ethylene, the strength of adsorption decreases in the order Pt > Pd > Rh > Ni. The ordering of ethylene adsorption strength is valid also for 1/4 and 1/9 coverages, except that Pd and Rh switch place at 1/4 coverage, see Table 4.1. For vinyl, the adsorption is strongest again on Pt and weakest on Ni, however, different from ethylene adsorption, adsorption of vinyl on Rh(111) is stronger than on Pd(111). When the hydrogen content decreases further, to at most one hydrogen per C atom, the adsorption strength trend is reversed; adsorption on Ni(111) becomes the strongest, closely followed by the adsorption strength on Rh(111) while for Pd(111) and Pt(111) the adsorption energies are lower and similar to each other.

The binding energies of the hydrocarbon species on each metal are ordered in the same way: $C_2H_4 < C_2H_2 < C_2H_3 < C_2H < C_2 < C$. The reason that C_2H_2 adsorbs weaker than C_2H_3 is the high stability of the former species also in the gas phase. This will be shown by the subsequent energy analysis. Another way of rationalizing this trend is by reference to the radical character of vinyl. Otherwise, the trend of the BE values of hydrocarbons is consistent with the bond order conservation concept; the fewer H atoms are bound to carbon centers, the stronger is the interaction with the surface.

To gain more insight into these binding energies, they were separated into partial contributions, namely the deformation energies of the surface and the hydrocarbon species. In this way the binding energy, BE, is the result of the interaction between suitably prepared surface and hydrocarbon species moieties, weakened by the deformations of these two subsystems; $BE = E_{int} - \Delta E(M) - \Delta E(C_2H_x)$. Here E_{int} is the (full) metal-adsorbate interaction, $\Delta E(M)$ and $\Delta E(C_2H_x)$ are the deformation energies of the metal surface and the adsorbate, respectively. The latter two values are obtained by calculating the amount of energy required to bring a system, either the clean metal surface or the molecular species in the gas phase, from its equilibrium structure to the structure displayed in the adsorption complex. The resulting E_{int} values, along with the deformation energies at 1/9 coverage are listed in Table 5.1. The resemblance between the trends of the resulting E_{int} and BE values is quite

noticeable; see Figures 5.1a and b. Inspection of the binding energy, the interaction energy, and the deformation energies reveals that the irregular behavior of C_2H_2 is due to the larger deformation energy that accompanies the adsorption (Figure 5.1c).

The deformation energy by itself also requires a further decomposition and analysis of its components. As can be seen from Figures 5.1d and e, the major part of the deformation is due to the change of the structure of the adsorbate, $220\text{--}280\text{ kJ mol}^{-1}$, not to that of the surface, $8\text{--}22\text{ kJ mol}^{-1}$ (see Table 5.1). The deformation of the adsorbate is highest in the case of acetylene. In fact, apart from C_2H and C_2 where the surface buckles during adsorption, the adsorbate deformation is all the time the major contribution to the total deformation energy. The energies for the deformation of the hydrocarbon species increase from ethylene, $87\text{--}132\text{ kJ mol}^{-1}$, to vinyl, $74\text{--}192\text{ kJ mol}^{-1}$, and peaks at acetylene. For the same species, the deformation of the surface is not very significant, the energies ranging from 7 to 22 kJ mol^{-1} . For the hydrocarbon species with lower H content, C_2H and C_2 , the deformation of the adsorbate decreases to 50 kJ mol^{-1} (Table 5.1, Figure 5.1d), whereas for the same species the deformation energy of the surface increases up to 83 kJ mol^{-1} (Table 5.1, Figure 5.1e). The deformation energy for Pt(111) is significantly higher for these species, along with that of Pd(111) to some extent, followed by Rh(111). This trend is in accordance with the M–M distances, Pt–Pt distance being the longest, 282 pm, closely followed by that of Pd, 280 pm. In order to accommodate the species which shorter C–C bonds, the surface metal atoms shift above the crystal plane: the longer the M–M distance of the bulk metal, the higher the surface atom shifts (Sections 4.1.4, 4.1.5). These changes result in higher deformation energies for the surfaces where M–M distances are longer. As the deformation energies are higher for the adsorbates, the trend of the interaction energies, E_{int} , follow the trend of the adsorbate deformation energies, $\Delta E(C_2H_x)$.

The average displacement of the metal atoms at the top layer upon adsorption has also been investigated. The average displacement of the atoms increases with decreasing H content of the hydrocarbon species and the deformation energies increase exponentially with increasing average displacement, see Figure 5.2.

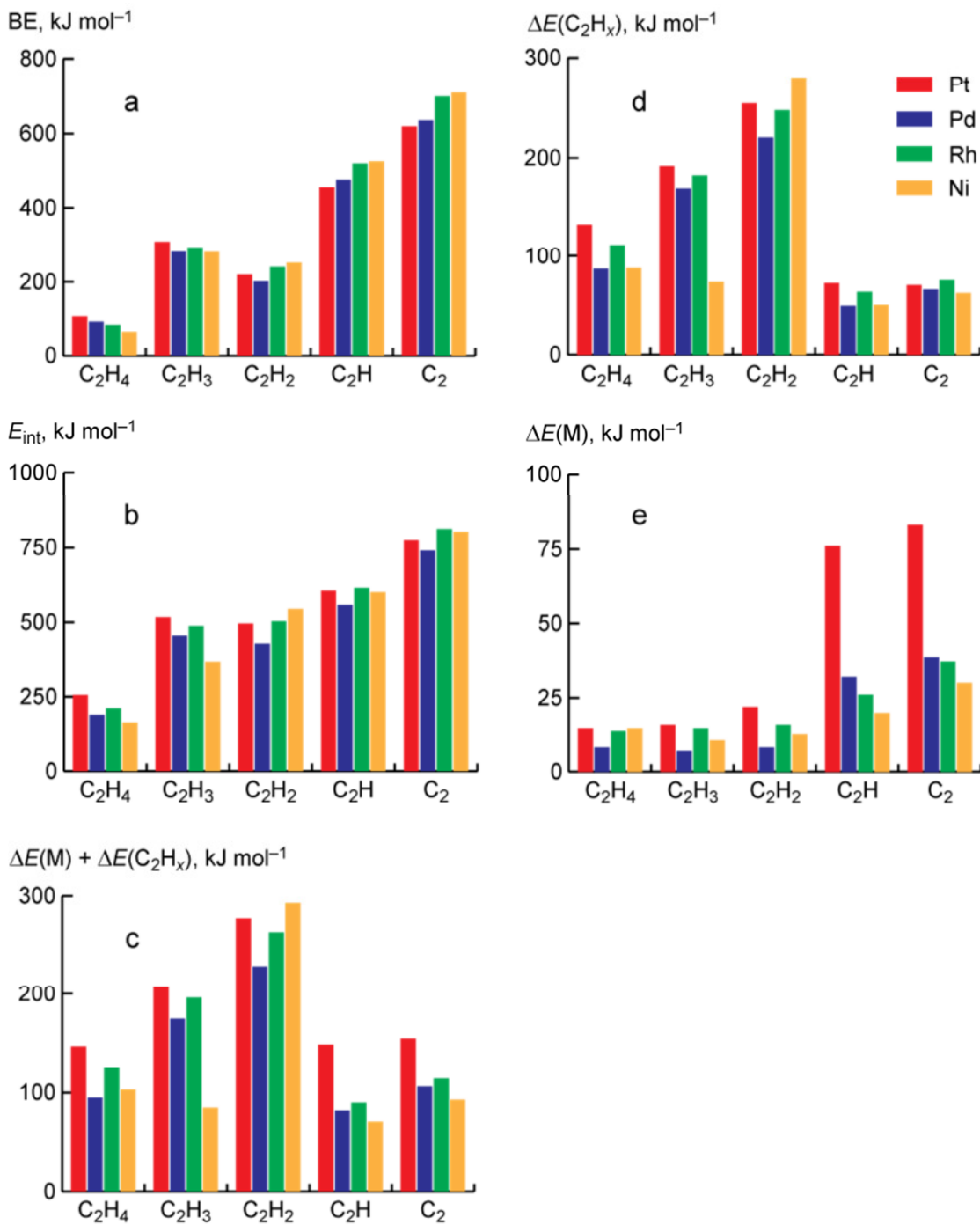


Figure 5.1 Characteristic energies (kJ mol^{-1}) of the adsorbates on four metal surfaces:
 (a) binding energies: BE, (b) metal–adsorbate interaction: E_{int} , (c) total deformation energies of the surface and the hydrocarbon species due to adsorption: $\Delta E(\text{M}) + \Delta E(\text{C}_2\text{H}_x)$, (d) deformation energies of the hydrocarbon species: $\Delta E(\text{C}_2\text{H}_x)$, (e) deformation energies of the surface: $\Delta E(\text{M})$.

Table 5.1 Energy characteristics (kJ mol^{-1}) of C_nH_x ($n = 1 - 2$, $x = 0 - 4$) at 1/9 coverage on M(111) (M = Pt, Pd, Rh, Ni)

| | | BE^a | E_{int}^b | $\Delta E(\text{M})^c$ | $\Delta E(\text{C}_2\text{H}_x)^d$ |
|------------------------|----|---------------|--------------------|------------------------|------------------------------------|
| C_2H_4 | Pd | 94 | 190 | 8 | 87 |
| | Pt | 109 | 256 | 15 | 132 |
| | Rh | 86 | 212 | 14 | 112 |
| | Ni | 63 | 166 | 15 | 88 |
| C_2H_3 | Pd | 281 | 456 | 7 | 168 |
| | Pt | 309 | 517 | 16 | 192 |
| | Rh | 293 | 488 | 15 | 181 |
| | Ni | 280 | 365 | 11 | 74 |
| C_2H_2 | Pd | 202 | 430 | 8 | 220 |
| | Pt | 220 | 496 | 22 | 254 |
| | Rh | 240 | 503 | 16 | 247 |
| | Ni | 251 | 543 | 13 | 280 |
| C_2H | Pd | 474 | 556 | 32 | 50 |
| | Pt | 454 | 603 | 76 | 73 |
| | Rh | 522 | 612 | 26 | 64 |
| | Ni | 527 | 598 | 20 | 51 |
| C_2 | Pd | 635 | 741 | 39 | 67 |
| | Pt | 619 | 774 | 83 | 71 |
| | Rh | 698 | 811 | 37 | 76 |
| | Ni | 708 | 801 | 30 | 63 |
| C(fcc) | Pd | 684 | 704 | 20 | |
| | Pt | 695 | 732 | 37 | |
| | Rh | 690 | 718 | 28 | |
| | Ni | 668 | 683 | 15 | |
| C(hcp) | Pd | 684 | 696 | 12 | |
| | Pt | 678 | 700 | 22 | |
| | Rh | 709 | 727 | 18 | |
| | Ni | 674 | 688 | 14 | |

^a Binding energy of C_nH_x . ^b Interaction energy of C_nH_x . ^c Deformation energy of the metal surface. ^d Deformation energy of the adsorbate. For the definition of the energies the reader is referred to Section 5.1.

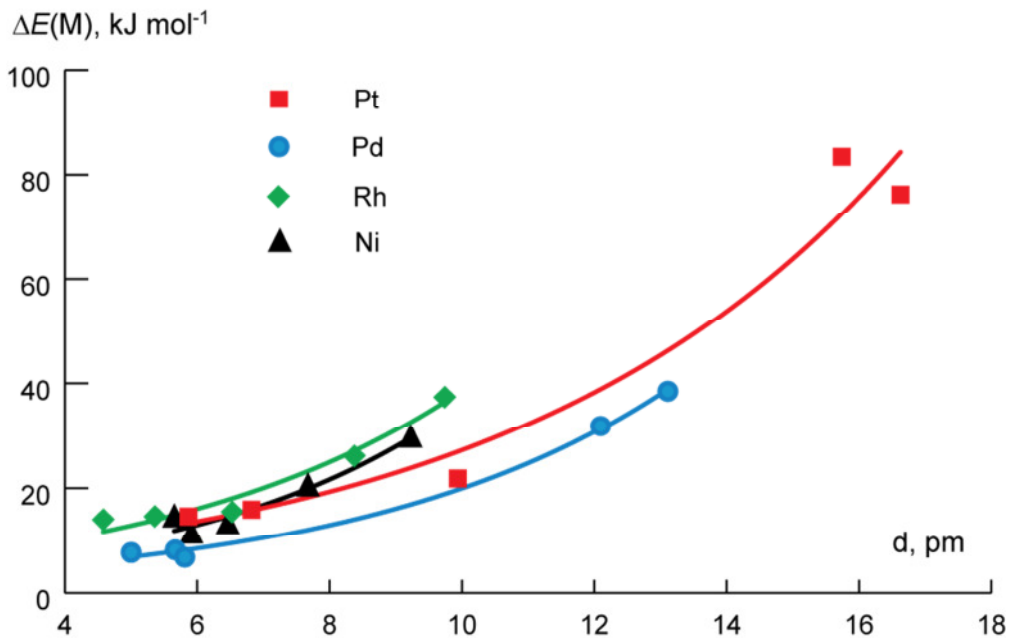


Figure 5.2 Exponential correlation of deformation energies of the surfaces, $\Delta E(M)$ (kJ mol^{-1}), as a function of the average displacements of the metal atoms at the top layer, d (pm): Pt: $(4.93 \pm 2.52) \times \exp[(0.17 \pm 0.03)d]$, $r = 0.98$; Pd: $(2.35 \pm 0.30) \times \exp[(0.21 \pm 0.01)d]$, $r = 1.00$; Rh: $(4.35 \pm 0.93) \times \exp[(0.22 \pm 0.02)d]$, $r = 0.98$; Ni: $(2.87 \pm 0.77) \times \exp[(0.25 \pm 0.03)d]$, $r = 0.97$.

5.2. Barriers and reaction energies

All geometric and energetic properties of the five reactions of interest are listed in Table 4.7. The energy profiles of the reactions are also depicted in Figure 5.3, the energy reference being ethylene in the gas phase and the clean metal surface. When the barriers of the reactions are considered, the reactions can be classified in two groups: the C_2H_x species with high H content ($x = 3, 4$) form one group and the species with low H content ($x = 0 - 2$) the other one. The barriers of the reactions of the first group are $\sim 50 \text{ kJ mol}^{-1}$ lower than those of the second group. Within this first group, dehydrogenation of the vinyl species requires overcoming the lowest barriers on all metals, $21 - 85 \text{ kJ mol}^{-1}$. The barriers increase significantly at the last dehydrogenation step, ranging between 131 kJ mol^{-1} and 154 kJ mol^{-1} .

The reaction energies also behave similarly to the activation barriers. For the two dehydrogenation reactions of ethylene and vinyl the conversions are $\sim 30 \text{ kJ mol}^{-1}$ more exothermic than the last two dehydrogenation steps, those of acetylene and ethynyl. This is in line with the Brønsted–Evans–Polanyi (BEP) relationship,^{118,119} to be discussed in more detail in Section 5.3. The dehydrogenation step of vinyl to acetylene is the most exothermic step, overcoming the lowest barriers, Table 4.7 and Figure 5.3. The most exothermic

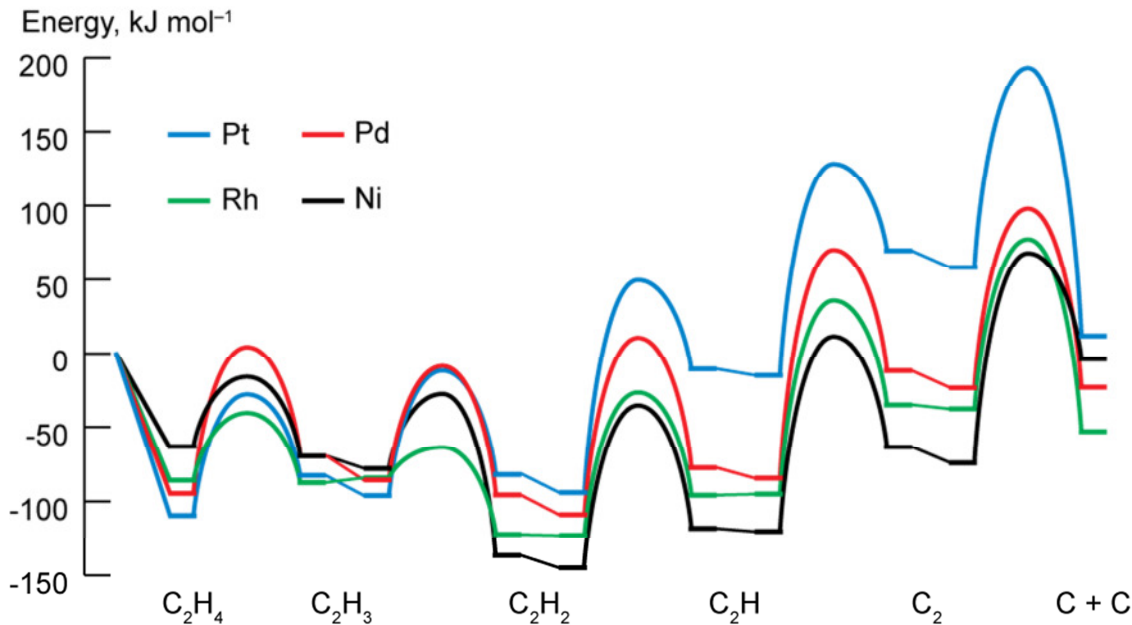


Figure 5.3 Energy profiles of the model ethylene decomposition on M(111) surfaces (M = Pd, Pt, Ni, and Rh). Energies are given with respect to ethylene in the gas phase and the corresponding clean optimized M(111) surface. Arches represent the transition states; straight lines connect the energies of the products (coadsorbed with hydrogen in the same unit cell) to energies of species with hydrogen at (formal) infinite separation.

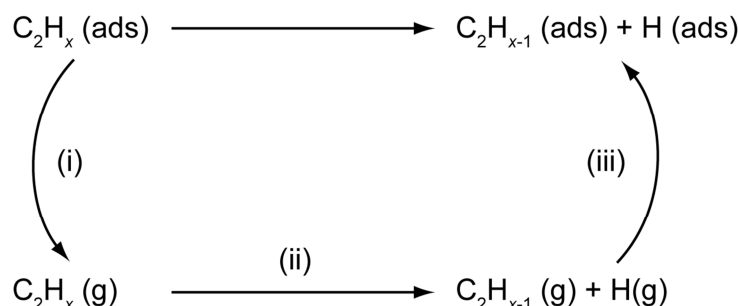
dehydrogenation step is the one occurring over Ni(111) with reaction energy of -58 kJ mol^{-1} . Although this step is still endothermic on Pt(111) surface with 14 kJ mol^{-1} , it has the lowest reaction energy out of all the dehydrogenation reactions occurring over this surface. A recent experiment by Lorenz et al.⁸⁹ showed that ethylene adsorbed on Ni(111) converts to carbon with acetylene observed as intermediate. This finding confirms the easier conversion at the two steps resulting in acetylene and as expected, with increasing barriers, the conversion speed drops. As can be seen in Figure 5.3, adsorbed acetylene is the lowest-lying state of the energy profiles. This statement is also true for Pd, but it has been shown^{20,22} that there are reactions of vinyl, such as dehydrogenation at the other carbon resulting in vinylidene or hydrogenation to ethylidene, that have lower activation barriers. The last reaction calculated is the C–C bond breaking of the carbon dimer. The backwards reaction, the formation of a C₂ species, is of great interest as this species can be regarded as precursor of graphene or coke formation on the metal surfaces. The barriers of C₂ formation are high on Pt(111), Pd(111), and Rh(111), 181, 120 and 129 kJ mol^{-1} , respectively, while the barrier on Ni(111) is significantly lower, 71 kJ mol^{-1} . The reaction on Ni(111) becomes exothermic, -71 kJ mol^{-1} , thus also favoring the formation of C₂ species. The propensity of base metals to form

carbonaceous depositions easier than noble metals, implied by these results, has been established before⁴³ and agrees with previous experimental^{120,121} and theoretical results.^{113,121}

Based on the calculated reaction energetics, the four metals under investigation can be divided into two groups. On Ni(111) and Rh(111) the dehydrogenation reactions are more exothermic going over lower barriers than the corresponding processes on Pd(111) and Pt(111) surfaces, Table 4.7. The most active metal of the set is Rh, on which the dehydrogenation barriers are even lower than those on Ni, by up to 29 kJ mol⁻¹, although the reactions are more exothermic on Ni surfaces, by up to 21 kJ mol⁻¹. Rh is also more active in C₂ dissociation with an activation barrier of 113 kJ mol⁻¹ compared to 142 kJ mol⁻¹ on the Ni(111) surface. However, the largest energy release in a C₂ dissociation occurs on Pt(111), 46 kJ mol⁻¹, but over a higher barrier, 135 kJ mol⁻¹, than on Rh.

As in Section 5.1, the binding energies were analyzed by decomposing them into various partial contributions. The conversion of the reactant adsorbed on the surface to the products adsorbed on the surface can be described by the thermodynamic cycle depicted in Scheme 5.1, which consists of the following steps: (i) desorption of the reactant from the surface, (ii) reaction in the gas phase, and (iii) adsorption of the products back on the surface.

Considering the processes listed in the thermodynamic cycle, the reaction energies of the dehydrogenation steps under investigation can be thought of a combination of three energies on the assumption that the species are at an “infinite separation”. The first one is the difference between the binding energies of the reactant and the product hydrocarbon species, $\Delta BE(C_2H_x \rightarrow C_2H_{x-1}) = BE(C_2H_{x-1}) - BE(C_2H_x)$, the second is the reaction energy in the gas phase, $\Delta E(C_2H_x \rightarrow C_2H_{x-1})$, and the third is the binding energy of a hydrogen atom, BE(H). The four dehydrogenation steps from ethylene down to a carbon dimer in the gas phase are highly endothermic; 479, 180, 580 and 505 kJ mol⁻¹, respectively. Except for the second dehydrogenation step, the dehydrogenation reactions are very unfavorable in the gas phase,



Scheme 5.1 Thermodynamic cycle elements of the surface reaction

the energies being 479–580 kJ mol⁻¹. The second dehydrogenation step concerns vinyl dehydrogenation to form acetylene, which is a stable species in the gas phase. This is the primary reason for the lower endothermicity of this step compared to the steps forming unstable product hydrocarbon species, C₂H_x, in the gas phase. As the binding energies of the products are higher on the surfaces than the binding energies of the reactants, these high reaction energies in the gas phase are somewhat compensated. The first energy contribution listed above, the difference of the binding energies, $\Delta BE(C_2H_x \rightarrow C_2H_{x-1})$, of the various reactants for $x = 4 - 1$ range from 187 to 217 kJ mol⁻¹ for ethylene, from -89 to -29 kJ mol⁻¹ for vinyl, from 234 to 282 kJ mol⁻¹ for acetylene, and from 161 to 181 kJ mol⁻¹ for ethynyl. Again, the second step, C₂H₃ → C₂H₂, being exothermic, is an exception, as the binding energy of acetylene on the surface is not higher than that of vinyl due to stable gas phase species. This investigation is solely based on the hydrocarbon species as a reactant and a product, on both sides of reactions. These results show that the binding energy of an H atom does not affect substantially the reaction energies.

5.3. Relationship between reaction energies and activation barriers

The key point of the search for the transition states is to obtain the activation barriers and figure out plausible reaction routes. The Brønsted–Evans–Polanyi relationship (BEP) suggests that activation barriers of reactions of similar character correlate linearly with the corresponding reaction energies.^{118,119} Once such a relationship is established, one may estimate approximate activation barriers from the energies of the corresponding reactant and product states. Recent studies demonstrated that BEP relationships also hold in heterogeneous catalysis.^{47,104–106}

Figure 5.4a shows the relationship between the activation barriers and the reaction energies for the dehydrogenation steps on the four metal surfaces. Figure 5.4b uses different values for the axes, illustrating the relationship between the “absolute” energies of the transition state, E_{TS} , and the corresponding final state, E_{FS} , measured relative to a common reference, here the initial state with ethylene in the gas phase and the corresponding clean metal surface. The fits of the linear relationship to the actual energies demonstrate the relationships hold well in both cases for the four transition metal surfaces investigated. The close fit of the final state energies and the transition state energies proposes that the latter are of a “late” character,¹²² matching the conclusions discussed for several transition states in Section 4.2. The relationship that is found here between the reaction energies and the activation barriers, $E_a = (0.91 \pm 0.10) E_r + (73.67 \pm 4.72)$ in kJ mol⁻¹ ($r= 0.92$), is very close

to the one calculated earlier,¹²³ $E_a = (0.92 \pm 0.05) E_r + (84.26 \pm 4.84)$ ($r= 0.96$), from a study that incorporated dehydrogenation from C and O atoms.

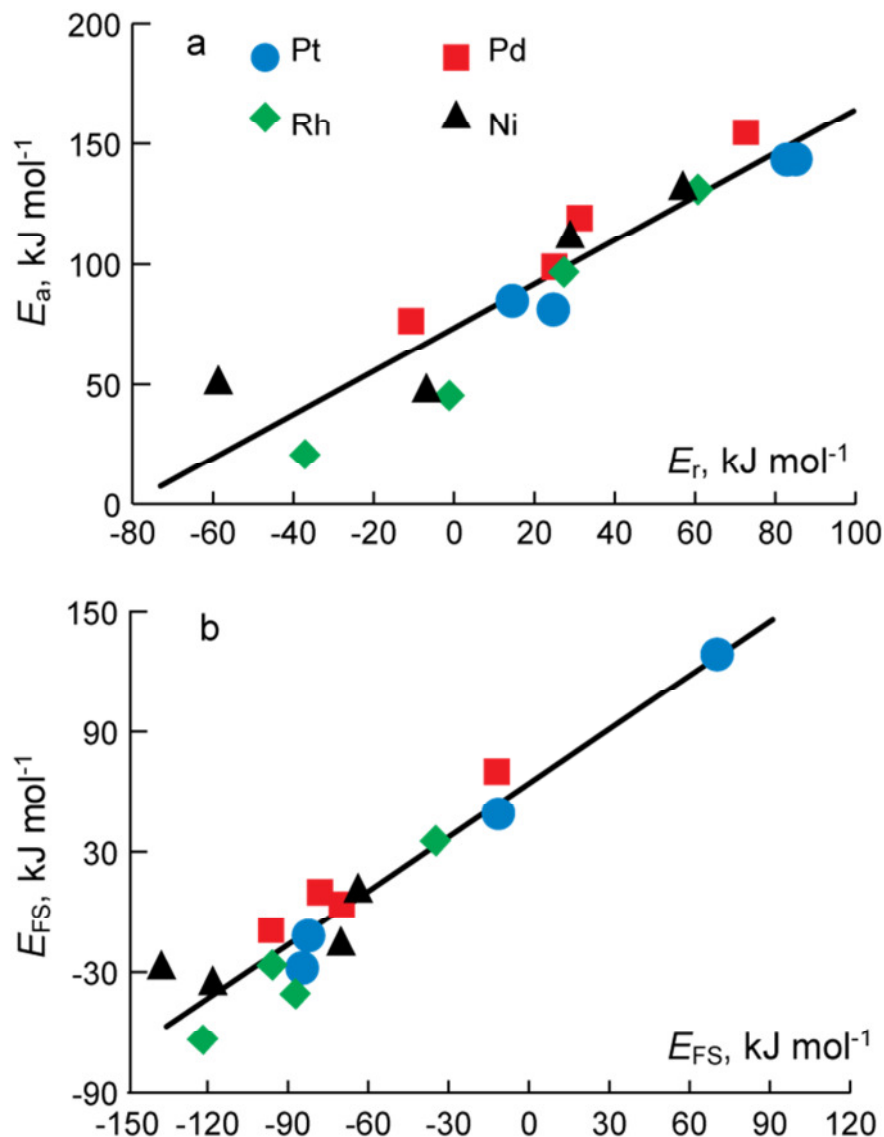


Figure 5.4 Linear relationship between (a) reaction energies E_r and activation barriers E_a (in kJ mol^{-1}) of the four dehydrogenation steps starting from ethylene, studied here on the four metal surfaces M(111), M = Pt, Pd, Rh, and Ni: $E_a = (0.91 \pm 0.10) E_r + (73.67 \pm 4.72)$; $r = 0.92$, and (b) “absolute” energies (see text) of the products E_{FS} and the transition states E_{TS} : $E_{TS} = (0.90 \pm 0.08) E_{FS} + (64.33 \pm 6.65)$; $r = 0.95$.

5.4. Coverage effect

The coverage effect described here does not refer to the number of adsorbed species per surface atom, referred to as 1/9, 1/4, and 1/3 coverages in the present study, but to the effect of lateral forces between coadsorbed species in the product state. This will be achieved by investigating two reaction energies calculated: (a) taking the energy of the product state from a calculation where both species are adsorbed in the same unit cell (3×3), thus making the effective coverage of this state 2/9, and (b) taking the energy of the product state as the sum of the individual energies of each product at 1/9 coverage, assuming that they are adsorbed on the surface but are formally at “infinite separation”. Both values are listed in Table 4.7 as E_r and E_r^{inf} , respectively. The effect is most prominent in the case of C₂ decomposition, while the coadsorption of two C atoms in the final state has a huge lateral repulsion effect. Hence the reaction energies drop by 34–64 kJ mol⁻¹ on all metals when the C atoms of the product state are assumed to be infinitely separated. For the dehydrogenation reactions, this results in an energy change of at most 16 kJ mol⁻¹ energy change when H and C₂H_x ($x = 0 – 3$) are taken to be at infinite separation.

The effect of coverage on the reaction energies changes depending on the metal, generally in the order Pd > Pt > Ni > Rh, see Table 4.7 and Figure 5.3. In most cases, the effect is similar on Pd, Pt, and Ni, but on the Rh surface it is almost negligible. For the dehydrogenation reactions on Rh, the change is only 1–2 kJ mol⁻¹, for the others the range is from 3 to 16 kJ mol⁻¹. As the steric effects should be comparable for these metals, the electronic interactions through the surface might cause the attractive lateral interaction in the case of Rh.

The coverage effect on barriers was not examined in the present work. Previous studies^{18,20,21} dealing with transition state searches of ethylene transformations at different coverages, where comparable results at 1/9 coverage with the current study were obtained, stated that barriers increase by 3–30 kJ mol⁻¹ when the surface coverage is increased from 1/9 to 1/3.

5.5. Limitations of the models used

The chain of reactions investigated here, four successive dehydrogenation steps starting from ethylene and a final C–C bond scission, is just a small section of the various possible conversions in the network of ethylene decomposition, as has been set in a previous work on Pd(111) surface.²² The dehydrogenation of ethylene to vinyl is the crucial, rate-limiting step during ethylene conversion to ethylidyne on Pd(111),^{18,20,82} and an important

step of the same conversion on Pt(111).^{21,82} Acetylene hydrogenation to ethane has also been of much interest in catalysis research, and is accepted to follow the steps $\text{C}_2\text{H}_2 \rightarrow \text{C}_2\text{H}_3 \rightarrow \text{C}_2\text{H}_4$.²³ From previous studies, it has been concluded that on Pt and Pd(111) surfaces C–C bond breaking occurs easier for the hydrocarbons containing less H atoms.²² Here the only C–C bond breaking step considered was that of the species with no H atoms, the carbon dimer. However the possibility of a C–C bond breaking at an earlier step for a hydrocarbon species containing more H atoms should not be excluded. Podkolzin et al.¹⁰⁸ reported a Monte Carlo model study based on energies calculated by DFT for reactions of C_2H_x ($x = 0 - 6$) on Pt(111) and Pt(211). That study showed that the C–C bond breaking of ethane at high H_2 pressure proceeds primarily through C_2H_5 species.

Another limitation of the model is based on the fact that only the flat surfaces of the metals, M(111), have been explored. These are idealized surfaces, but surface defects such as steps are known to be more reactive than flat surfaces.^{44,124-126} For instance, steps and other surface defects have been shown to favor C–C bond breaking on Ni.⁵⁵ Also for the reaction $\text{C}_2\text{H}_4 \rightarrow \text{CH}_2 + \text{CH}_2$, the stepped Pd surface, Pd(211), was determined to be more active than the flat surface, the barrier on the former being 163 kJ mol^{-1} compared to 204 kJ mol^{-1} on the latter.^{71,76} However the barriers of the reaction steps $\text{C}_2\text{H} \rightarrow \text{C} + \text{CH}$ and $\text{C}_2 \rightarrow \text{C} + \text{C}$ are quite similar on flat and stepped surfaces of Pd; the barrier of the latter reaction is even lower on the flat surface. Yet, the barriers of simple hydrogenation/dehydrogenation steps are found to be close on both surfaces.^{71,76}

6. Conclusions

The first part of the thesis dealt with the decomposition of ethylene within a model chain of reactions on the flat surfaces of four transition metals, M = Pt, Pd, Rh, and Ni, via periodic slab model density functional calculation at the GGA level. The reaction chain is composed of five steps: $\text{CH}_2\text{CH}_2 \rightarrow \text{CH}_2\text{CH}$; $\text{CH}_2\text{CH} \rightarrow \text{CHCH}$; $\text{CHCH} \rightarrow \text{CHC}$; $\text{CHC} \rightarrow \text{CC}$; $\text{CC} \rightarrow \text{C} + \text{C}$. Among the intermediates, ethylene and acetylene, the closed-shell species, bind weakest, adsorption energies ranging from 33 to 109 kJ mol^{-1} for the former (see Table 4.1) and from 179 to 251 kJ mol^{-1} for the latter (see Table 4.3). The binding energies of the remaining open-shell species are higher, 247 – 708 kJ mol^{-1} , and increase as the H content of the species decreases.

On all metal surfaces studied, the binding energies of the species increase in the order: $\text{C}_2\text{H}_4 < \text{C}_2\text{H}_2 < \text{C}_2\text{H}_3 < \text{C}_2\text{H} < \text{C}_2 < \text{C}$. The higher H content species, C_2H_4 and C_2H_3 , bind strongest on the Pt(111) surface, whereas the lower H content species bind stronger on

Rh(111) or Ni(111) surfaces. When the coverage is increased from 1/9 to 1/3, the binding energies drop due to repulsive lateral interactions. This coverage effect is least prominent on the Rh(111) surface. Also in the case of C₂H and C₂, the binding energies at 1/3 coverage are higher than those at 1/4 coverage due to the formation of linear chains of metal and C atoms. In consequence, the surface layer of metal atoms is distorted, causing them to bind less to the second-layer atoms, but in turn binding stronger with the adsorbates.

The activation barriers and the reaction energies of the dehydrogenation reactions reveal that such type of conversions will occur more readily on Ni(111) or Rh(111) than on Pd(111) or Pt(111). Trends of reaction energies and barriers on the various metals are controlled to a large extent by the difference of the bonding strength between the reactants and the product hydrocarbon species. The binding energy of hydrogen does not influence these trends, probably due to the relatively small variations of the bonding strength of hydrogen over the metals studied. Among all four metals, Ni is the most available hence the cheapest metal. Thus, it is an attractive replacement for the other metals as a catalyst in various hydrocarbon conversions including dehydrogenations. However it should be kept in mind that Ni is the most prone to coke formation, which strongly reduces its catalytic behavior. Several studies aim to improve the catalytic properties of Ni-based catalysts against coke formation.^{86,113}

The first two steps of dehydrogenation, ethylene dehydrogenation to vinyl and vinyl dehydrogenation to acetylene, are kinetically and thermodynamically more facile than the successive dehydrogenation steps for all of the four metals. The breaking of C–C bond, while covered here to happen at the carbon dimer, might also take place one dehydrogenation step earlier, as C–C bond breaking of ethynyl, as the barrier and the reaction energies for dehydrogenation increase remarkably.

IV. PART II - CONVERSION OF SIMPLE ALCOHOLS ON PLATINUM SURFACES

7. The choice of hydrogen as an energy carrier

Hydrogen is the simplest and the most abundant element in the universe,¹²⁷ however it is not easily accessible; it is found only in combination with other elements. The fact that it can serve two purposes – as a fuel and as a chemical – makes it a very popular choice as a reactant and an energy carrier.¹²⁸ Hydrogen can be used as a raw material in the manufacture of ammonia within a mixture of nitrogen (Haber-Bosch process),¹²⁹ in synthesis of methanol,¹³⁰ liquid hydrocarbons (Fischer-Tropsch),¹³¹ or higher alcohols with a mixture of carbon oxides,¹³² and in hydrogenation of oils to form fats. As a fuel it can be used in internal combustion engines to obtain directly mechanical energy or in fuel cells to be converted into water and electricity, which can be further converted to obtain mechanical energy. Fuel cell power plants are used in the Space Shuttle to generate all the electrical energy necessary, and the by-product water is stored as potable water.¹³³

Hydrogen is a very high-quality energy carrier, depicted as the future energy carrier due to its high efficiency and zero or near-zero emissions.^{129,134,135} As water is the only by-product when pure hydrogen is burnt, its use as an energy carrier reduces the CO₂ emissions. When renewable energy resources are converted into hydrogen, it is an energy source to be utilized to meet most energy needs, especially in transportation and mobile sectors.^{127,135}

7.1. Chemical background on hydrogen production

In general, hydrogen production technologies are gathered in three categories; thermal, electrolytic and photolytic processes.¹³⁶ Figure 7.1 shows the distribution of resources for hydrogen production in 2005; 96% of hydrogen produced is derived from fossil fuels.¹³⁷ An overview of the current hydrogen production technologies will be given based on the primary energy sources used for the production.

7.1.1. *Hydrogen from fossil fuels*

Various papers, books, and reviews exist that extensively report on hydrogen production technologies. The following discussion of hydrogen production from fossil fuels is mainly based on the reviews of Holladay et al.¹³⁸ and Navarro et al.¹³⁹

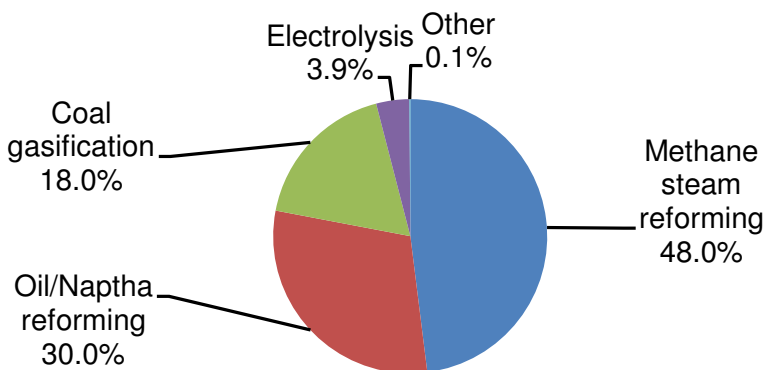
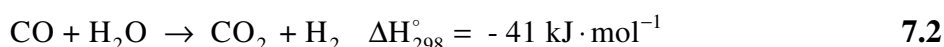
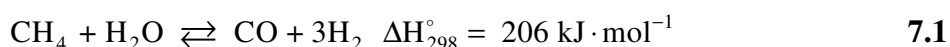


Figure 7.1 Main production routes of hydrogen.¹³⁷

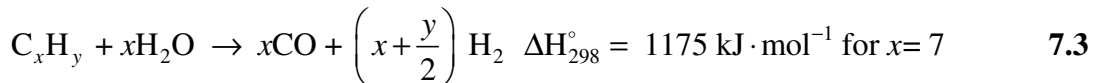
The main fraction of industrial hydrogen is currently produced from fossil fuels. Steam reforming (SR) of natural gas (mostly methane) is the globally most common and the most prominent process to obtain hydrogen from fossil fuels. It is also the choice when large amounts of H₂ is to be produced.¹⁴⁰ It is one of the thermal processes in hydrogen production. The overall reactions taking place in SR of natural gas into hydrogen are as follows:



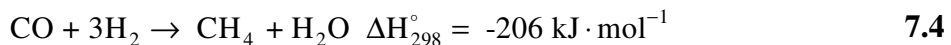
The first reaction, 7.1, is the SR of methane followed by the WGS reaction, 7.2. As the SR reaction is reversible and endothermic, it is carried out at high temperatures, ~800°C, and low pressures, 3-25 bar. The exothermic WGS reaction further produces hydrogen converting CO into CO₂. The stream is then sent to pressure swing adsorption (PSA), where a hydrogen purity of 99.9 vol.% can be achieved by removing the CO₂ and the other impurities.¹²⁹

The catalysts used in SR of methane are Group VIII metals supported on different oxide-supports. In this set the activities of Rh and Ru are the highest,^{141,142} however Ni is the most widely used metal. Although it is more susceptible to deactivation and less active in steam reforming, the cost advantage has made it the choice of the industry.¹³ Non-metallic catalysts, e.g. molybdenum carbide and tungsten carbide, have also been investigated, but they cannot match the activities and stabilities of the Group VIII metals.^{143,144}

Steam reforming of naphtha, introduced later than that of methane, is a process technology that is more flexible in terms of the feedstock. This becomes an important advantage especially at conditions where natural gas is not available. The reforming reaction is shown in 7.3.

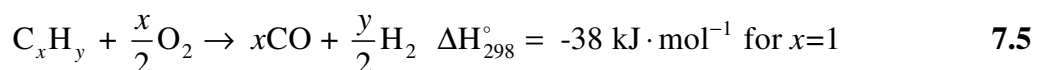


The reaction heat shows that the heat requirement per carbon atom is less for the conversion of n-heptane than it is for methane conversion, which in turn means operational duty under similar conditions is less for naphtha than for methane.¹⁴⁵ The adsorbed hydrocarbon is converted to adsorbed C₁ species via subsequent C-C bond breakings without any other intermediates forming. Reaction 7.3 couples with the WGS reaction shown in 7.2, and also with methanation reaction:



This reaction supplies the heat required while removing the CO adsorbed on the surface, however it consumes three molecules of H₂ per molecule of CO reacted. Reactivities of the hydrocarbons vary: longer-chain hydrocarbons and olefins perform better than methane whereas the aromatics show similar performance with methane due to the stable resonance of the rings.¹³⁹

Another possibility to produce hydrogen from a hydrocarbon feed is partial oxidation (POX). Apart from the reviews mentioned above,^{138,139} especially the review of Trimm and Önsan¹⁴⁶ about partial oxidation reactions provides a thorough resource for research on this topic. This process entails lower energy cost as it does not require costly superheated steam as in SR processes. Partial oxidation reaction, reaction 7.5, is energetically less demanding than steam reforming, reaction 7.1, and proceeds faster; however less H₂ is produced per hydrocarbon reacted.



This reaction can be performed with or without the presence of a catalyst. When no catalyst is present, the temperature should be kept at high levels, ~1300-1500 °C, to achieve complete conversion and avoid soot formation.¹³ With the employment of catalysts, the operating temperature is reduced to values of ~800°C. There are mainly two mechanisms discussed: the indirect partial oxidation (IPOX) and the direct partial oxidation (DPO).^{139,146} IPOX combines the highly exothermic total oxidation of the hydrocarbon with SR and WGS, 7.1 and 7.2, respectively. The total oxidation part provides the energy to deliver the heat of the endothermic SR reaction. The product CO₂ might be reformed further to produce additional H₂. Direct partial oxidation is the partial oxidation reaction as given in 7.5 followed

by the WGS reaction. It is favored at high temperatures and short residence times as longer residence times will drive to total oxidation and hence to IPOX.¹⁴⁶

Autothermal reforming (ATR) provides another route for the partial oxidation of the hydrocarbons and is achievable in a single reformer.¹³ This makes the process very attractive for the large-scale production of hydrogen. In this process, part of methane is combusted incompletely to CO and H₂O via an exothermic reaction in the entrance region of the reactor. In the following regions the remaining methane is reacted with steam – SR of methane – and WGS takes place to convert CO into H₂ and CO₂. The ratios of oxygen to fuel and steam to carbon should be regulated very carefully to achieve the desired reaction temperature and product gas composition in ATR operation.¹³

The hydrocarbon can directly be decomposed to hydrogen and carbon without presence of any other reactant via pyrolysis.¹⁴⁷ For the decomposition of methane the energy requirement per H₂ produced is less than in SR. The lack of air or water in the stream results with significant decrease in the emissions as no carbon oxides are formed.¹⁴⁷ If necessary the heat of the reaction can be supplied by combusting only ~10% of the methane feed; however this would produce CO₂ in small amounts. The carbon formed accumulates mostly as filaments on the surfaces of metallic and bimetallic catalysts, causing deactivation.¹³⁹

Hydrogen produced by coal gasification takes up the second biggest production volume after reforming processes, see Figure 7.1. It is a versatile process in terms of feedstock, and it takes place at high temperatures, 900-1100°C, and moderate pressures, 5-10 bar.¹³⁹ Main reactions occurring are pyrolysis producing tar, steam/dry reforming of tar, partial oxidation of hydrocarbons, WGS and methanation. Several catalysts were found to be active and selective in reactions in gasification process; Fe₂O₃/Fe₃O₄ catalyzing the whole process, Ni catalyzing dry reforming, WGS and methanation, Ca-based catalysts that decrease the reaction temperature. The low cost of the coal is the main attraction of this process;^{148,149} however it has to be coupled with CO₂ sequestration to achieve acceptable CO₂ emissions.^{136,148}

7.1.2. *Hydrogen from water*

In their review of 2009, Holladay et al.¹³⁸ provided extensive coverage of water splitting as a hydrogen resource. That work was used as a guideline for this section and as a gateway to relevant publications in this field.

Jules Verne refers to water as “the coal of the future” due to the inexhaustible energy source of its constituents – hydrogen and oxygen – in his book *The Mysterious Island* back in

1874.^{149,150} Hence the concept of obtaining hydrogen from water is not new; the commercial water splitting to make hydrogen and oxygen dates back to the 1890s. In the current production volume, electrolysis of water takes 3.9% and is the most capacious process to produce hydrogen from renewable resources.¹³⁷

Electrolysis achieves hydrogen and oxygen production via passing an electric current through two electrodes immersed in water. This system is currently used in small scale and research for larger scales is performed.¹³⁶ The emissions from electrolysis depend on how the electricity is produced to run the electrolyzer as the only products of the system itself are O₂ and H₂. Three main types of electrolyzers are employed: alkaline based, proton exchange membrane (PEM), and solid oxide electrolyzer cell (SOEC). Alkaline electrolyzers, the most common ones, are made up of Ni or Cu coated with metal oxides at the anode separated by an alkaline solution from the Ni coated with a catalytic coating such as Pt at the cathode. They work on the principle of splitting water at the cathode forming H₂ and OH⁻ and transferring the OH⁻ through the electrolytic material to the anode to form O₂. As the H₂ formed stays in the alkaline electrolyte, a separation process follows.¹³⁸ The PEM electrolyzers utilize a solid polymer membrane, e.g., Nafion, in between the anode, e.g., porous Ti coated with Ir, Ru, IrO₂ or RuO₂, and the cathode, e.g., porous C element with Pt/C coating.¹⁵¹ H₂O splits at low temperatures, 120-130°C, at the anode to O₂ and H⁺, only protons travel through the membrane as it is impermeable to gases, and H₂ is produced at a very high purity at the cathode.¹⁵¹ SOEC is another solid state electrolyte performing at higher temperatures handling steam instead of water; thus decreasing the required electrical energy by replacing it with thermal energy. In this type of electrolyzers O²⁻ is the ion that is transferred through solid oxide electrolyte, e.g., fully or partially stabilized (with Y₂O₃, Sc₂O₃) zirconia, ceria doped with Gd₂O₃ or Sm₂O₃, metal doped La metal oxides.¹⁵¹ In general, electrodes are ceramic, metal, or metal-ceramic composites.¹⁵¹

Photoelectrolysis is another form of electrolysis where the energy required is obtained from sunlight using semiconductors similar to the ones employed in photovoltaics. It has been defined as a “Holy Grail” for its potential to yield a viable alternative to petroleum as a source of energy.¹⁵² The process can be performed in two separate cells for each function stepwise or they can be combined in a single nanoscale process increasing the efficiency of this integrated photochemical process.¹⁵³ The semiconductor material for that purpose should have a small band gap – below 1.7 eV but exceeding the standard potential for water 1.23 eV – for efficient adsorption, and the efficiency is directly related to the band gap.¹⁵⁴

7.1.3. *Hydrogen from biomass*

In this section, earlier processes for biomass as a resource of hydrogen are discussed. Several groups reviewed this topic. The following overview is largely based on reviews by Holladay et al.,¹³⁸ Navarro et al.,¹³⁹ Ni et al.,¹⁵⁵ and Nath and Das.¹⁵⁶

As an abundant, versatile resource, biomass is a very strong candidate considered also to produce H₂ in the near- and mid-term future.¹⁵⁷ Like in fossil fuels, most processes produce also CO₂ as a by-product but as the biomass itself consumed CO₂ as it grew, the overall amount of this greenhouse gas set free is much lower compared to fossil fuels.¹²⁹ Major resources of biomass include animal wastes, municipal solid wastes, agricultural wastes, short-rotation herbaceous species, wood wastes, crop residues, bio-solids, grass, waste from food processing, aquatic plants and algae animal wastes, and a host of other materials.¹⁵⁸ Hence these resources are renewable compared to fossil fuels and biomass is regarded as the only sustainable source of energy and carbon.¹⁵⁹ Through thermochemical or biological processes, biomass is converted either directly to H₂ or to storable intermediates which can be later processed to obtain H₂.¹⁵

Direct combustion of biomass in air has a low heat value and its by-products are pollutant emissions. In biomass liquefaction biomass is heated in water in the absence of air with or without a solvent or a catalyst, however the operational conditions are difficult to achieve and the hydrogen production is low. Hence these two processes are eliminated as the mainstream methods to obtain hydrogen in the future.¹⁵⁵

Biomass pyrolysis is a thermochemical conversion of the biomass in the absence of air at 350–500°C and 1–5 bar. In contrast to the pyrolysis of hydrocarbons a wide range of products is obtained due to the high oxygen content of biomass: in woody biomass around 50 wt.% is carbon and 45 wt.% is oxygen.¹⁶⁰ High heating rate, high temperature and long volatile phase residence time are required to achieve high H₂ production.¹⁵⁵ H₂ yield is increased by the catalytic steam reforming of the bio-oils formed in fast pyrolysis.^{161,162} The non-selectivity of the reactions along with large amounts of char formed make this process not a very attractive choice for H₂ production.¹¹

Gasification is by-far the most commercial and mature technology to produce hydrogen from biomass.^{129,138,155,156} It is a variation of pyrolysis conducted in the presence of a gasification agent, steam, oxygen and/or air, in a controlled amount.¹³⁶ At temperatures above 1000 K biomass is gasified via partial oxidation and/or steam reforming to produce mainly gases, with char and as by-product. The efficiency of the process depends on the

moisture content of the biomass as it must be vaporized, causing major energy loss.¹⁵⁸ The tar produced in the reactions might be reduced with the employment of catalysts, e.g. Rh/CeO₂/M (M=SiO₂, Al₂O₃, and ZrO₂), or additives, e.g. dolomite, olivine, char.

7.2. Hydrogen from biomass via aqueous phase reforming (APR)

As depicted in several cases, steam reforming of carbohydrates (and of hydrocarbons in the case of fossil fuels) is a widely used process, either as a stand-alone process as in steam reforming of methane or as a step in the conversion route as in biomass pyrolysis, to increase the H₂ production yield. Its coupling with WGS reactions enhance the H₂ produced. As a next step in improving the reforming reactions coupled with WGS, a recent process devised by Dumesic et al.^{11,16,17,163-166} aims at producing H₂ from biomass-based oxygenated hydrocarbons through catalytic aqueous phase reforming at temperatures around 200°C with CO₂ as the primary by-product.

The primary advantage of aqueous phase reforming (APR) of oxygenates over steam reforming of carbohydrates is the operating conditions the process takes place:^{17,167}

- The WGS reaction that converts CO into CO₂ and H₂ is also thermodynamically favorable at the same conditions, the conversion occurs in a single reactor with increased hydrogen yield.
- The lower temperatures eliminate (or minimize) undesirable decomposition reactions encountered at the higher temperatures of steam reforming.
- The energy consuming vaporization of the reactants is not required.
- The effluent can be purified to H₂-rich stream via pressure swing adsorption or membranes as the pressures, 15-50 bar, are suitable for these methods.

The selectivity, however, becomes an issue at the same low temperatures as H₂ produced might further react via methanation and/or Fischer-Tropsch to alkanes or instead of C–C bond breaking, C–O bond breaking might occur from the feedstock, ending up with alkanes as product. Figure 7.2 shows a schematic representation of the plausible reaction pathways involved in the formation of H₂ and alkanes from oxygenated hydrocarbons, with H₂ marked as a product.¹⁶ There are several different conversions taking place on the support, the metal and/or in the solution. Hence with a careful selection of each of these factors the end product might be selectively produced. APR is based on the conversion of carbohydrates with a C:O ratio of 1:1 as their thermodynamic characteristics make the reaction favorable at lower temperatures than for alkanes having the same number of carbon atoms.¹⁷

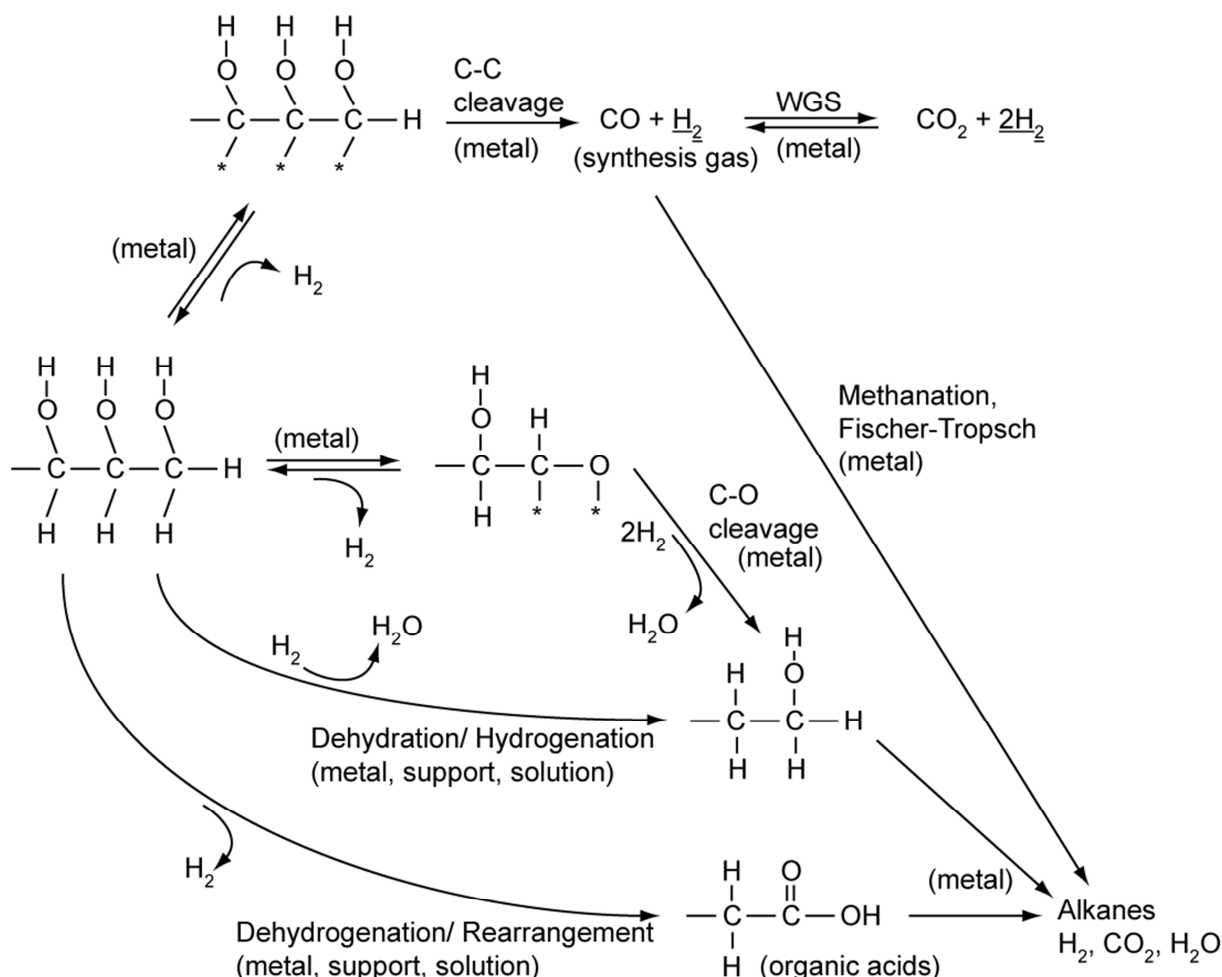


Figure 7.2 Reaction pathways for producing H₂ by reactions of oxygenated hydrocarbons with water. Adapted from Ref. 16.

7.2.1. Selectivities

Kinetic studies aimed to find a catalyst that is active in C–C bond cleavage while preserving C–O bonds; that strategy will enhance the WGS reaction while having a low activity for methanation. Among various metals, Pt and Pd – especially Pt for its higher activity in WGS – are selected as the most suitable metals to achieve all the tasks to a satisfactory extent for H₂ production. Alloying Pt with Ni, Co, or Fe supported with Al₂O₃ increases the activity of the catalyst further by decreasing the d-band center.^{11,17} More recently combining Re with Ir, Ni, Pt, and Rh proved to improve H₂ yield.^{168,169} As for the supports, Pt on Al₂O₃, ZrO₂, and TiO₂ were shown to be the most active. The selectivity dependence of H₂ or alkane production on the type of oxygenates is summarized in Figure 7.3. Polyol feeds produce H₂ more selectively, with the H₂ selectivity decreasing when the number of carbon atoms increases as the probable number of side reactions that consume

hydrogen increase. Increasing the feed concentration of sugars increases the selectivity for alkanes.¹⁷

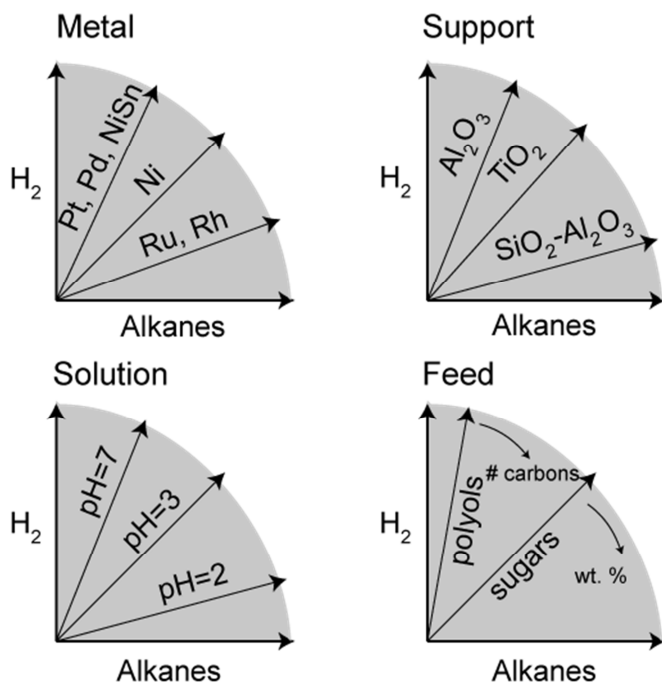


Figure 7.3 Factors important in the selectivity of aqueous phase reforming. Redrawn from Ref. 17.

7.2.2. Glycerol as feed

Glycerol is a polyol containing three hydrophilic alcoholic hydroxyl groups, which are responsible for its water solubility and hygroscopic nature.¹⁷⁰ Glycerol has been used in many studies on aqueous phase reactions.^{25,164,168,171-174} It is obtained in high amounts as by-product of two different processes as shown in Figure 7.4. During the transesterification of biocrude 10 wt. % of glycerol is produced following Scheme 7.1, making it widely and cheaply available.¹⁷⁵ Fermentation of glucose can also be regulated to obtain at least a 25 wt.% aqueous solution of glycerol.¹⁷⁶ Glycerol has become a popular model compound in APR studies as it undergoes the same type of reactions with a simpler product list than higher sugar alcohols.¹⁷¹

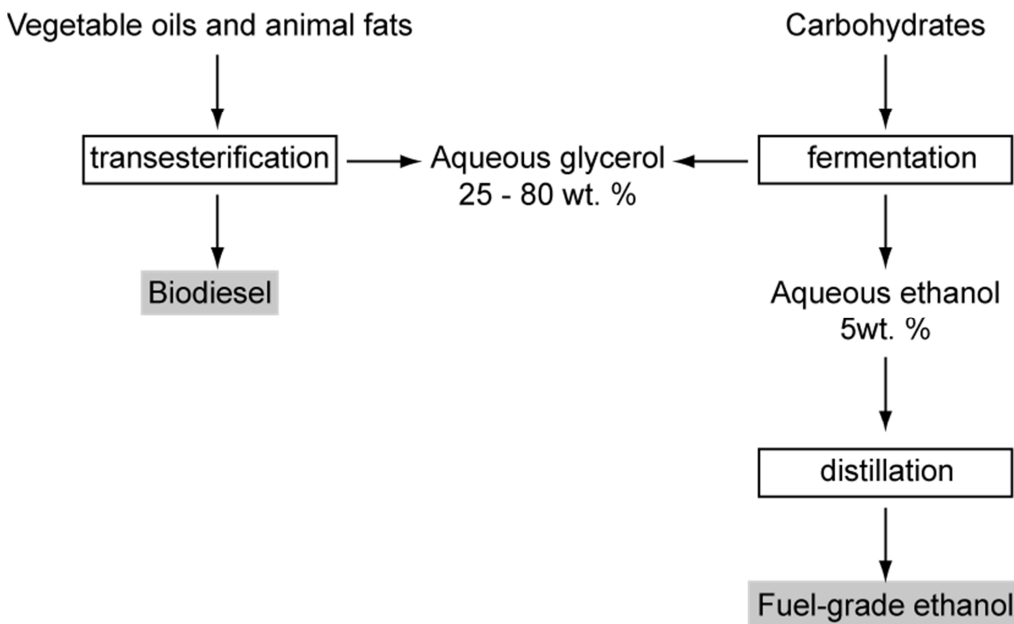
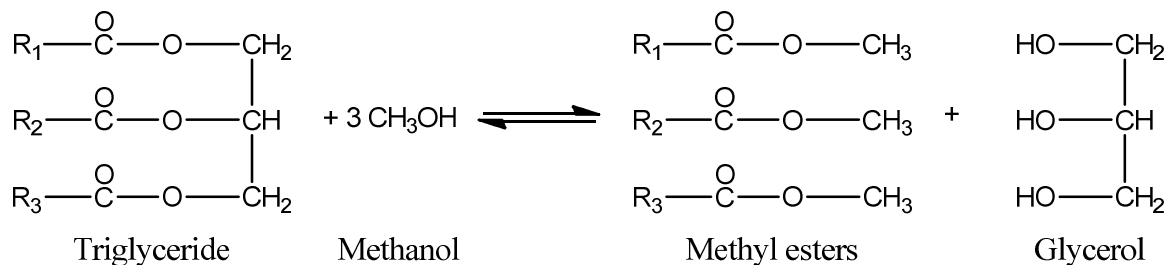


Figure 7.4 Aqueous solution of glycerol obtained as by-product of two major processes.
Adapted from Ref. 174.



Scheme 7.1. Overall reaction for biodiesel conversion; producing glycerol as by-product. R_i , $i = 1, 2, 3$, are hydrocarbon chains with 15 to 21 atoms.¹⁷⁵

The conversion of glycerol in aqueous solution on Pt metal over different supports has been studied experimentally.^{25,172,173} Among amorphous silica-alumina (ASA), γ -alumina (Al_2O_3), and silica (SiO_2) supports, the hydrogen production rate was shown to be highest on γ -alumina.¹⁷³ The γ - Al_2O_3 support and the alumina part of ASA employed converts in aqueous conditions to boehmite ($\text{Al}_2(\text{OOH})_2$) on which acidic sites exist but this material exhibits more basic Al, O, and OH sites than other types of aluminum oxides.¹⁷⁷ Glycerol conversion was also investigated in aqueous phase over Pt/ Al_2O_3 at ~ 500 K and total pressure of 26–45 bar in a 10–30% reactant aqueous solution to see which of the C–C and C–O bond cleavages take place under these conditions. Several experiments were carried out to understand the mechanism of the conversion of oxygenates – including mono-, di- and tri-alcohols in the presence and the absence of H_2 pressure. Also the effects of particle size, total pressure, and

conversion were investigated. The results of these studies show that direct hydrogenolysis of alcohols does not occur and dehydration and dehydrogenation occurring on the support and metal, respectively, are the main reactions.²⁵

In the investigations to find the reaction pathway, primary and secondary mono-alcohols, e.g. 1- and 2-propanol, were also tested on ~1.5 nm particles both in the absence and the presence of H₂. In the case of 2-propanol without H₂ pressure, the effluent consisted of acetone and propane, without any H₂ or CO₂ detection.²⁵ When H₂ is added to the stream the observed products did not change for 2-propanol.¹⁷² 1-propanol conversion under H₂ pressure however showed changes from its conversion from the case where there was H₂ present in the

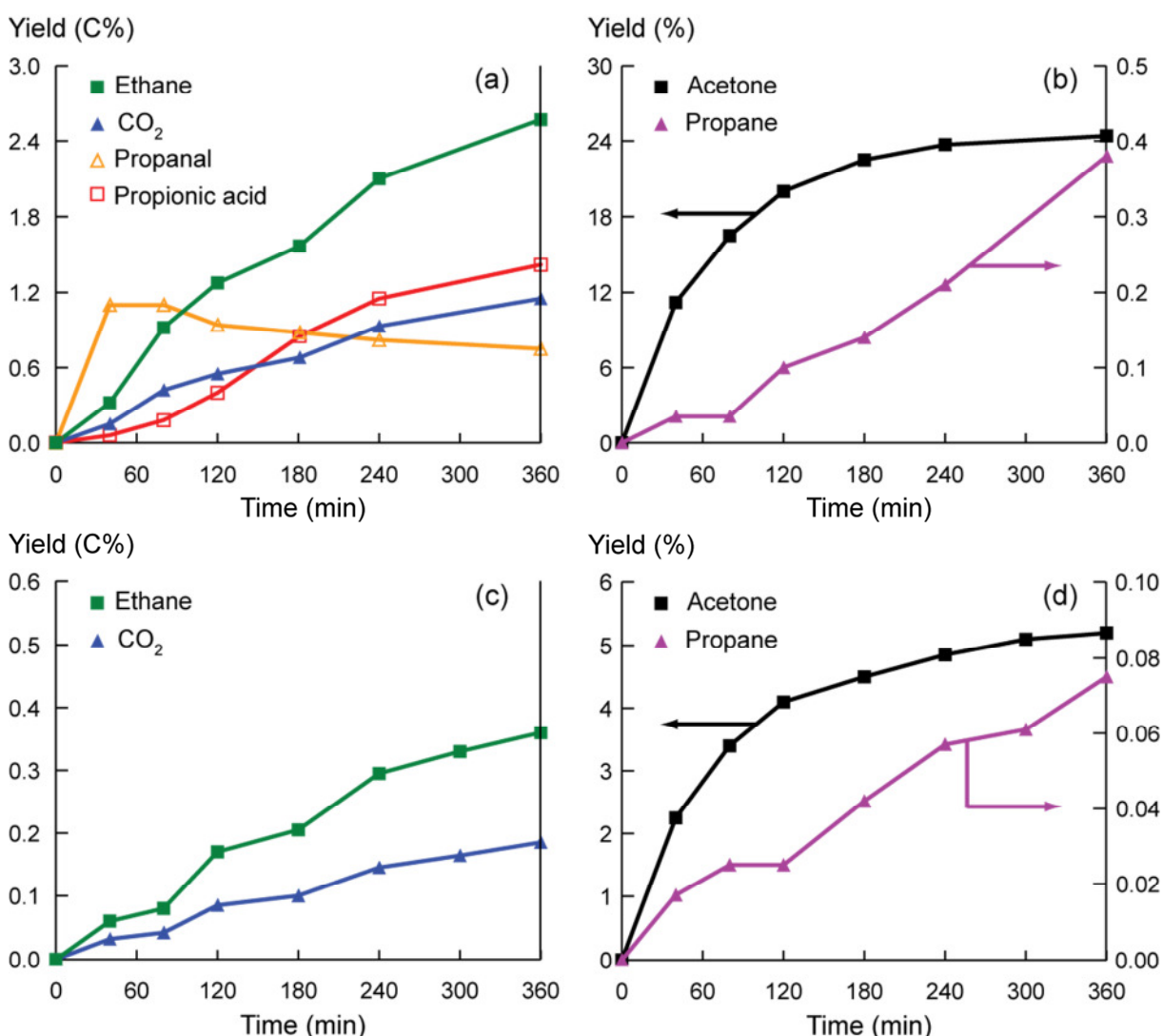


Figure 7.5 Yields from 1- and 2-propanol conversions. Upper panels in the absence of H₂ and lower panels at a total pressure of 40 bar H₂: (a), (c) on conversion of 1-propanol and (b), (d) on conversion of 2-propanol.^{25,169}

stream. The main products were the same: ethane and CO₂. In the absence of H₂, propanal and propionic acid were also detected in large amounts (cf. Figure 7.5), whereas in the case of H₂ pressure propanal was detected only in trace amounts and no trace of propionic acid was detected. Lobo et al.¹⁷⁸ also studied the reforming of 1-propanol on Pt supported over Al₂O₃, TiO₂, and Ce₂O₃ in the absence of H₂ pressure. The Pt particle size on the alumina support was on average 3.4 nm. Their results mostly agree with these of Wawrzetz et al.²⁵, however the fraction of propionic acid is higher and propane is also observed. The results from both studies point out that dehydrogenation is the dominating process taking place on the metal particle, here on Pt, and metal particle also participates in the C–C bond breaking reactions for the alcohols with terminal hydroxyl groups.

8. Dehydrogenation of 1- and 2-propanol

Batch experiments of 1- and 2-propanol led experimentalists²⁵ to consider a conversion route for these alcohols that would start with dehydrogenation. The experiments conducted at 473 K under 20 bar total pressure at 10 wt. % propanol over Pt particles of 1.5 nm average size in the absence of H₂ resulted in different conversions for the primary and the secondary alcohol. They have also run experiments with H₂ pressure¹⁷² and the resulting main compounds were the same without H₂ supplied in the reactor. Over a time span of six hours, 1-propanol was converted to ethane and CO₂ in both cases along with propanal and propionic acid when there is no H₂ in the stream, whereas acetone was the main product of 2-propanol conversion, along with a small amount of propane. From these data, it is deduced that propane is formed on the alumina support via dehydration and dehydrogenation is the only reaction that occurs on the metal surface for 2-propanol species. Experiments of 1- and 2-octanol over Pt supported by carbon¹⁷⁹ also resulted in different products; while the primary alcohol converts into aldehyde, which converting further was claimed to be blocking the active sites, the secondary alcohol reaches total conversion with the ketone as the only product. Hence the different dehydrogenation behavior of 1- and 2-alcohol under the same conditions is of primary interest regarding the intermediate that would then lead to the further conversions, e.g. C–C bond scission in the case of 1-propanol.

Computational modeling was carried out in the context of the present work to unravel the different reaction patterns of 1- and 2-propanol.

8.1. Adsorption complexes

In the following section the calculated adsorption geometries of the dehydrogenation intermediates and their binding strength on the Pt(111) surface are reported. The naming of

each species is also presented in this section. The geometries of the intermediates are depicted in Figure 8.1 and the corresponding binding energies are reported in Table 8.1.

8.1.1. Alcohols: 1- and 2-propanol, C_3H_8O

The most stable adsorption geometry of alcohols on transition metal surfaces in $\eta^1(O)$ mode, mediated via the oxygen lone pair.¹⁸⁰⁻¹⁸² The present modeling also resulted in such a propanol structure, as depicted in Figure 8.1 as **1a** for 1-propanol and **2a** for 2-propanol. As propanol is stable in the gas phase, the binding energy of 1-propanol when adsorbed on the surface is not so high, only 32 kJ mol⁻¹, and that of 2-propanol is almost the same, 28 kJ mol⁻¹. The O–Pt bond is long, 232–233 pm, due to weak interaction with the surface, see Table 8.1. The structure of the molecule does not change much from the gas phase species; the only significant difference is an elongation of the C–O distance elongation by 3–4 pm upon adsorption. In accordance with minor changes in the geometry of the structure the deformation energies are only 2 kJ mol⁻¹ and 3 kJ mol⁻¹ for 1- and 2- propanol, respectively (Table 8.1). Inspection of the deformation energies of the surfaces shows that the secondary alcohol causes more deformation on the surface than the primary alcohols. The deformation energy $\Delta E(M)$ of the substrate in the case of the secondary alcohol is 13 kJ mol⁻¹ higher than that for the primary alcohol (Table 8.1). Indeed, the secondary alcohol actually interacts stronger, by 10 kJ mol⁻¹, with the surface than the primary alcohol, see E_{int} in Figure 8.2.

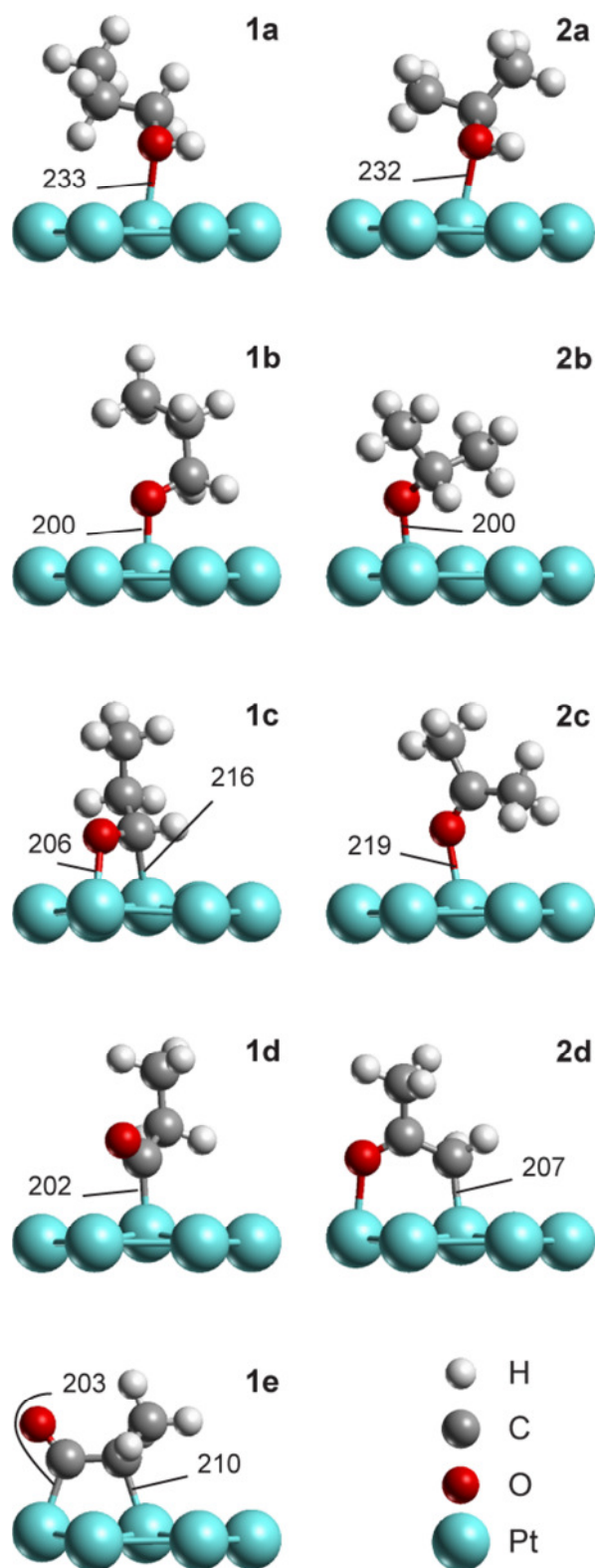


Figure 8.1 Optimized structures of 1- and 2- propanol and their dehydrogenation products on Pt(111): 1a – 1-propanol, 1b – 1-propoxy, 1c – propanal, 1d – propionyl, 1e – methyl ketene, 2a – 2-propanol, 2b – 2-propoxy, 2c – acetone, 2d – 2-oxopropyl. Selected distances are shown in pm.

Table 8.1 Energy characteristics (kJ mol^{-1}) of the intermediates C_3OH_x ($x = 4 - 8$) on the Pt(111) at 1/9 coverage.

| Intermediates | | BE ^a | E_{int}^b | $\Delta E(\text{M})^c$ | $\Delta E(\text{C}_3\text{OH}_x)^d$ |
|----------------------|-----------|-----------------|--------------------|------------------------|-------------------------------------|
| Alcohol | Primary | 32 | 38 | 4 | 2 |
| | Secondary | 28 | 48 | 17 | 3 |
| Alkoxide | Primary | 172 | 219 | 5 | 42 |
| | Secondary | 171 | 221 | 6 | 44 |
| Carbonyl | Primary | 35 | 155 | 12 | 108 |
| | Secondary | 18 | 60 | 32 | 10 |
| Acyl | Primary | 233 | 276 | 13 | 30 |
| | Secondary | 197 | 362 | 38 | 127 |
| Methyl ketene | Primary | 168 | 433 | 17 | 248 |

^a Binding energy of C_3OH_x . ^b Interaction energy of C_3OH_x . ^c Deformation energy of the Pt(111) surface. ^d Deformation energy of the adsorbate. For the definition of the energies refer to Section 5.1.

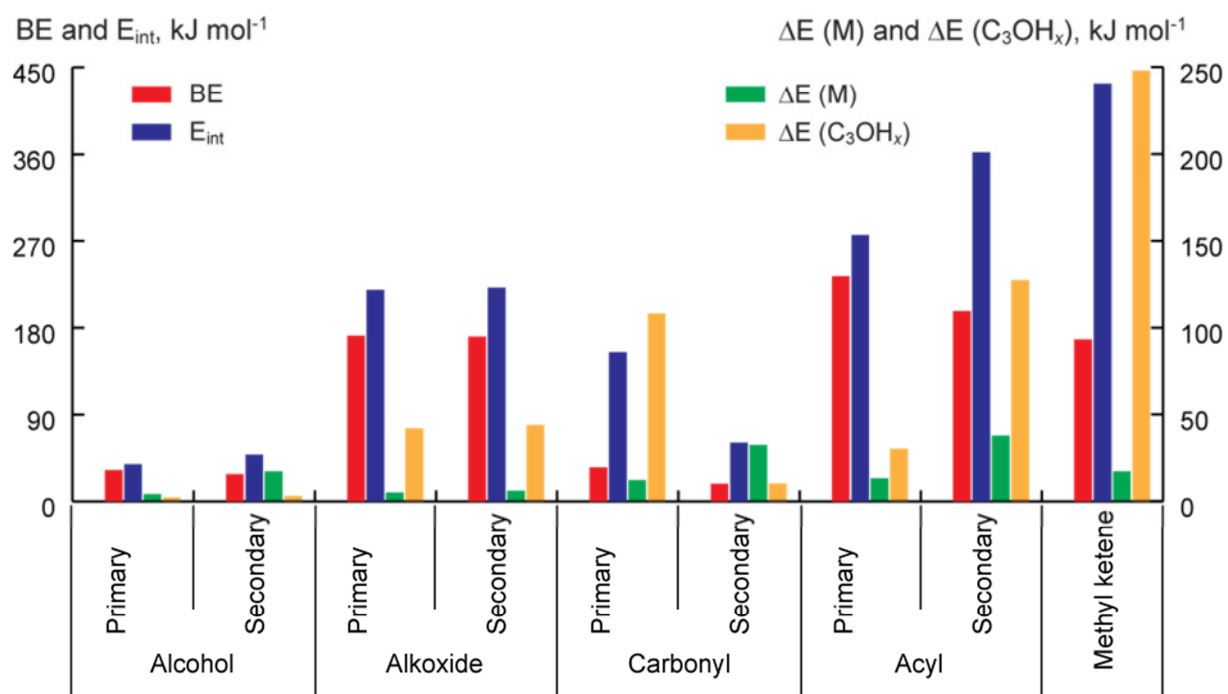


Figure 8.2 Various characteristic energies (kJ mol^{-1}) of the adsorbates on Pt(111); see Section 5.1 for the definition of the energies.

8.1.2. Alkoxides: 1- and 2-propoxy, C_3H_7O

The two molecules bind at the same site on Pt(111), atop a Pt atom. The interaction between the molecule and the surface is through the O atom, see **1b** for 1-propoxy and **2b** for 2-propoxy in Figure 8.1. The O–Pt distance is 200 pm in both cases. The C–O bond distances in the two molecules have elongated by 5 pm upon adsorption. Another notable change from the structure in the gaseous phase 1-propoxy is the dihedral angle C-C-C-O; while the C-C-C-O framework is planar in the gas phase, the dihedral angle changes to 60° when the molecule is adsorbed. The binding energies are almost the same, 172 kJ mol⁻¹ and 171 kJ mol⁻¹ for 1- and 2-propoxy, respectively. The deformation energies of the surface and the structures are also the same, Table 8.1. Thus, both species interact similarly with the metal surface.

8.1.3. Carbonyls: propanal and acetone, C_3H_6O

The adsorption of propanal and acetone can occur in two modes, especially on Group VIII metals: via only the O atom atop a metal atom, $\eta^1(O)$, or via C and O over a bridge site, $\eta^2(C,O)$.¹⁸⁰ Hence, both modes were inspected to obtain the lowest energy mode for both molecules. The most stable modes depicted in Figure 8.1 as **1c** and **2c** show that propanal prefers the η^2 mode whereas acetone prefers η^1 mode. The η^1 adsorbed mode of propanal and the η^2 adsorbed mode of acetone are given in Figure 8.3; both of these structures are each 14 kJ mol⁻¹ less stable than the corresponding favored adsorption modes. Note also the similar lengths of the bonds to the surface in η^1 and η^2 modes, irrespective of the molecule. Earlier works on acetone have also proposed the η^1 mode, both experimentally¹⁸³⁻¹⁸⁵ and theoretically.^{182,186-188} Although Vannice et al.¹⁸⁴ has advocated an η^2 mode to be the most stable adsorption mode, Jeffery et al.¹⁸⁶ pointed out, by calculating the vibrational spectra, that the η^2 species observed cannot be the ketone species and should be assigned to a different species that might have formed through the decomposition of acetone; the vibrational spectra calculated in this thesis also support their findings, see Table 8.2. Alcalá et al.¹⁸² employed the $\eta^1(O)$ adsorbed mode of propanal in their hydrogenation studies, claiming it adsorbs 11 kJ mol⁻¹ more strongly, while Loffreda et al.¹⁸⁹ employed the $\eta^2(C,O)$ mode when studying the hydrogenation of acrolein. The C–O bond of acetone (**2c**) is ~10 pm shorter than the one in propanal (**1c**), 135 pm (η^2 -acetone 137 pm), but almost the same as in η^1 -propanal, 124 pm.

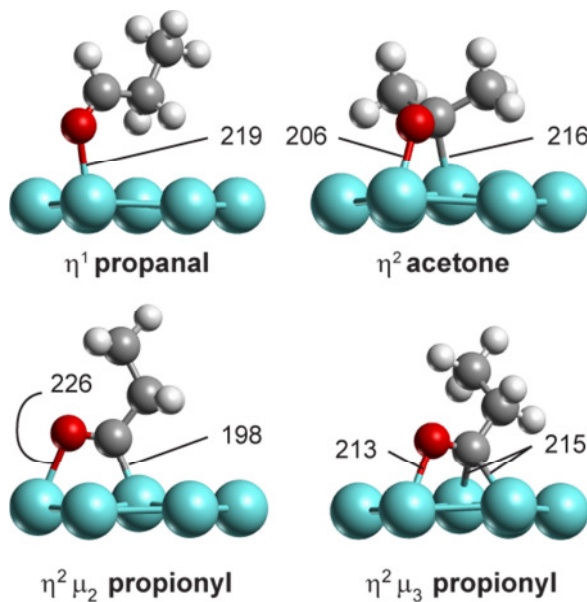


Figure 8.3 Optimized structures of adsorption complexes for alcohol dehydrogenation. The adsorption modes of carbonyls were suggested in Ref. 180, of propionyl in Ref. 190

Table 8.2 Comparison of vibrational frequency (cm^{-1}) assignments of the calculated and experimental data.

| | η^1 -acetone | η^2 -acetone | 2-oxopropyl | Mode 1 ^a | Mode 2 ^a |
|-----------------------|-------------------|-------------------|-------------|---------------------|---------------------------|
| $\nu(\text{CO})$ | 1598 | 1161 | 1544 | 1638 | 1610 1530-1585 1511 |
| $\nu_a(\text{MeCMe})$ | 1220 | 1138 | 1238 | 1238 | 1240 |
| $\nu_s(\text{MeCMe})$ | 804 | 773 | | | |

^a Values from Ref. 184. Mode 1 and Mode 2 refer to species η^1 -acetone and η^2 -acetone, respectively, as assigned in Ref. 184.

The binding energy of propanal on the surface is almost twice as large as that of acetone, however both molecules are only weakly bound on the surface, 35 kJ mol^{-1} and 18 kJ mol^{-1} , respectively. The binding energy of acetone (**2c**) presented here is very close to the value reported in a periodic DFT study,¹⁸² 19 kJ mol^{-1} , but much lower than results of another study employing periodic DFT calculations,¹⁸⁶ 40 kJ mol^{-1} , or 48 kJ mol^{-1} and 49 kJ mol^{-1} reported from temperature programmed desorption (TPD).^{183,184} In Ref. 182 the surface was modeled by a 2×2 surface unit cell of a two-layer slab with atoms at fixed geometry, calculated by ultrasoft pseudopotentials with plane waves at a kinetic energy cutoff of 340 eV

using the PW91 functional. Ref. 186 employed a 3×3 surface unit cell of a three-layer slab model with the positions of the surface atoms optimized, calculated with the PAW method and a plane wave cutoff of 400 eV, also with the PW91 functional. The adsorption energy can be decomposed into a deformation part of the substrate and an interaction energy E_{int} with the surface (cf. Section 5.1). Inspection of the interaction energies E_{int} of the both structures in Table 8.1 reveals that the difference between the primary and the secondary carbonyls, 95 kJ mol⁻¹, is much higher than the differences of the interaction energies between primary and secondary alcohols and alkoxides, 10 kJ mol⁻¹ and 2 kJ mol⁻¹, respectively. This is due to the differences in the deformation energies. The corresponding deformation energy of propanal, 108 kJ mol⁻¹, is much larger than the deformation energy of acetone, 10 kJ mol⁻¹. However in the case of acetone the surface is deformed 20 kJ mol⁻¹ more than in the case of propanal. The difference in the deformation energies can easily be explained by referring to the changes in the structures upon adsorption; propanal adsorbed in η^2 mode undergoes several structural changes from the gas phase molecule whereas the changes are minor for acetone adsorbed in η^1 mode.

8.1.4. Acyls: propionyl and 2-oxopropyl, C₃H₅O

Propionyl adsorbs through the carbon atom in $\eta^1(\text{C})$ or $\eta^2(\text{C},\text{O})$ fashion, hence also in two modes as just discussed for the carbonyls. The difference between the η^1 mode represented as (**1d**) in Figure 8.1 and the $\eta^2\mu_2$ mode shown in Figure 8.3 is only 1 kJ mol⁻¹. The $\eta^1(\text{C})$ mode produced via dehydrogenation of propanal (**1c**), as will be explained in Section 8.2.3, is taken to calculate subsequent steps. As the C atom has only one contact to the surface and is free of attached hydrogen atoms, the C–Pt distance is very short, 202 pm. The C–O bond has lost the partial triple bond character which it has in the gas-phase and represents a double bond when adsorbed with a bond length of 121 pm, whereas the C–C bond length is the same as calculated for the acyl in the gas phase, 152 pm. The adsorption energy, BE = 233 kJ mol⁻¹, of this radical is very large, the strongest of all the dehydrogenation products investigated, see Table 8.1. Lu et al.¹⁹⁰ determined the adsorption of propionyl on Pd(111) to occur at a threefold site in a $\eta^2\mu_3(\text{C},\text{O})$ mode where the C atom is bound to two Pd atoms of the surface, to be 17 kJ mol⁻¹ more stable than the atop adsorption mode. On Pt(111) surface, however, the $\eta^2\mu_3(\text{C},\text{O})$ mode located at an hcp-threefold site as shown in Figure 8.3 is calculated to be 17 kJ mol⁻¹ less stable.

The most stable adsorption mode for 2-oxopropyl was determined to be $\eta^2(\text{C},\text{O})$; see structure **2d** in Figure 8.1. The bonds of the centers C and O of this dehydrogenation product

of acetone to the surface are 207 and 216 pm, respectively. The C–CH₂ bond is elongated by 4 pm from the molecule in the gas phase, whereas C–CH₃ bond shrunk by 2 pm. With a BE of 197 kJ mol⁻¹, this radical species adsorbs strongest among the dehydrogenation products of 2-propanol.

8.1.5. *Methyl ketene, C₃H₄O*

The dehydrogenation product of propionyl (**1d**), methyl ketene, (**1e**), adsorbs on the surface in an $\eta^1\eta^1(\text{C,C})$ mode. The carbonyl C atom binds to a Pt center at a distance of 203 pm and the ethylidene carbon bond length to the surface is 210 pm. The C–C bond has elongated by 20 pm from its value in the gas phase and reached 151 pm in the adsorption complex. The linear O–C–C angle for the molecule in the gas phase has also decreased to 128°; all these changes in the structure result in a deformation energy of the molecule of 247 kJ mol⁻¹ (Table 8.1). The interaction with the surface, the strongest among all structures inspected with a value of 433 kJ mol⁻¹, is not reflected in the BE due to this high deformation energy; also see Figure 8.2. Lu et al.¹⁹⁰ calculated methyl ketene on a Pd(111) surface and determined the same mode as obtained here, but with a binding energy that is by ~50 kJ mol⁻¹ smaller.

8.2. Reactions

In this section the four consecutive dehydrogenation steps, starting from 1-propanol (**1a**), and the three consecutive dehydrogenations steps, starting from 2-propanol (**2a**), will be described. The conversion of species derived from 2-propanol (**2a**) was not continued one step further as in the case of 1-propanol (**1a**) in view of the higher barrier of the third dehydrogenation step compared to the binding strength of the reactant acetone (**2c**) on the Pt(111) surface; the third reaction goes over a very high barrier whereas the binding strength of the reactant acetone (**2c**) is low; hence this pathway has a low probability for further conversion. The reactions of the alcohols will be described in pairs; each consecutive conversion is discussed simultaneously for 1- and 2-propanol. In this way the similarities and the differences of the initial states, transition states and the final states will be given in one section. The barrier heights and the reaction energies will be also simultaneously compared. In Section 8.1 the adsorption modes of the initial states are presented in Figure 8.1 with the corresponding BE values in Table 8.1. Figure 8.4 illustrates the calculated transition states side by side, in the same fashion as it is done for the initial states in Figure 8.1. The final state structures are not shown this time, different from the first part of the thesis as the first part dealt with a comparison of various metals. In the present system, the hydrogen in the final

state is adsorbed at a nearby site, coadsorbed with the dehydrogenated species. Hydrogen is assumed to migrate subsequently to a distant location before the next dehydrogenation step. The total energy change in the dehydrogenation reactions of 1- and 2-propanol is shown in Figure 8.5.

8.2.1. Alcohol dehydrogenation, TS_{nab}.

As described in Section 8.1.1, the most stable mode of alcohol adsorbed on Pt surfaces is through the oxygen atom, mediated via the oxygen lone pair. In the literature it is well documented that experimentally the hydroxyl hydrogen dissociates to form an alkoxide intermediate on Pt group metals.^{180,191-193} However, there are recent computational studies suggesting that hydroxyalkyl species are more stable than the corresponding alkoxides species.¹⁹⁴⁻¹⁹⁷ Even if this is the case, this kind of C–H bond scission would require the initial adsorption geometry of the alcohol on the surface to be bound through the α -C, which is by 10 kJ mol⁻¹ less favorable.¹⁹⁸ Hence, in this study the first dehydrogenation of alcohol is considered to happen at the hydroxyl group, producing 1- and 2-propoxide from 1- and 2-propanol, respectively.

The hydroxyl hydrogen atoms to be separated points to the surface in the initial state in both cases, see structures **1a** and **2a** in Figure 8.1. This H atom starts to interact with a neighboring Pt atom, causing the molecule to be bound to the surface almost as in a bridge site at the TS, **TS1ab** and **TS2ab** (Figure 8.4). In **TS1ab** of 1-propanol and **TS2ab** of 2-propanol the newly forming bond to the metal, between H and Pt, is rather short, 163 pm. The O–H bonds, which were 98 pm in 1- and 2-propanol in the adsorption geometries, elongate to 166–167 pm in the TS structures. The O–Pt distances are again very close to each other for the two molecules, contracting to 206–207 pm at the TS. All the geometrical parameters are very close to those calculated previously in the TS structures of 1- and 2-propoxide hydrogenation to corresponding alcohols.¹⁸²

The reaction of 1- and 2-propanol dehydrogenation to corresponding alkoxides is endothermic, calculated at 45 kJ mol⁻¹ for the primary and at 48 kJ mol⁻¹ for the secondary alcohol, see Table 8.3. According to Hammond's postulate the transition state geometry will resemble the final state when the reaction is endothermic. This is satisfied here as the O–H bond is strongly elongated and the newly formed H–Pt bond has already shortened to 163 pm. The barriers of both reactions are also similar to each other, 62 kJ mol⁻¹ and 68 kJ mol⁻¹ for 1- and 2-propanol, respectively. Alcalá et al.¹⁸² calculated the same reaction in a DFT study, by a 2 × 2 surface unit cell, modeled with a two-layer slab, kept at a fixed geometry, employing

ultrasoft-pseudopotentials and PW91 as the functional, at an energy cutoff of 340 eV. The corresponding dehydrogenation energies they obtained were 58 kJ mol⁻¹ for 1-propanol over a 77 kJ mol⁻¹ barrier and 53 kJ mol⁻¹ for 2-propanol over a 71 kJ mol⁻¹ barrier. The values for 2-propanol are close to the values obtained in this study whereas those for 1-propanol conversion are higher than the ones calculated here. These differences might be due to the simpler model employed by Alcalá et al.¹⁸² Chibani et al.¹⁹⁹ computed the same reaction for the secondary alcohol, and came up with a barrier of 90 kJ mol⁻¹ and a reaction energy of 69 kJ mol⁻¹, with the same computational parameters as in this study, apart from employing a surface modeled with a four-layer slab instead of five. Both values obtained by Chibani et al. are higher compared to the ones calculated in this study, although the TS structures calculated in both studies are similar, apart from their structure being closer to the surface than it is in this study. This might rationalize the lower energy presented in this thesis due to a higher stabilization of the complex. In the study by Chibani et al. ethanol instead of 1-propanol was chosen to represent the primary alcohol. The energies they calculated, 65 kJ mol⁻¹ and 85 kJ mol⁻¹ for the reaction energy and the barrier, respectively, are again higher than those mentioned here for 1-propanol. Experimentally, the barrier of 2-propanol dehydrogenation was reported to be 38–48 kJ mol⁻¹ when catalyzed by Pt powder of ultra high purity and 28–30 kJ mol⁻¹ when catalyzed by Pt supported on activated carbon.¹⁹³

A recent study by Michel et al. investigated alcohol dehydrogenation on Rh(111) surface.²⁰⁰ They have observed that hydrogen bonding between a coadsorbed ethanol and water and in a glycerol molecule itself decreases the dehydrogenation barrier at the OH group. Hence, in that case also the transition states might go over lower barriers with the presence of hydrogen bonding when there is a hydrogen network employed in the model. Zope et al. showed that the presence of a hydroxyl group on the surface decreases the reaction energy of ethanol dehydrogenation on Pt(111) from 98 to -5 kJ mol⁻¹ while decreasing the barrier from 116 kJ mol⁻¹ to 18 kJ mol⁻¹, producing water together with the adsorbed alkoxide.²⁰¹

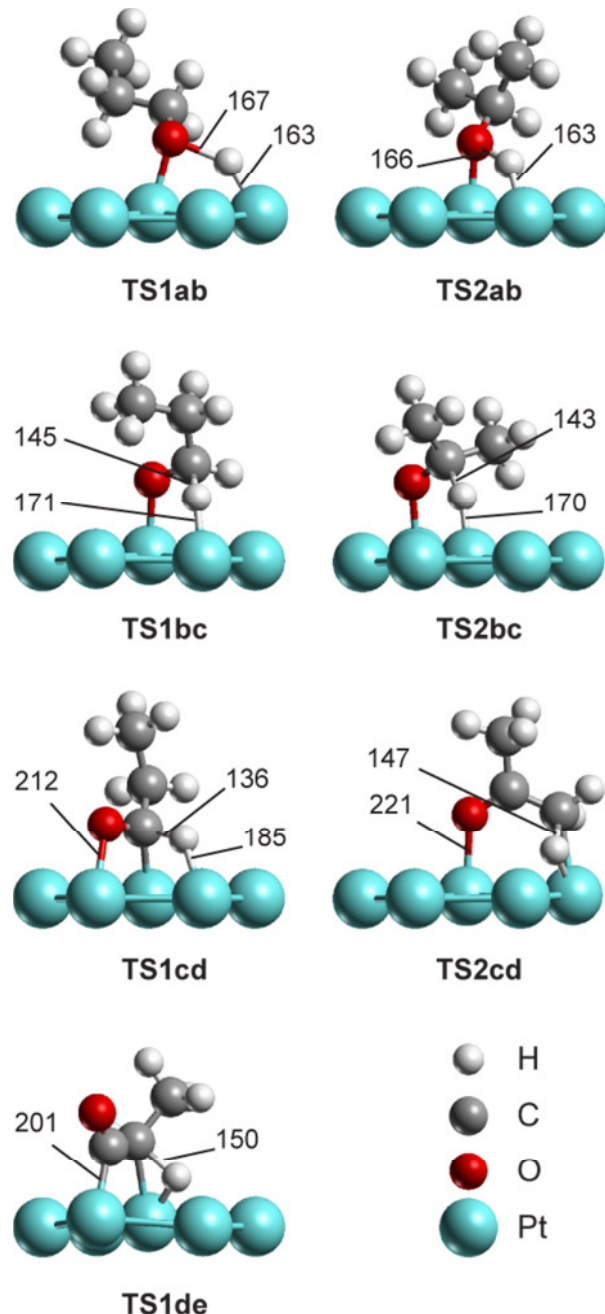


Figure 8.4 Transition state structures of the consecutive dehydrogenation reactions of 1- and 2- propanol on Pt(111). Structures are named **TS_nx_y** ($n = 1 - 2$, $x = a - d$, $y = b - e$), a dehydrogenation of **nx** structure to **ny** structure, as depicted in Figure 8.1. Selected distances are shown in pm. Atom coding is also supplied.

Table 8.3 Energies of the reactions (kJ mol^{-1}) involved in the dehydrogenations of primary and secondary alcohols on Pt(111). E_r and E_r^{inf} are reaction energies at close proximity and infinite distance, respectively, and E_a is the activation barrier.

| | | E_r^a | $E_r^{\text{inf},b}$ | E_a^c |
|-----------------|-----------|---------|----------------------|---------|
| Alcohol | Primary | 45 | 45 | 62 |
| | Secondary | 48 | 45 | 68 |
| Alkoxide | Primary | -42 | -43 | 12 |
| | Secondary | -46 | -48 | 7 |
| Carbonyl | Primary | -74 | -79 | 11 |
| | Secondary | -18 | -30 | 70 |
| Acy1 | Primary | 4 | -6 | 91 |

^a Reaction energy at close proximity. ^b Reaction energy at infinite distance. ^c Activation energy

8.2.2. Alkoxide dehydrogenation, TS_{nbc}

The second step in the typical alcohol decomposition path on Pt-group metals is H abstraction from C₁ to form the corresponding carbonyl compounds.^{180,192} Hence in this step the H atom geminal to the O center will be eliminated to form propanal (**1c**) from 1-propoxide (**1b**) and acetone (**2c**) from 2-propoxide (**2b**).

The geometries of TS structures **TS1bc** and **TS2bc** of the dehydrogenation are very similar, as shown in Figure 8.4. The H atom that is dissociating interacts with a nearby Pt atom, the C–H bond is elongated by 30–32 pm at the TS while the H–Pt distance remains long, 170–171 pm. The O–Pt bond lengths for both cases are also similar, 208–209 pm. Again, the calculated values are very close to those calculated previously by Alcalá et al.¹⁸² apart from the O–Pt distances. The values determined in this study are by 9 pm shorter than previously reported, as the intermediate propoxy species were also calculated to bond through longer O–Pt bonds in this study.

The reactions for the alkoxides dehydrogenation step are exothermic, calculated at -42 kJ mol^{-1} for the primary and at -46 kJ mol^{-1} for the secondary alkoxides as shown in Table 8.3. Also the barriers are very low in both cases, only 12 kJ mol^{-1} and 7 kJ mol^{-1} , respectively. In this case, the barrier calculated for the secondary alcohol matches the value obtained by Besson et al.;¹⁹⁹ the reaction energy they obtained is by ~15 kJ mol^{-1} more exothermic. The extremely low values of barriers point to a very fast dehydrogenation of the propoxy species

once they are formed; hence the detection on the surface in experiments should be very difficult.

8.2.3. Carbonyl dehydrogenation, TS_ncd.

The two previous dehydrogenation steps were very similar for the species both

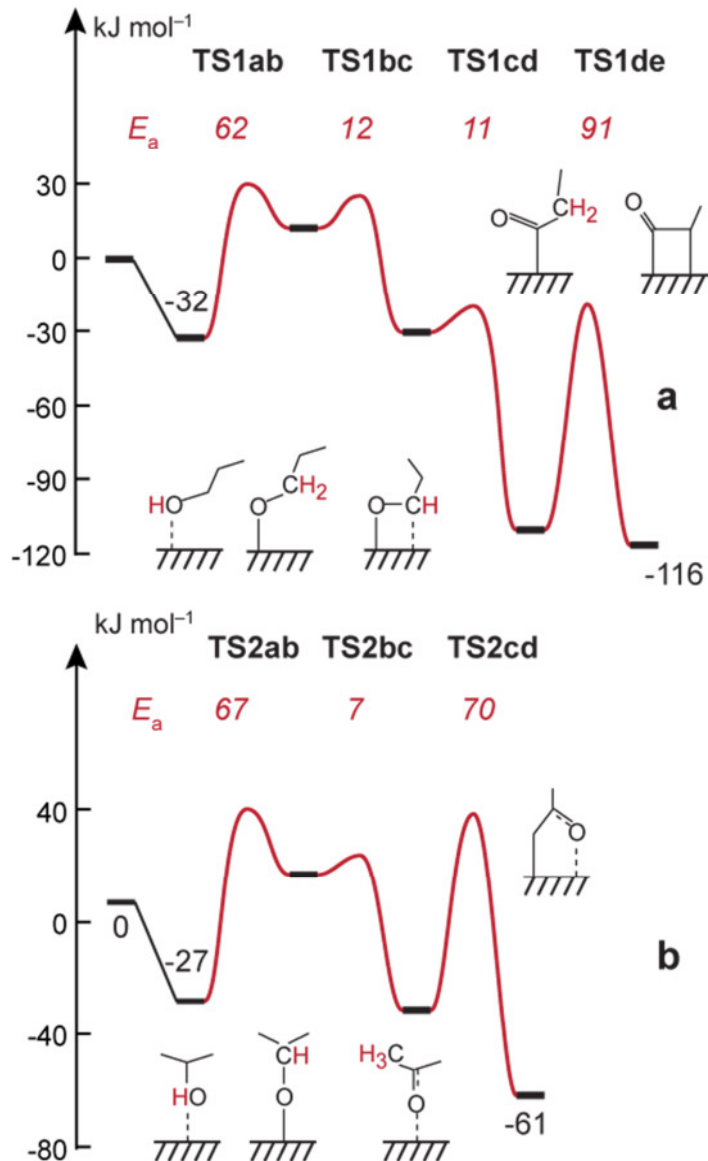


Figure 8.5 Calculated energy profiles of alcohol dehydrogenation on Pt(111) at coverage 1/9: comparison of analogous dehydrogenation steps for (a) 1-propanol and (b) 2-propanol. Energies are relative to a system where the corresponding alcohol molecule is in the gas phase and the surface is clean. The reaction energies are represented with products at infinite separation. Arcs represent reaction barriers of the various dehydrogenation steps; the corresponding activation energies are listed as E_a values (in italics). All energies in kJ mol^{-1} .

geometrically and energetically. For these steps, the reactant adsorption geometries were the same, but, as discussed in Section 8.1.3, the most stable adsorption modes of the carbonyls, propanal and acetone, are not the same. Hence one anticipates that the TS structures of the subsequent dehydrogenation reactions will also be different. Another difference is the greater strength of the C–H bond in acetone than in propanal; calculations on species in the gas phase reveal a difference of 30 kJ mol⁻¹.

In the dehydrogenation of the η^2 mode of propanal (**1c**), the H atom of the CH group bound to the surface starts to interact with a close by Pt atom of the surface. At a very small elongation of the C–H bond, the transition state is reached. At the TS **TS1cd**, the C–H bond length is only 136 pm, and the new H–Pt bond is accordingly 185 pm long, hence very close to the initial state. As the resemblance of the TS to the IS suggests exothermicity, the reaction releases 74 kJ mol⁻¹. The barrier that accompanies this conversion is low, only 11 kJ mol⁻¹ (Figure 8.5).

The η^1 mode of acetone causes the CH₃ groups to be pointing away from the surface. However as the molecule is somewhat bent, one CH₃ group is closer to the surface than the other, as structure **2c** in Figure 8.4 shows. One of the H atoms that is close to the surface starts to interact with a nearby Pt atom, but the C atom of the CH₃ group comes also close to the surface as shown in Figure 8.4 as **TS2cd**. Hence at the TS the resulting structure is already an oxametallacycle, resembling the FS. The dehydrogenation is slightly exothermic; the reaction energy is -18 kJ mol⁻¹. The corresponding barrier for the C–H bond to be broken is 70 kJ mol⁻¹, much higher than the corresponding conversion for propanal as shown in Figure 8.5. This barrier is much higher also compared to the adsorption energy of acetone on the surface, calculated at 18 kJ mol⁻¹ (Table 8.1), which raises the propensity for desorption rather than for the decomposition of the ketone **2c**. Despite this lower propensity to dehydrogenate, the vibrational spectra of the η^2 -species that Vannice et al.¹⁸⁴ observed when increasing the temperature during acetone adsorption on Pt(111) and described as a strongly bound $\eta^2(\text{C},\text{O})$ -acetone resembles more the vibrational spectra of η^2 adsorbed 2-oxopropyl (**2d**). The vibrational spectra determined in this work and in the experiment are listed in Table 8.2. The C–O bond stretching frequency, $\nu(\text{CO})$, of η^1 -acetone calculated in this work matches the value of mode 1 in Ref. 184, but the value of η^2 -acetone is very different from that of mode 2. Also the asymmetrical stretch of the methyl groups, $\nu_a(\text{MeCMe})$, of η^2 -acetone is not similar to that of mode 2 determined in the experiment. In both cases the frequencies match better

those of 2-oxopropyl. This might be an indication that deprotonation of acetone on clean Pt(111) surface can take place, as has been pointed out by Jeffery et al.¹⁸⁶

Although deprotonation is possible on a clean surface, there is a difference in the reaction behavior for the two carbonyls derived from 1- and 2-propanol due to their most stable adsorption mode on the surface. This difference matches the earlier observation that $\eta^1(\text{O})$ configuration of acetone desorbs in the presence of other intermediates rather than decomposes further, while the $\eta^2(\text{C},\text{O})$ configuration undergoes C–H bond scission at the carbonyl position.^{180,192,199} Rioux and Vannice¹⁹³ reported that 2-propanol converts to acetone with 100% selectivity on a Pt catalyst on acidic group-free supports. Experiments with 2-propanol on Pt/Al₂O₃ in the gas phase also found acetone forming below 473 K while propane, through dehydration on the support and hydrogenation on the metal, becomes the major product at higher temperatures.¹⁷² The reactivity of 1- and 2-propanol was also compared on Pt/ γ -Al₂O₃ in the presence of water²⁵ and acetone was observed as the main product from 2-propanol while C–C bond scission takes place in the 1-propanol conversion, observed as ethane and CO₂. However, as the experiments were carried out in an aqueous medium, it is important to inspect the behavior of these two intermediates when water is around. With a simplified model, where several explicit water molecules represented the aqueous phase, the adsorption and desorption behavior of two carbonyls is investigated in Section 8.3.

8.2.4. Acyl dehydrogenation, TSnde.

As the 2-propanol (**2a**) conversion ends with dehydrogenation to acetone (**2c**), in this step only the dehydrogenation of the propionyl (**1d**) species, derived from 1-propanol (**1a**), is considered.

In this step many structural changes occur until the species is converted to its most stable intermediate in its $\eta^2(\text{C},\text{C})$ adsorption mode on the surface. The α -H atom dissociates in this step from the carbon center. As in the case of acetone dehydrogenation, the α -C center also interacts with the surface and binds to the same Pt atom that the α -H atom is connected to. At the **TS1de** in Figure 8.4, the molecule is in almost the same conformation as the final state of methyl ketene (**1e** in Figure 8.1). The C–H distance elongates to 150 pm and the H is almost at a Pt–Pt bridge position with bond lengths of 169 pm and 214 pm at the **TS1de**. The newly formed C–Pt bond is 232 pm long; in the initial state **1d** this C atom was 357 pm separated from the Pt atom of the surface.

The reaction is endothermic by only 4 kJ mol⁻¹ although the geometry of the transition state shows a late character that would suggest a higher endothermicity. However the barrier that the reaction has to overcome is very high, 91 kJ mol⁻¹ (Figure 8.5a), in comparison with other dehydrogenation reactions that 1-propanol undergoes. This high barrier hinders a fast conversion of propionyl (**1d**) to methyl ketene (**1e**). However, in contrast to acetone (**2c**), propionyl is not expected to desorb from the surface due to strong adsorption on the surface, BE = 233 kJ mol⁻¹ (Table 8.1). The possibility of propionyl to undergo C-C bond breaking in order to eliminate CO deserves some interest as that route has been proposed on many surfaces.^{180,192} This particular reaction network comprising C-C bond breaking reactions also at surface defects, represented as steps, is discussed in Chapter 9.

8.3. Aqueous medium modeling

The experiments conducted on 1- and 2-propanol that suggested different routes for the primary and secondary alcohol were done in the presence of water as solvent. Hence it is important to consider how the presence of the water affects the adsorption and the reaction of the intermediates. As modeling every single step of this reaction chain for both of the molecules is a very demanding task, only those intermediates are considered where the difference in behavior arises. Hence the two intermediates, which are the reactants of the third decisive step, are inspected in aqueous medium. Presently the studies with aqueous models are limited to systems with small adsorbates and a few reactions. Researchers have come up with several ways to deal with the problem. One strategy is to fill up the space between repeated slabs with water molecules of a certain density, employing tri-dimensional ice layers.²⁰¹⁻²⁰³ Another approach is more exclusive to clusters, where the solvent water is represented by a continuum with an appropriate dielectric constant as Goddard et al. have employed in their treatment of water formation.²⁰⁴ Very recently, Heyden et al.²⁰⁵ presented their implicit solvation model, where they include the solvent effect by calculating cluster models in an implicit continuum and use the free energy differences between those and clusters without an implicit solvent description as a localized perturbation to the results of periodic-slab calculations.

In this study, a simpler approach has been applied as the concern is focused on a desorption reaction, which is supposed to occur in very close proximity to the surface. Hence only one layer of water consisting of eight water molecules per unit cell is taken to represent the reaction in question as has been detailed in Chapter 2 and depicted in Figure 2.1. Propanal and acetone were placed selectively in this water layer coated Pt(111) surface to model two

situations: (i) close to the surface, below the water layer to represent the adsorbed state, and (ii) away from the surface, on the water layer to represent the desorbed mode.

8.3.1. *Propanal, 1c*

Propanal adsorption on the close packed (111) surface of Pt in the presence of water molecules is shown in the structure **1c-ads** of Figure 8.6. This complex resembles closely the propanal-metal complex in the gas phase, used in the calculations which have been described in Section 8.1.3, and represented as **1c** in Figure 8.1. The hydrogen bonding network due to the water molecules on the surface also extends to the O atom which is bonded to the surface with an O–H distance of 160 pm. The C–Pt distance, 217 pm, and the O–Pt distance, 209 pm, are 1 pm and 3 pm, respectively, longer than the corresponding values for the complex at the metal–vacuum interface. The C–O distance is by 5 pm longer, 140 pm, than when the adsorbate is calculated without water molecules. This latter result is probably due to bond competition by the hydrogen bond.

When propanal is placed above the water layer with its oxygen end pointing to the water molecules as shown as **1c-des** in Figure 8.6, the structure is stabilized through two weak bonds with O–H distances of 203 pm and 220 pm in the hydrogen bonding network of water molecules. The geometrical properties of propanal, e.g., bond distances and angles, are close to the values of the propanal molecule in the gas phase. Compared to the propanal placed closer to the surface, **1c-ads**, this latter structure, **1c-des**, is 59 kJ mol⁻¹ more stable.

8.3.2. *Acetone, 2c*

Acetone placed at the close-packed (111) surface to represent the adsorbed mode optimizes to the “solvated” structure **2c-ads** in Figure 8.6. Although the adsorbate itself also resembles its adsorbed form on the surface at the metal–vacuum interface, acetone does not chemisorb anymore on the surface; it is ~400 pm away from the surface. As in the case of the complex at the metal–vacuum interface, where it was adsorbed weakly with a BE of 18 kJ mol⁻¹, the bond lengths of the angles of the molecule are similar to its molecular gas phase values. Acetone is included in the hydrogen bonding network of the water molecules through an O–H bond of 168 pm.

When placing the molecule above the water layer, it was also configured with its O end positioned towards the water layer. As a result of that, acetone is stabilized above the water layer by forming two hydrogen bonds with distances of 164 and 206 pm. Again there are no significant changes in the structure of the acetone molecule when compared to the free

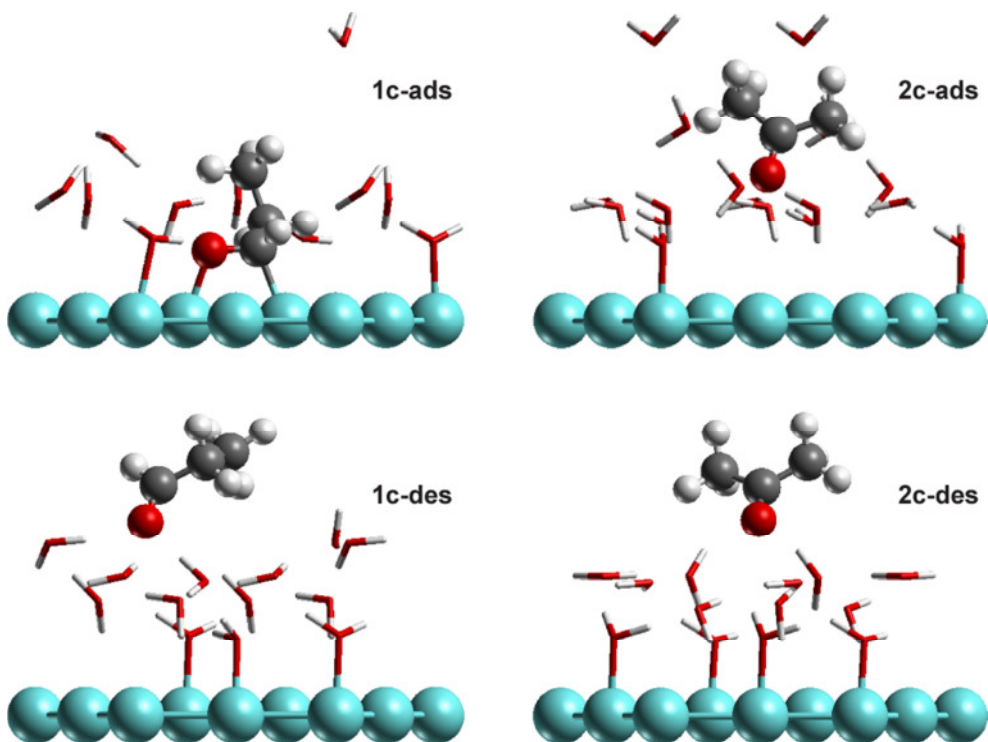


Figure 8.6 Propanal **1c** and acetone **2c** optimized with an approximate representation of the aqueous medium (see Figure 8.1 for the adsorption modes without the aqueous medium). Aqua ligands from more than one unit cell are shown.

molecule. Placed above the water layer, this structure, **2c-des**, is 47 kJ mol^{-1} more stable than the one closer to the surface.

8.3.3. Desorption of propanal and acetone in aqueous medium

In the last two subsections the optimized geometries of the two carbonyls in the presence of a water layer above and below it were described. The significant differences between these optimized complexes occur in the case of acetone close to the surface layer, approximating the “adsorbed” mode. The 400 pm distance of the molecule to the surface indicates an energetically downhill transfer of the molecule into the aqueous phase. In fact, when it finally arrives at the “desorbed” mode, approximated by placing the molecule above the water layer, it still gains 47 kJ mol^{-1} . Through this transfer, the structure of the molecule hardly changes; the relaxation of the structure at the “adsorbed” mode to the structure at the “desorbed” mode releases only 2 kJ mol^{-1} . Propanal, however, presents a totally different case. As explained in Section 8.3.1, the geometries of the complex closer to the surface and that lying above the water layer are remarkably different. When propanal is above the water layer it is still more stable than the “adsorbed” mode as in the case of acetone, but this time the stable minimum of an adsorbed mode of propanal on the surface points out to a transfer

into the water layer that is energetically not continuously downhill, indicating the presence of a barrier to desorption. The relaxation in the gas phase of the adsorbed structure of propanal to the geometry of the desorbed structure of propanal is 160 kJ mol^{-1} exothermic. Thus, assuming the propanal leaves the surface with its structure fixed as depicted in **1c-ads** mode, its shape will be strongly unfavorable for the situation in solution.

To see the differences in energies in both systems in detail, energies of the systems were calculated for structures where the solute was placed at various heights above the surface. As there are two different modes of each molecule, one being the adsorbed (“inner sphere”) and the other above the water (“outer sphere”), both those geometries of propanal were calculated at various heights above the surface. One can imagine the situation as the adsorbate moving upwards from the surface and the desorbed solute moving downwards into the solvent while the energy of the complex at several heights at fixed geometry is calculated. The energy differences resulting from such operations are given in Figure 8.7. The energy curves for moving the structures upwards and downwards intersect at energies $\sim 190 \text{ kJ mol}^{-1}$ for **1c** and 14 kJ mol^{-1} for **2c** above the energies of the adsorbed complexes. Relaxation of the propanal would decrease this energy at most by $\sim 160 \text{ kJ mol}^{-1}$ while for acetone this number is $\sim 2 \text{ kJ mol}^{-1}$. This result indicates that there exists an activation barrier to desorption in the case of propanal of $\sim 30 \text{ kJ mol}^{-1}$ whereas the barrier for propanal dehydrogenation is calculated at 11 kJ mol^{-1} (Figure 8.5a).

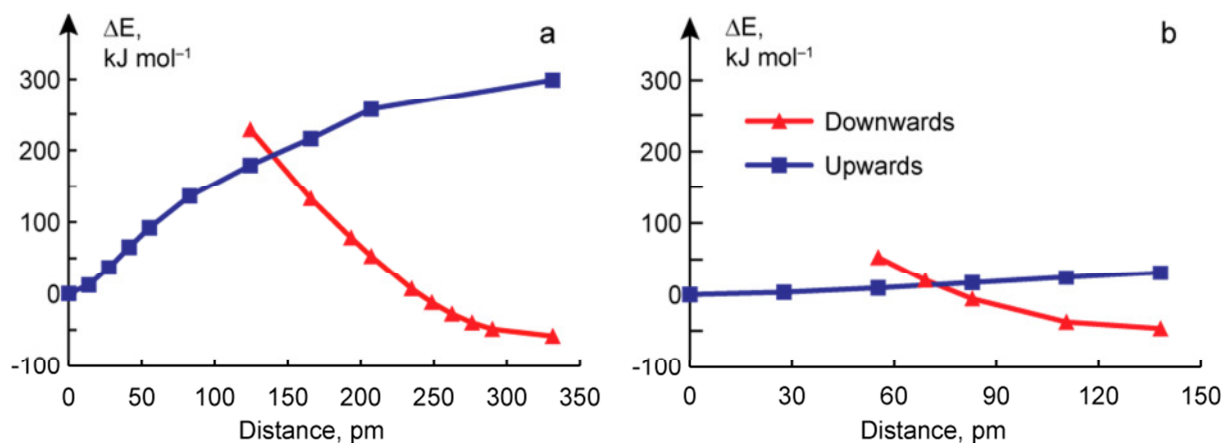


Figure 8.7 Single-point energies of the solute in a water layer at various distances above the surface, with its structure fixed at the adsorption complex (“inner sphere”, moved upwards) and the geometry above the solvent (“outer sphere”, moved downwards): (a) propanal, (b) acetone. Energies (kJ mol⁻¹) and distances (pm) are referenced to the adsorption complexes.

Based on this indication, the transition state of propanal desorbing was calculated for a simple solvation model. The resulting structure is depicted in Figure 8.8. The activation barrier associated with this structure is 28 kJ mol^{-1} . Hence the simple models support acetone desorption but the presence of a barrier in the case of propanal suggests the possibility of further conversions on the surface. This result also confirms the observation in the experiments,²⁵ which detect acetone in the product mixture of 2-propanol (Section 8.2.3).

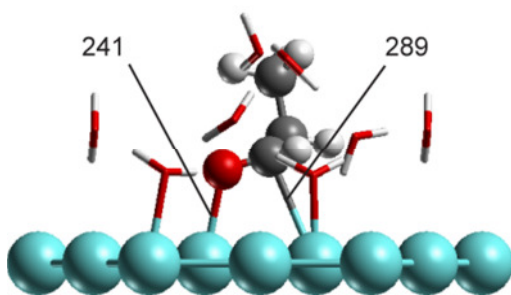


Figure 8.8 Transition state of propanal leaving the Pt(111) surface. Selected distances in pm.

8.4. Conclusions on the dehydrogenation behavior of 1- and 2-propanol

Based on the experimental observation that primary and secondary C₃ alcohols behave differently under the same experimental conditions,^{25,172} the initial dehydrogenation pathways of the two alcohols were investigated via density functional theory based calculations. This dehydrogenation pathway is of special importance as for the 2-propanol case it is the pathway that forms the main product, acetone, and for 1-propanol case, it is believed to initiate the C–C or C–O bond cleavage reactions, as these reactions, especially C–C bond breaking, are found to occur easily on more dehydrogenated groups.^{22,206}

In the dehydrogenation network of 1- and 2-propanol, the first two steps are very similar, both energetically and structurally. The structures produced as a result of the first two conversions adsorb in a different way on the surface, resulting in differences in the probable conversions of both carbonyls. The activation barrier of propanal (**1d**) conversion derived from 1-propanol (**1a**), is 17 kJ mol^{-1} whereas that of acetone (**2c**), derived from 2-propanol (**2a**) is 70 kJ mol^{-1} (Figure 8.5). The obvious competing reaction for each molecule is desorption from the surface. The adsorption of propanal on the surface is 17 kJ mol^{-1} stronger than that of acetone, see Table 8.1. Although one might argue that the difference in the adsorption energies is not too large, taking into account the overall accuracy of the model strategy, the additional difference in the conversion barriers makes desorption a more feasible

choice for acetone (**2c**) whereas propanal (**1c**) easily converts over a low barrier into propionyl (**1d**). Propionyl (**1d**) adsorbs very strongly on the surface, and the barrier to dehydrogenate this species to methyl ketene (**1e**) is even higher than that of the acetone (**2c**). However in this case as the molecule **1d** binds very strongly on the surface, the competing reaction is not the desorption of the molecule, but other decomposition reactions such as C-C bond breaking, which will be investigated in Chapter 9. The calculations including a basic model for the aqueous environment also confirm the very weak interaction of acetone (**2c**) on the surface and desorption without a barrier whereas propanal (**1c**) remains interacting with the metal surface even though there are water molecules in the environment.

The geometry of the molecules plays an important part in this discrepancy between the reaction pathways; for acetone (**2c**) to reach an adsorption mode where the H atom would be extracted more easily, it has to rearrange into a mode where, due to repulsive interaction of the methyl group with the surface, it is 14 kJ mol⁻¹ less stable. Another important difference is the strength of C–H bonds in propanal (**1c**) and acetone (**2c**). A calculation of H extraction in the gas phase shows that the C–H bond to be activated in the methyl group of acetone is 30 kJ mol⁻¹ stronger than the C–H bond of the carbonyl C atom of propanal, further suggesting an easier dehydrogenation in the case of propanal (**1c**).

9. Conversion of propionyl to CO₂ and ethane

In this chapter, I will concentrate on the further conversion of the most stable product from the dehydrogenation of 1-propanol to the products of highest selectivity, ethane and CO₂, obtained in the experiments in aqueous medium.^{25,178} Another product observed in the experiments is propionic acid. Wawrzetz et al.²⁵ report a lesser extent in their experiments on smaller particles ($d \approx 1.5$ nm) while Lobo et al.¹⁷⁸ observed a higher fraction of the products to be propionic acid on larger particles ($d \approx 3.4$ nm). Propanal was also reported in both studies. Lobo et al. mention additionally propane formation in the same amount as propanal. As the experiments are conducted in aqueous medium, the source of CO₂ formed is unclear; it might form from WGS of CO formed by decarbonylation. Lobo et al.¹⁷⁸ report a low amount of CO present on the surface as is frequently seen during carbonyl conversion on metal surfaces.^{207,208} Alternatively, oxidation of aldehyde by an oxygen containing group, here possibly OH, might produce intermediates that will form CO₂ directly via decarboxylation. These OH groups on the surface may be supplied by water dissociation. Although this process on a clean Pt(111) surface is disputed,²⁰⁹⁻²¹¹ the presence of impurities, such as adsorbed O or CO,²¹²⁻²¹⁴ facilitates the process. As Frassoldati et al.¹⁷⁹ presented in their paper on primary

alcohol oxidation in dioxane, the addition of water to the solution caused the formation of acid as a product, and the source of oxygen atom was confirmed to be coming from water rather than from the supplied O₂ gas.²¹⁵

Figure 9.1 shows the reaction network to be examined in the following. There are in total six reactions that cleave C–C bonds of intermediates reached by different dehydrogenation levels of propionyl, the most stable intermediate of 1-propanol as shown in Chapter 8. C–C bond scission reactions are considered only at the C–C bond nearest to the CO group as previous experiments on Pt²¹⁶ and Pd²¹⁷ had shown that for alcohols only these bonds are broken. Apart from the ideal close-packed (111) surface of Pt as the reference surface, a (221) surface is also employed to investigate the effects of surface defects. While the (111) facets dominate the surfaces of larger particles, smaller particles tend to be made up of stepped facets. For particles with a diameter smaller than 10 nm it was shown that the ratio of the step and kink sites increases significantly.²¹⁸ These sites are under-coordinated and exhibit a different aptitude when they interact with molecules. Surfaces that are rich in such sites, referred to as “rough surfaces”,²¹⁹ are usually more reactive. Ethylene decomposition on the stepped surface of Ni occurs at more than 100 K lower temperatures on the stepped surfaces than on the flat (111) surface,²²⁰ CO adsorbs stronger on the step sites of Pt,²²¹ NO dissociates easier on stepped Ru surfaces,²²² and the activation barrier of N₂ drops by 145 kJ mol⁻¹ on stepped Ru surfaces.²²² This effect is divided in two classes: an entirely electronic effect which is due to changing d-band center, or purely geometrical effect due to different arrangements of the surface atoms providing new adsorption configurations for the molecules.^{223,224} Recently Zhao et al.²²⁵ showed that such structural effects are notable in reducing the barriers of C–C bond breaking reactions and thus affect the product distribution of methylcyclopentane decomposition. Hence, for the conversion of propionyl the dehydrogenation and the C–C bond scission reactions on both surfaces were considered.

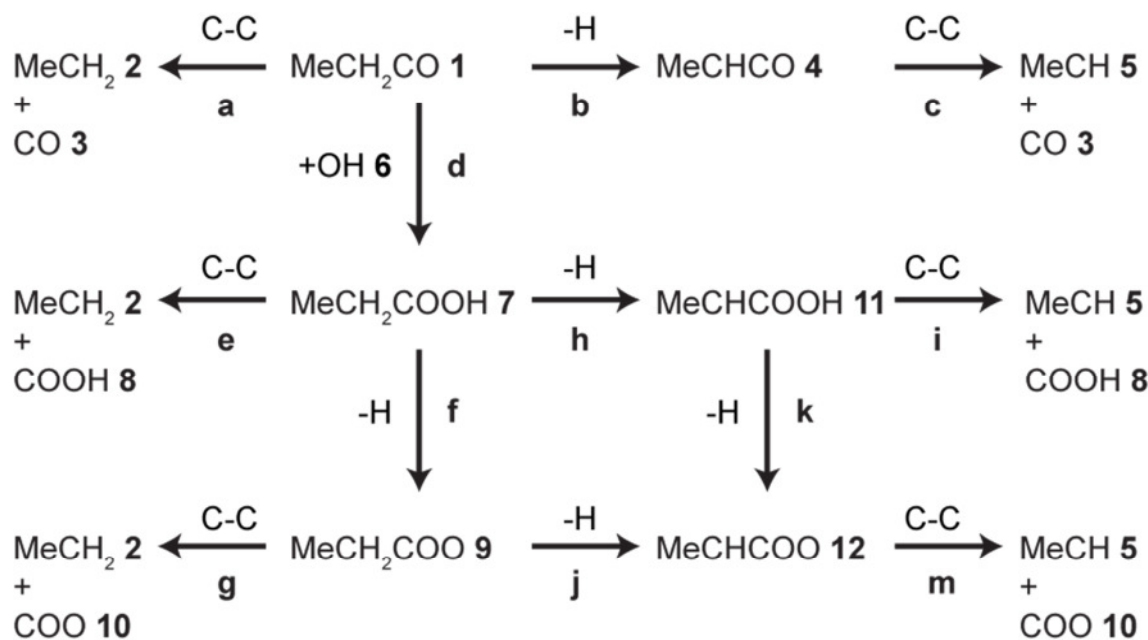


Figure 9.1 Reaction network for the conversion of propionyl to ethane and CO_2 . The C–C bond breaking reactions occur on the outermost columns. In the dehydrogenation reactions, the product H is not represented. The names of the reactions are given below each arrow in lower-case letters, molecules are numbered in parentheses. Me represents the methyl (CH_3) group.

9.1. Adsorption complexes on the flat (111) and on the stepped (221) surface

First of all, the stable adsorption geometries of the intermediates occurring throughout the network represented in Figure 9.1 are calculated on both the flat (111) and the stepped (221) surfaces. On the flat surface the most stable geometry and the site for each adsorbate are selected, while on the stepped surface those sites and geometries were preferentially probed that looked promising to remove geometrical strain for the conversions in question. The species obtained during the conversion of propionyl (MeCH₂CO 1) are: ethyl (MeCH₂ 2), carbon monoxide (CO 3), methyl ketene (MeCHCO 4), ethyldene (MeCH 5), propionic acid (MeCH₂COOH 7), carboxyl group (COOH 8), propionate (MeCH₂COO 9), carbon dioxide (CO₂ 10), 1-carboxy-ethyl (MeCHCOOH 11), 1,1-propendiolate (MeCHCOO 12) and H. Me here represents the methyl (CH_3) group. The species on the stepped surface are identified with a prime next to the number, e.g., 1' identifies propionyl (MeCH₂CO) adsorbed on a stepped surface. Figures 9.2 and 9.3 show the adsorbates on flat and stepped surfaces, respectively. Table 9.1 lists the binding energies of the intermediates along with the deformation energies

of the intermediates and the surfaces to investigate the extent of metal-adsorbate interaction, as described in Section 5.1, additionally.

9.1.1. Propionyl, MeCH_2CO 1& 1'

The adsorption mode of propionyl is the same as in Section 8.1.4 and **1d** in Figure 8.1. To facilitate the following discussion, the same structure is presented here also in Figure 9.2 labeled as **1**.

On the stepped surface propionyl is adsorbed at a terrace site to benefit C–C bond scission or dehydrogenation via introducing available adjacent sites with which the dissociating atoms can straightforwardly interact. As shown in Figure 9.3 as **1'**, the molecule is again adsorbed through the C atom in the same mode as **1**, but this time the Pt–C bond is tilted $\sim 10^\circ$ more from the terrace normal (cf. Figure 9.2), which brings the O atom 18 pm

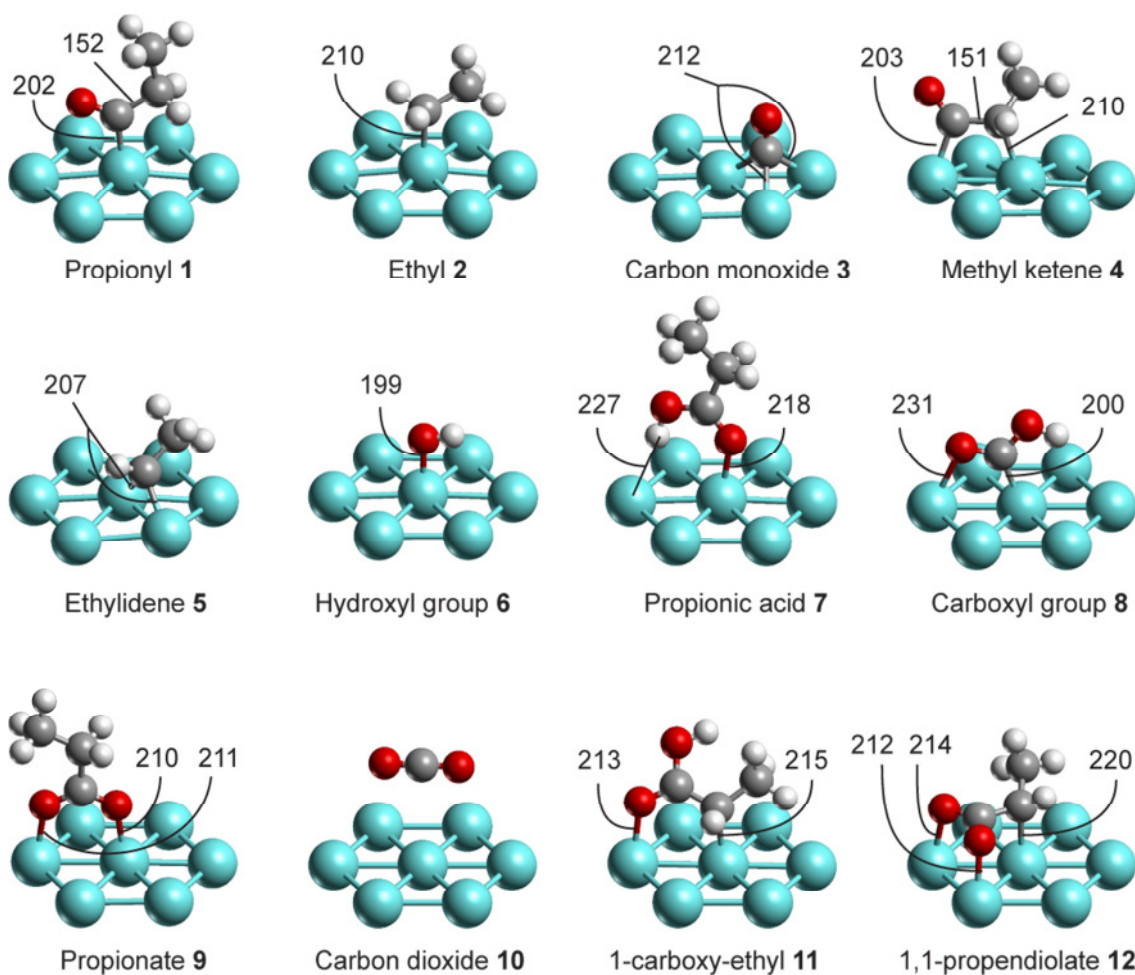


Figure 9.2 Optimized geometries of the intermediates calculated for formation of CO_2 and ethane from propionyl on the flat surface Pt(111). The numbering is as in Figure 9.1. Selected distances are given in pm.

closer to the surface, ~258 pm. Other than this shorter O–Pt distance, the geometries of both adsorbates are nearly identical. Table 9.1 lists the BE values for both adsorbates; the adsorption on the flat surface is 14 kJ mol⁻¹ stronger than on the stepped one. The interaction energy of **1** with the surface is 10 kJ mol⁻¹ larger on the (111) surface; the deformation energies of both the metal surface and the adsorbate species each are only 2 kJ mol⁻¹ larger for the stepped surface structure, Figure 9.4.

9.1.2. Ethyl, MeCH₂ 2& 2'

Ethyl adsorption on Pt(111) occurs at the atop site, depicted in Figure 9.2 as **2**, forming one bond with the surface through the CH₂ carbon in a η^1 (C) fashion. The C–Pt bond formed is 210 pm long, and the C–C bond length is 151 pm. The angle C-C-Pt is 115°. The binding energy is at 195 kJ mol⁻¹.

On the stepped surface ethyl is bound atop an edge Pt atom of the upper terrace. The C–Pt bond length is 209 pm and the C–C bond length is 151 pm, as on the flat surface, see **2'** in Figure 9.3. Only the C–C–Pt angle is slightly smaller, 111°. The BE values are exactly the same on both surfaces for the modes represented, 195 kJ mol⁻¹, whereas the interaction energy is slightly higher on the flat surface, by 6 kJ mol⁻¹ (Table 9.1).

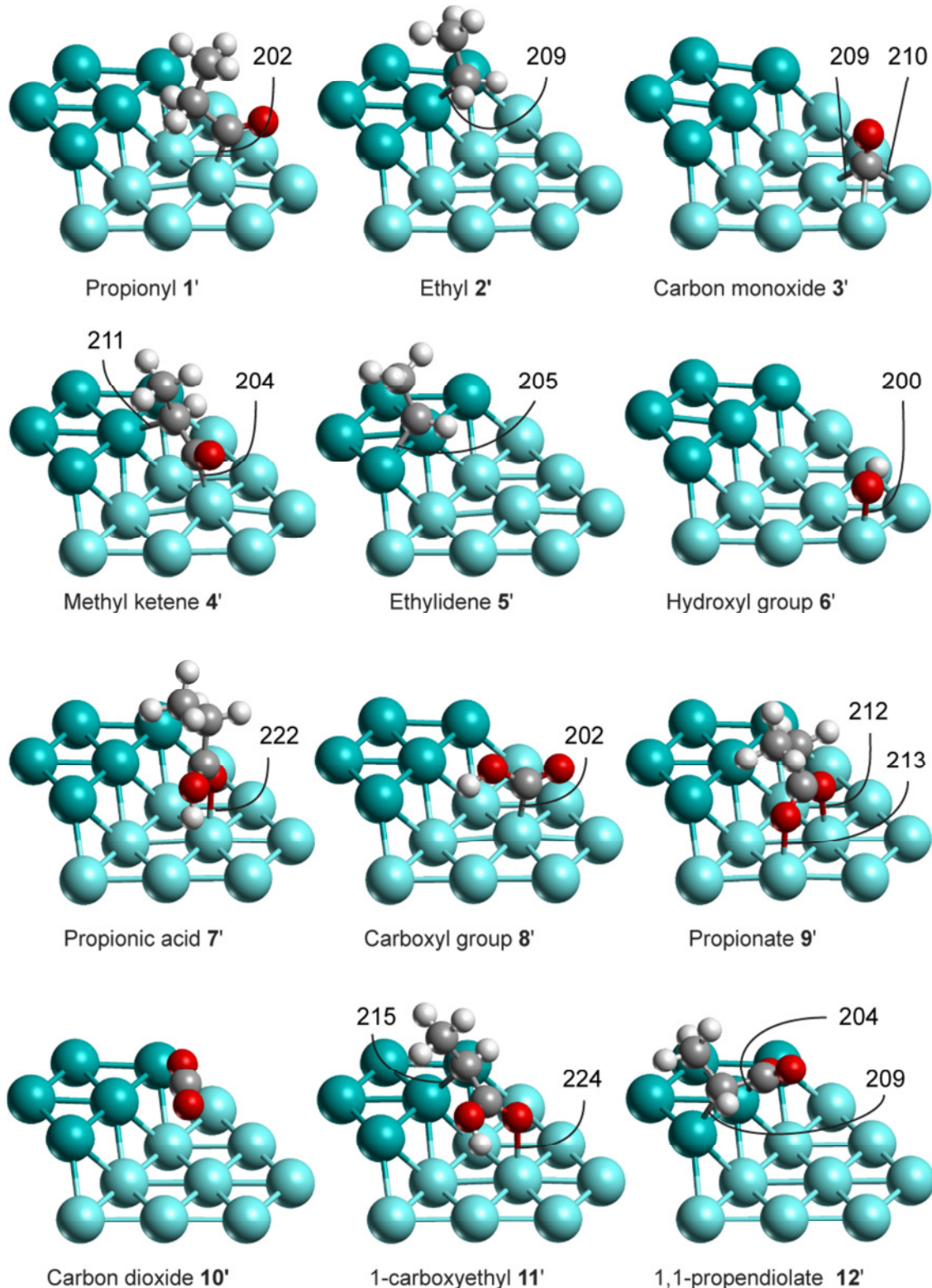


Figure 9.3 Optimized geometries of the intermediates calculated for formation of CO₂ and ethane from propionyl on the close packed Pt(221) surface. The numbering is as in Figure 9.1, identified with a prime (') to represent the stepped surface. Atoms of the upper Pt(111) terrace are rendered in a darker shade. Selected distances are given in pm.

Table 9.1 Energy characteristics (kJ mol^{-1}) of the intermediates $\text{C}_m\text{O}_n\text{H}_x$ ($m = 0 - 3$, $n = 0 - 2$, $x = 4 - 8$) on the Pt(111) and the Pt(221) surfaces at 1/9 coverage.

| Intermediates | | | BE ^a | $E_{\text{int}}^{\text{b}}$ | $\Delta E(\text{M})^{\text{c}}$ | $\Delta E(\text{C}_m\text{O}_n\text{H}_x)^{\text{d}}$ |
|---------------|-------------------|----------------------------|-----------------|-----------------------------|---------------------------------|---|
| 1 | Propionyl | MeCH_2CO | (111) | 233 | 276 | 13 |
| | | | (221) | 219 | 266 | 15 |
| 2 | Ethyl | MeCH_2 | (111) | 195 | 281 | 12 |
| | | | (221) | 195 | 275 | 8 |
| 3 | Carbon monoxide | CO | (111) | 175 | 198 | 9 |
| | | | (221) | 168 | 199 | 16 |
| 4 | Methyl ketene | MeCHCO | (111) | 168 | 432 | 17 |
| | | | (221) | 145 | 447 | 29 |
| 5 | Ethylidene | MeCH | (111) | 390 | 449 | 19 |
| | | | (221) | 405 | 463 | 16 |
| 6 | Hydroxyl group | OH | (111) | 247 | 291 | 4 |
| | | | (221) | 236 | 283 | 7 |
| 7 | Propionic acid | MeCH_2COOH | (111) | 39 | 60 | 6 |
| | | | (221) | 26 | 44 | 4 |
| 8 | Carboxyl group | COOH | (111) | 231 | 278 | 0 |
| | | | (221) | 228 | 273 | 10 |
| 9 | Propionate | MeCH_2COO | (111) | 232 | 298 | 7 |
| | | | (221) | 199 | 262 | 6 |
| 10 | Carbon dioxide | CO_2 | (111) | 4 | 5 | 0 |
| | | | (221) | 6 | 7 | 0 |
| 11 | 1-carboxy-ethyl | MeCHCOOH | (111) | 135 | 273 | 7 |
| | | | (221) | 167 | 239 | 11 |
| 12 | 1,1-propendiolate | MeCHCOO | (111) | 307 | 364 | 12 |
| | | | (221) | 318 | 353 | 14 |

^a Binding energy of $\text{C}_m\text{O}_n\text{H}_x$. ^b Interaction energy of $\text{C}_m\text{O}_n\text{H}_x$. ^c Deformation energy of the surface. ^d Deformation energy of the adsorbate. For the definition of the energies refer to Section 5.1.

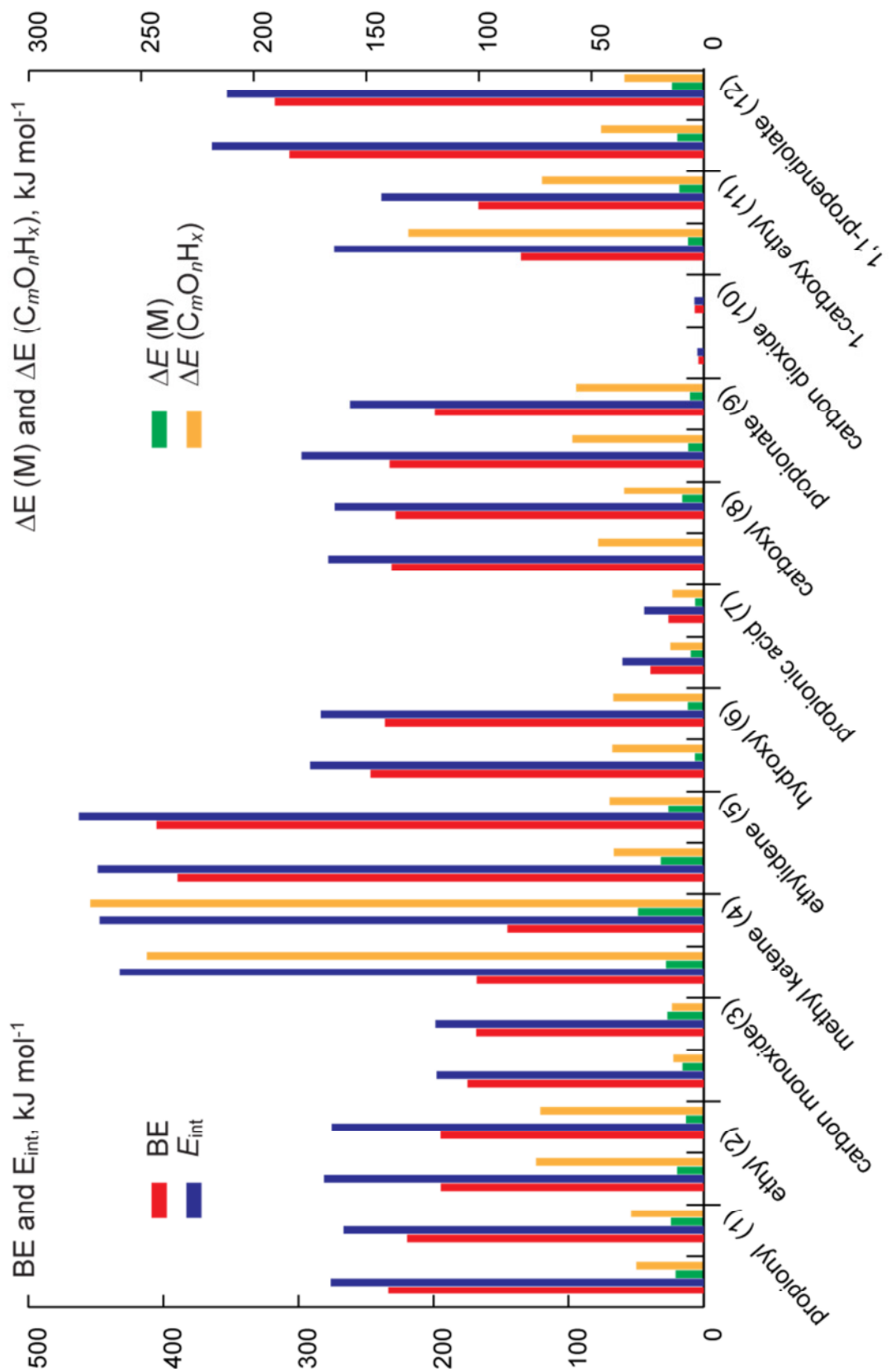


Figure 9.4 Various characteristic energies (kJ mol⁻¹) of the adsorbates as defined in Section 5.1. The values of the species on Pt(111) and Pt(221) is given in the first and second set, respectively.

9.1.3. Carbon monoxide, CO 3& 3'

Adsorption of CO on a Pt(111) surface and surfaces vicinal to it, e.g., a (221) surface employed in this study, is of great interest as CO plays an important role in several technologically relevant reactions such as CO oxidation, Fischer-Tropsch, and WGS reactions.¹²⁵ Experimental methods, including LEED,^{226,227} electron energy loss spectroscopy (EELS),²²⁸⁻²³⁰ scanning tunneling microscopy (STM),^{231,232} all agree on 1-fold coordinated atoms being the preferred adsorption site at low coverage on both flat and stepped surfaces and as the surface coverage increases, CO adsorption on bridge sites starts.

However common Kohn-Sham DFT methods fail to reproduce these phenomena not only on Pt but also on Cu, Rh, Ag, and Au surfaces both qualitatively and quantitatively.²³³ This contradiction between the findings of experiments and Kohn-Sham calculations, which is presented as “CO puzzle”, is very well documented and has been first thoroughly examined by Feibelman et al.²³⁴ in their now classical paper about CO adsorption on Pt(111) and surfaces vicinal to it employing the local-density or the generalized-gradient approximation (semi-local) as exchange functionals. The use of these functionals results in the preference of hollow sites as most stable on Rh, Pt, and Cu and degenerate hollow and top sites on Ag and Au, along with overestimated adsorption energies.^{233,234} Gil et al.²³⁵ did DFT calculations on CO adsorption over the Pt (111) surface for both cluster and periodic slab models to reach the same conclusions. Their investigations showed that the inadequately described energy gap between the highest occupied molecular orbital and the lowest unoccupied molecular orbital (HOMO-LUMO gap) is responsible for this behavior. This explanation was further supported by other studies;^{236,237} the high-coordination sites bind the molecule stronger as a result of the wrongly positioned LUMO orbital which interacts stronger with the d-band of the surface. The $2\pi^*$ orbitals of CO lie too low due to the self-interaction error of common approximate exchange-correlation functionals. As a result, back-donation to these orbitals is facilitated.

As an improvement, it was suggested to employ hybrid functionals, which replace part of the exchange energy with the exact exchange of the Kohn-Sham determinant.²³⁵ Doll employed the B3LYP method, a hybrid functional, and calculated the right adsorption order for Pt(111) surface.²³⁸ Hybrid functionals of Perdew-Becke-Ernzerhof (PBE) – PBE0, HSE03 and a variant of HSE06 – in the PAW formalism were also employed to address this problem.^{239,240} The PBE functional itself prefers adsorption at hollow site of Pt(111) surface by ~ 15 kJ mol⁻¹ and overestimates the binding energy by 40 kJ mol⁻¹ compared to experiment.²⁴¹ Although employing of hybrid functionals improved the situation in some cases, the results obtained are not satisfactory as the ordering of the sites is not improved for

Pt and the adsorption energies are still overestimated. More importantly, the description of the metal is worse when one employs an admixture of the exact exchange. Hence, although there is minor improvement in CO adsorption energies it is mostly at the expense of other properties, such as the incorrect description of the metal bandwidth properties; the d-band width increases when non-local exchange is included.^{239,240} A recent study employing a meta-GGA functional (M06-L), with no non-local exchange inclusion, brings a significant improvement on both the metal and the adsorption properties.²⁴² The advantage of a meta-GGA is that it further expands the exchange-correlation potential to include the kinetic energy density. Results from calculations with the M06-L functional predict the right adsorption site, atop on Pt(111), by ~35 kJ mol⁻¹ over the fcc site. Also the binding energy calculated for the atop adsorption site,²⁴² 143 kJ mol⁻¹, is within the error margin of the experiments, 132±13 kJ mol⁻¹.^{178,241}

In this study the GGA functional PW91 was employed, hence the most stable site was calculated to be the fcc hollow site. In the structure with CO adsorbed at the hollow site all three C–Pt bonds on the flat surface are 212 pm, see Figure 9.2. On the stepped surface the most stable site as a result is actually the 2-fold step-edge site as a result of using the PW91 functional.²³⁴ However as the CO molecule here is a product of the decomposition reactions (**a**) or (**c**), solely the adsorption of CO on the terrace site is investigated, Figure 9.3. On the terrace of the (221) surface the molecule adsorbs also at fcc hollow site, with C–Pt bonds ranging from 209 to 211 pm. The C–O bond is 119 pm and 120 pm on the (111) and (221) surface, respectively. The BE on the (111) surface is 175 kJ mol⁻¹, overestimating the experimental value by ~40 kJ mol⁻¹ as with the PBE functional.²⁴¹ On Pt(221) surface, the binding energy is only 7 kJ mol⁻¹ lower, Table 9.1. The difference is mostly caused by the 5 kJ mol⁻¹ higher deformation of the metal substrate, Figure 9.4.

9.1.4. *Methyl ketene, MeCHCO 4& 4'*

As in the case of propionyl, methyl ketene **4** on the flat surface has already been inspected in Section 8.1.5 and it is depicted in Figure 9.2. The adsorption mode on the stepped surface is the same as on the flat surface; $\eta^1\eta^1(\text{C},\text{C})$. However on this surface the carbonyl C is bound to a lower terrace Pt atom and the α -C is bound to a Pt atom of the upper terrace. The C–C and C–Pt bonds on the two surfaces differ only by 1 pm; C–C = 151–152 pm, C₁–Pt = 203–204 pm, and α -C–Pt = 210–211 pm. The adsorbate binds 23 kJ mol⁻¹ stronger on the flat surface than on the stepped surface. However, the deformation of the structure on the stepped surface is stronger, which is reflected in the higher binding energy on the flat surface; the deformation energy from the gas phase to the adsorbed structures is 25 kJ mol⁻¹ higher for

4' than that for **4** as listed in Table 9.1. This molecule is, after ethylidene, the one that interacts strongest with the surface as deduced from the interaction energies, E_{int} , on both surfaces, Figure 9.4. However it is the one that deforms the most, $\Delta E(\text{MeCHCO}) = 247$ and 273 kJ mol^{-1} on flat and stepped surfaces, respectively. The changes of the molecule at the flat surface have already been mentioned in Section 8.1. The linear O-C-C angle in the gas phase narrows down even more when adsorbed on the stepped surface than is the case on the flat surface. This is also reflected in the higher deformation energy, Table 9.1. Adding all contributions together, the binding energy of methyl ketene on the stepped surface is computed lower than that on the flat surface, Figure 9.4.

9.1.5. Ethylidene, MeCH 5& 5'

Ethylidene (**5**) binds at bridge sites of Pt(111), in $\eta^1\mu_2$ fashion (Figure 9.2). The calculated C–C bond length is 150 pm, indicating single-bond character. The two C–Pt distances, 207 pm, are equal and the binding energy of this species is calculated at 390 kJ mol^{-1} (Table 9.1).

On the stepped surface, MeCH **5'** binds at the step-edge of the upper terrace, in the same $\eta^1\mu_2$ fashion as on the flat surface, see **5'** in Figure 9.3. The C–Pt bonds are slightly shorter, 205 pm, but the C–C bond length remains the same. The adsorption on the step-edge of the stepped surface is 15 kJ mol^{-1} stronger than on the flat (111) surface; see Table 9.1. The interaction energies of the molecule with the surfaces are highest for ethylidene, $E_{\text{int}} = 449 \text{ kJ mol}^{-1}$ and 463 kJ mol^{-1} for the flat and the stepped surfaces, respectively. As deformation energies of adsorbed ethylidene on both surfaces are much lower than those of methyl ketene, **4**, the resulting BE values are the highest among the structures in this part of the study, Figure 9.4.

9.1.6. Hydroxyl group, OH 6& 6'

The hydroxyl group adsorbs atop a Pt atom on both surfaces, Figures 9.2 and 9.3. On Pt(111) this site has been found to be the most stable in the literature.²⁴³, Adsorption at a bridge site on the edge of the stepped surface is calculated to be more favorable according to DFT calculations by Lew et al.²⁴⁴ However, here the adsorbed structure at the terrace is presented, adsorbed in the same mode as on the flat surface. OH **6'** adsorbed in this mode will be inserted into propionyl **1'**, which is also adsorbed at the terrace as shown in Figure 9.3 via the reaction depicted as (**d**) in Figure 9.1. The O–Pt bond length is 199–200 pm, O–H is 98 pm for both structures. The Pt–O–H angle is 106° on the flat surface and 104° on the stepped surface. This similarity in the adsorption modes is reflected in the structure deformation

energies; they differ by only 1 kJ mol⁻¹, Table 9.1. The adsorption energy of the OH group is 247 kJ mol⁻¹ and 236 kJ mol⁻¹ on the flat and stepped surfaces, respectively, which is high as it is expected for a radical. All these parameters are similar to those calculated by Michaelides and Hu.²⁴³

9.1.7. *Propionic acid, MeCH₂COOH 7& 7'*

Propionic acid **7** is weakly adsorbed on both surfaces in $\eta^1(\text{O})$ mode, atop a Pt atom. The MeCH₂ moiety is directed away from the surface and the H atom of the OH moiety points to the surface for both **7** and **7'**, Figures 9.2 and 9.3, respectively. The O–Pt bond length on the stepped surface is 222 pm, 4 pm longer than the value on the flat surface, which is also reflecting the weaker adsorption on the stepped surface represented by the BE values; the values in Table 9.1 show that there is a 13 kJ mol⁻¹ difference between the two surfaces, and this difference is also similar for the interaction strength, E_{int} . Bournel et al.^{245,246} confirmed that propionic acid is physisorbed on the surface at 95 K based on several experimental investigations, i.e. NEXAFS, XPS, Ultraviolet photoelectron spectroscopy (UPS) and Fourier transform reflection absorption infrared spectroscopy (FT-RAIRS). Lu et al.¹⁹⁰ considered adsorption of the same molecule on the Pd(111) surface. As it has been presented in the first part of the thesis (Part I), Pt and Pd(111) surfaces have similar adsorption properties of molecules to a large extent. This phenomenon holds also in this case; the molecule adsorbed on the Pd(111) surface also adsorbs through the O atom but it is differently tilted from the surface.¹⁹⁰ The structure Lu et al. calculated features an adsorption complex where $\alpha\text{-C-C}_1$ axis is parallel to the surface plane;¹⁹⁰ propionic acid adsorbed in such a style on the Pt(111) surface is shown in Figure 9.5 as the parallel adsorption mode (propionic acid^l) and is 38 kJ mol⁻¹ less stable than the one described above and depicted as **7** in Figure 9.2.

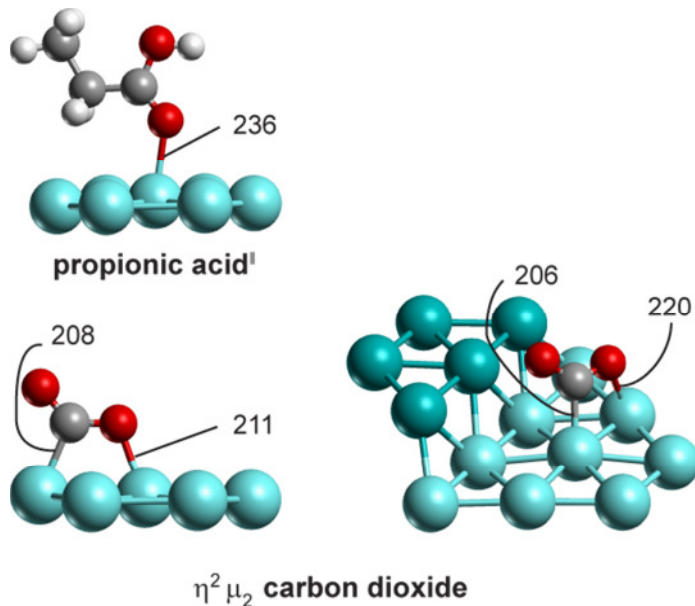


Figure 9.5 Optimized structures of adsorption complexes proposed in the literature for propionyl conversion to ethane and CO_2 . This mode of propionic acid is suggested in Ref. 190, of carbon dioxide in Ref. 248.

9.1.8. Carboxyl group, COOH 8& 8'

The carboxyl group binds on the flat (111) surface in $\eta^2(\text{C},\text{O})$ mode, see structure **8** in Figure 9.2. The molecule lies closer to the surface on its C end, O–Pt being 231 pm and C–Pt 200 pm long. The O–C–O angle is 118° , the C–O bond length is 125 pm for O and 133 pm for OH. The former value is 6 pm elongated from its value in the gas phase and the latter is 2 pm shorter; all these changes result in a 47 kJ mol^{-1} deformation energy of the carboxyl group, Table 9.1.

On the terrace of the stepped surface, the carboxyl group binds only through the C atom atop a Pt atom, as shown in Figure 9.3 as **8'**. The molecule is less bent, O–C–O = 122° , than on the flat surface, and the C–O bonds are changed to a lower extend from their gas phase values, C–O = 121 pm for O and 134 pm for the hydroxyl, which is reflected in a slightly lower deformation energy, 35 kJ mol^{-1} . The adsorption energies are within 3 kJ mol^{-1} with 231 kJ mol^{-1} and 228 kJ mol^{-1} for the flat and stepped surface, respectively.

9.1.9. Propionate, MeCH_2COO 9& 9'

The adsorption of propionate occurs on both surfaces through the O atoms in a bidentate form. The adsorption mode on the flat surface, depicted as **9** in Figure 9.2, shows the molecule adsorbed in upright orientation, parallel to the surface normal. The O–Pt bonds

are almost the same length, 210 and 211 pm. Both C–O bond lengths are 128 pm and the O–C–O angle is 128°. This geometry is the same one as observed by Avery.¹⁸³ Graham²⁴⁷ also mentions a perpendicular adsorption of propionate on the (111) surface on bridge sites. This bidentate adsorption mode of propionate **9** is strongly bound, 232 kJ mol⁻¹ (see Table 9.1). On the Pd(111) surface Lu et al.¹⁹⁰ also suggest the same mode of adsorption for this molecule with a similar high BE, 249 kJ mol⁻¹ including a 5 kJ mol⁻¹ zero-point-energy correction.

Propionate adsorbs also through the O atoms on the (221) surface to two Pt atoms of the terrace, see **9'** in Figure 9.3. This adsorption mode is the most stable one on this surface. In this geometry the O–Pt bond lengths are 212–213 pm, with other properties the same as on the flat surface. As one can deduce from the deformation energies of **9** and **9'** given in Table 9.1, the molecules adsorbed on both surfaces are distorted the same amount, however the BE is ~30 kJ mol⁻¹ lower on the (221) surface.

9.1.10. Carbon dioxide, CO₂ **10**& **10'**

The interaction of CO₂ **10** with the surface is very weak due to its very stable gas phase form. Both on the flat and on the stepped surfaces the values of BE and E_{int} are low, see Figure 9.4, and as conventional DFT methods lack dispersion effects, the physisorption strength is also not well described. Alavi et al.²⁴⁸ determined an η^2 (C,O) adsorbed mode of CO₂ as the product of CO oxidation reaction via DFT calculations at LDA level with a bent O–C–O angle, 131°, and unequal C–O bond lengths, 121 and 129 pm. Such an adsorption geometry, $\eta^2\mu_2$ (Figure 9.5) calculated at the GGA level resulted in an adsorption complex that is 24 kJ mol⁻¹ less stable on the flat surface; hence even the binding energy is negative, indicating an unfavorable interaction. The same mode on a stepped surface shows also no favorable adsorption, with BE = -41 kJ mol⁻¹. The stable structures are depicted as **10** in Figure 9.2 and as **10'** in Figure 9.3; the structure of the molecule is similar to its gas phase congener – C–O bond lengths ~118 pm and a 180° O–C–O angle – with no deformation energies in either case. The result by Lu et al.¹⁹⁰ on Pd(111) predicts the same mode with a similar BE.

9.1.11. 1-carboxy-ethyl, MeCHCOOH **11**& **11'**

1-carboxy-ethyl forms on the surface through dehydrogenation of propionic acid **7** at the α -C center. On the flat surface the species adsorbs in an η^2 (C,O) mode at a bridge site on the surface, **11** in Figure 9.2. The O–Pt bond length is 213 pm and the C–Pt bond length is 215 pm. The C–OH bond shrinks upon adsorption by 4 pm and the C–O bond elongates by 3 pm; both C–C bonds are elongated by 4–5 pm. The adsorption mode on the stepped surface is

the same as on the flat surface, only this time the C atom is bound to a Pt atom of the upper terrace, see Figure 9.3. Apart from the O–Pt distance being 11 pm longer, 224 pm, all the bonds are the same within ~1 pm as in the molecule adsorbed on the flat surface. Although other geometrical parameters, such as angles and dihedral angles of the molecule on the flat surface, are closer to their values in the gas phase molecule, the deformation energy of the adsorbed structure is higher on the flat than on the stepped surface, Table 9.1. This inconsistency between the extent of deformation and the resulting deformation energies partly explains the stronger binding energy on the stepped surface, however the difference in the interaction energies shows that the molecule is not interacting as strongly with the stepped surface as it does with the flat surface.

9.1.12. 1,1-propendiolate, MeCHCOO 12& 12'

1,1-propendiolate forms either through dehydrogenation of **9** at the α -C or of **11** at the hydroxyl group. On the flat surface the molecule **12** is adsorbed in an $\eta^3(\text{O},\text{O},\text{C})$ mode, at an hcp-threefold site. The O–Pt bond lengths are 212 and 214 pm and the C–Pt bond length is 220 pm. The C–O bond lengths are 130 and 131 pm; the elongation from the structure in the gas phase molecule is ~2–3 pm. The C–C bond between the methyl group and the α -C elongates 4 pm upon adsorption to 150 pm where the α -C–C₁ bond elongates 2 pm to 148 pm.

On the stepped surface 1,1-propendiolate **12'** adsorbs through a C atom and one O atom, at a bridge site on the step of the upper terrace, Figure 9.3. The C–O bond which is not interacting with the surface contracts to 123 pm, hence is transforming into a double bond. The other C–O bond elongates 5 pm to 133 pm, and the same O atom binds to a surface Pt at a distance of 204 pm. The C–Pt bond also shortens to 209 pm on the stepped surface. Both C–C bonds are 152 pm.

The binding of 1,1-propendiolate to the surface is stronger than 300 kJ mol⁻¹, placing it as the second most strongly adsorbed species after ethyldene for the surfaces and the molecules considered in this study. The adsorption on the stepped surface is 10 kJ mol⁻¹ stronger than that on the flat surface, which apparently is due to a more deformed structure on the flat surface, $\Delta E(M) \sim 10$ kJ mol⁻¹ (Table 9.1).

9.2. Reactions

In this section the reactions depicted in Figure 9.1 are described in detail both on the flat surface and on the stepped surface. The elementary steps are separated into reactions on the way to decarbonylation or decarboxylation, according to the final C–C bond scission which they undergo. Hence, from Figure 9.1, steps **(a)–(c)** are explained for the

decarbonylation pathway whereas steps (e)–(k) and (m) are included in the decarboxylation pathway. The reactions on the stepped surface are again labeled with a prime next to their identifiers as for the intermediates. Not all the steps in the network are studied on the stepped surface; step sites are only considered when there is a possibility for a substantially lower barrier via these sites.

The comparison of the reaction energies and activation barriers is given in Table 9.2. The transition state structures on the flat and stepped surfaces are sketched in Figures 9.6 and 9.7, respectively. As the orientation of the transition states on the stepped surfaces sometimes makes it harder to see easily the described structure, additional views are provided in Figure 9.8.

In the following the reaction network will be investigated in three subsections; decarbonylation and decarboxylation pathways as explained above and one more reaction – the hydroxyl insertion into propionyl **1** to form propionic acid **7** – are presented separately. The hydroxyl insertion is an important step as it opens up the path to decarboxylation routes. In addition, this part deals with the source of OH groups on the surface, water splitting. The results on the flat and stepped surfaces are discussed together, comparing the energetics and the geometries on both surfaces.

9.2.1. Decarbonylation

(a) $\mathbf{1} \rightarrow \mathbf{2} + \mathbf{3}$

The propionyl molecule **1** adsorbed on the flat surface decomposes into ethyl **2** and CO **3** via the scission of the α -C–C₁ bond. The C atom of the CH₂ moiety, α -C starts to interact with a Pt atom of the surface and gets closer to the surface as the C–C bond starts to stretch. When the α -C–Pt distance shortens to 230 pm, the C–C bond reaches 205 pm and at that geometry the transition state **TSa** occurs, as shown in Figure 9.6. The C₁–Pt distance shrinks at **TSa** by 9 pm to 193 pm. One of the α -H atoms binds also to the surface Pt atom at a distance of 193 pm. After reaching the transition geometry, the reaction proceeds so that ethyl **2** remains bonded atop the same Pt atom and CO **3** migrates to a threefold fcc site, both calculated as the most stable sites on the (111) surface.

When propionyl is adsorbed on the stepped surface the initial α -C–Pt distance is 334 pm; 23 pm shorter than the value on the (111) surface, 357 pm. The transition state **TSa'** occurs when the interaction between the α -C and Pt strengthens and the distance shrinks to 228 pm, Figure 9.7, which is 15 pm shorter than that of the **TSa**. The C–C distance at the TS is only 4 pm shorter at the stepped surface, 203 pm.

Table 9.2 Energies of the reactions (in kJ mol^{-1}) involved in the formation of CO_2 and ethane from propionyl on Pt(111) and Pt(221) surfaces. E_r and E_r^{inf} are reaction energies at close proximity and infinite distance, respectively, and E_a is the activation barrier.

| Reactions | | | E_r | | E_r^{inf} | | E_a | |
|------------------------|--|--|-----------------|-----------------|-------------|-------|-----------------|---------|
| | | | (111) | (221) | (111) | (221) | (111) | (221) |
| (a) | 1 | $\rightarrow \mathbf{2 + 3}$ | -49 | -54 | -45 | -53 | 134 | 106 |
| (b) | 1 | $\rightarrow \mathbf{4 + H}$ | 4 | 17 | -6 | 15 | 91 | 75 |
| (c) | 4 | $\rightarrow \mathbf{3 + 5}$ | -33 | -68 | -6 | -66 | 91 | 83 |
| (d) | 1 + OH | $\rightarrow \mathbf{7}$ | -46 | | -59 | | 31 | |
| (e) | 7 | $\rightarrow \mathbf{2 + 8}$ | -4 | -14 | 2 | -9 | 219 | 204 |
| (f) | 7 | $\rightarrow \mathbf{9 + H}$ | -11 | | -16 | | 44 | |
| (g) | 9 | $\rightarrow \mathbf{2 + 10}$ | -45 | -24 | 13 | -23 | $\sim 300^a$ | 142 |
| (h) | 7 | $\rightarrow \mathbf{11 + H}$ | 27 | 2 | 33 | 1 | 118 | 57 |
| (i) | 11 | $\rightarrow \mathbf{5 + 8}$ | -42 | 18^b | -27 | -8 | 108 | 110^b |
| (j) | 9 | $\rightarrow \mathbf{12 + H}$ | 67 | 31 | 56 | 24 | 142 | 85 |
| (k) | 11 | $\rightarrow \mathbf{12 + H}$ | 18 | | 7 | | 50 | |
| (m) | 12 | $\rightarrow \mathbf{5 + 10}$ | -43 | -41 | -39 | -40 | 119 | 86 |
| WS | H_2O | $\rightarrow \mathbf{H + OH}$ | 58 ^c | 66 ^c | | | 90 ^d | |
| WGS^e | $\text{CO} + \text{H}_2\text{O}$ | $\rightarrow \mathbf{\text{CO}_2 + H}_2$ | | | 23 | | 104 | |

^a Estimated value; see Section 9.2.3. ^b Effective reaction energy and effective activation barrier relative to **11** that is 14 kJ mol^{-1} lower in energy than the actual initial state **ISi'** of bond breaking (see Section 9.2.3). ^c Based on the energy values of **IS(1+6)+H** relative to **1+H₂O**. ^d Estimated value; see Section 9.2.2^e Energy change for the total conversion and the highest barrier relative to the adsorbed IS; Grabow et al.²⁵⁰

The calculated reactions are exothermic on the flat and the stepped surfaces with -46 kJ mol^{-1} and -54 kJ mol^{-1} , respectively. The difference of 8 kJ mol^{-1} between the reaction energies on the two surfaces is very close to the binding energy differences of the products and reactants on the two surfaces as listed in Table 9.1. The reaction energies at infinite separation, E_r^{inf} , as given in Table 9.2 are almost the same as the reaction energies, E_r , when the products are located close to each other immediately after bond dissociation. The barriers, however, are more separated; on the flat surface it is 134 kJ mol^{-1} whereas it drops to 106 kJ mol^{-1} on the stepped surface. This decrease is in part due to the difference in the binding energies. Furthermore, there is apparently another contribution, which is due to the

geometrical advantage of the stepped surface as the molecule at the transition state is much more stabilized through a shorter α -C–Pt distance, hence a stronger interaction with the surface. Here, as CO is one of the products and its BE is overestimated by the employed functional, PW91, a lower BE of the product CO as in experiment, see Section 9.1.3, would imply that the reaction is more endothermic (or less exothermic), which would increase the barrier accordingly, assuming that the BEP correlation holds.^{118,119}

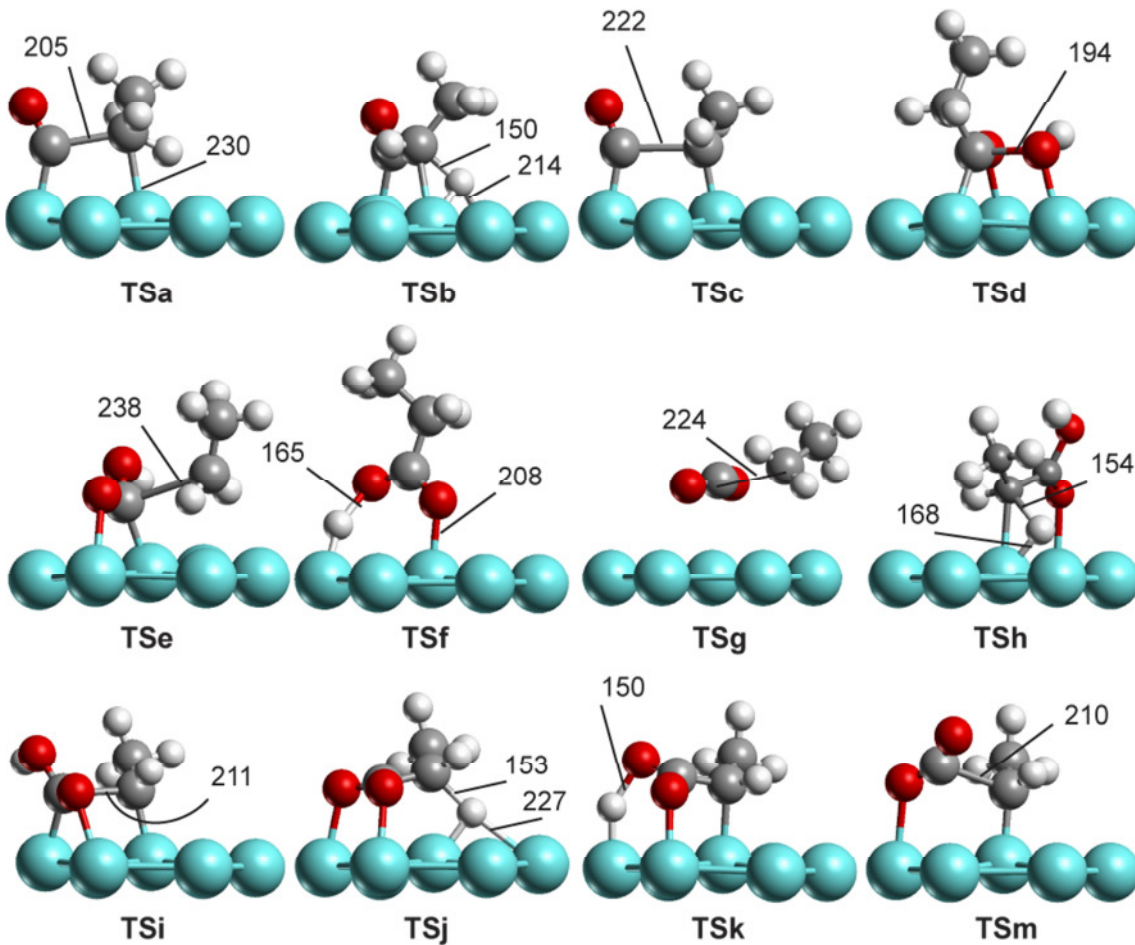


Figure 9.6 Structures of the transition states (TS) at Pt(111) surface in the reaction network studied as calculated for conversion of propionyl to carbon dioxide and ethane on the flat surface Pt(111). Selected distances are given in pm.

Lu et al.¹⁹⁰ investigated the decarbonylation reaction of propionyl **1** on a Pd(111) surface. They determined the $\eta^2\mu_3$ mode of propionyl as most stable on the Pd(111) surface; that structure is the analogous to the one discussed in Section 8.1.4 and represented in Figure 8.3. Nevertheless, in their reactivity study they also used the atop adsorption site for the reaction under investigation. The values they calculated with atop adsorbed propionyl as the

IS are -63 kJ mol^{-1} for the reaction energy and 154 kJ mol^{-1} for the activation barrier. As the first part of the thesis advocates, the energetics of this reaction is close to that on Pt surfaces.

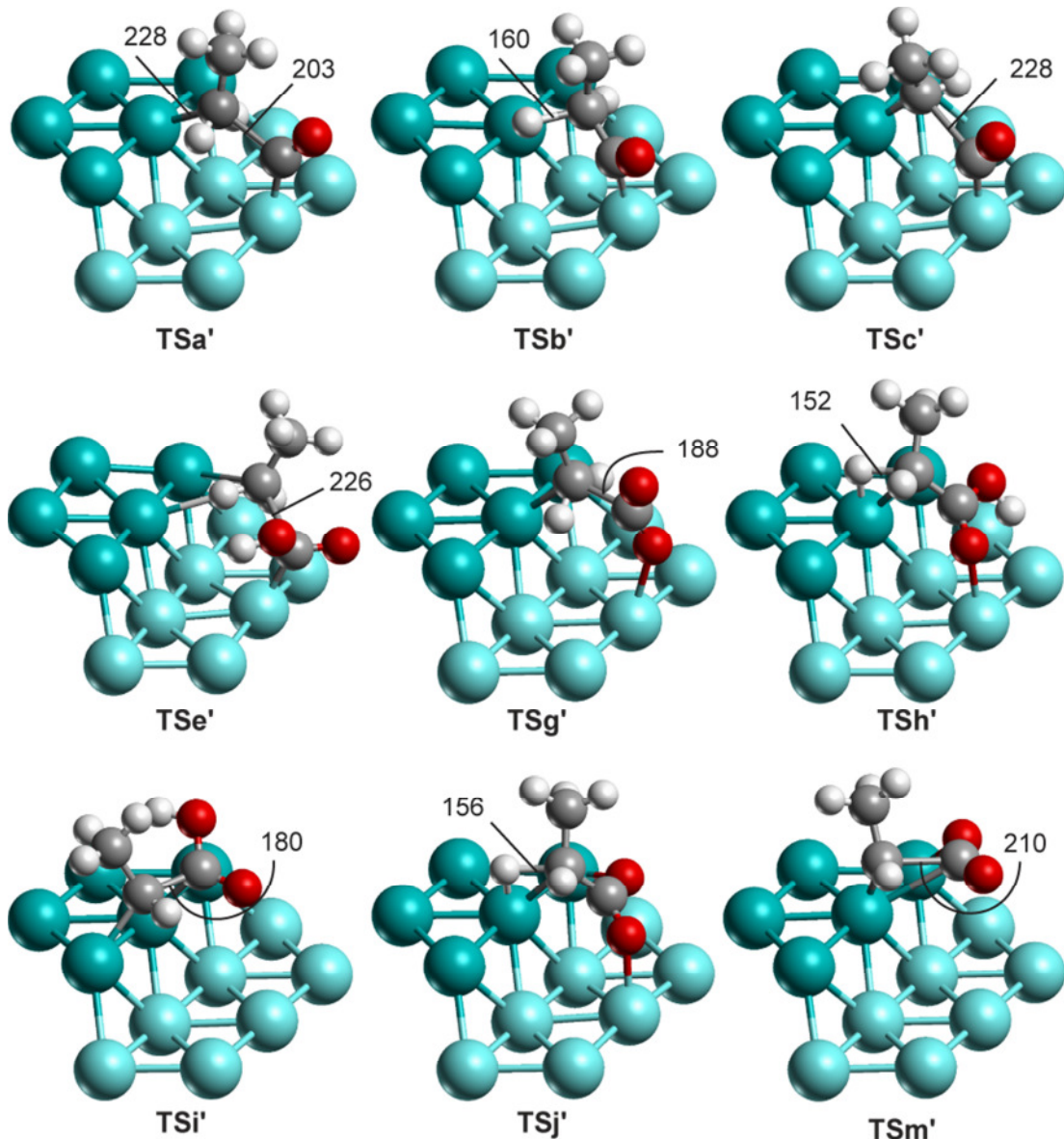


Figure 9.7 Structures the transition states (TSs) on Pt(221) stepped surface for the conversion of propionyl to carbon dioxide and ethane. Selected distances are given in pm.

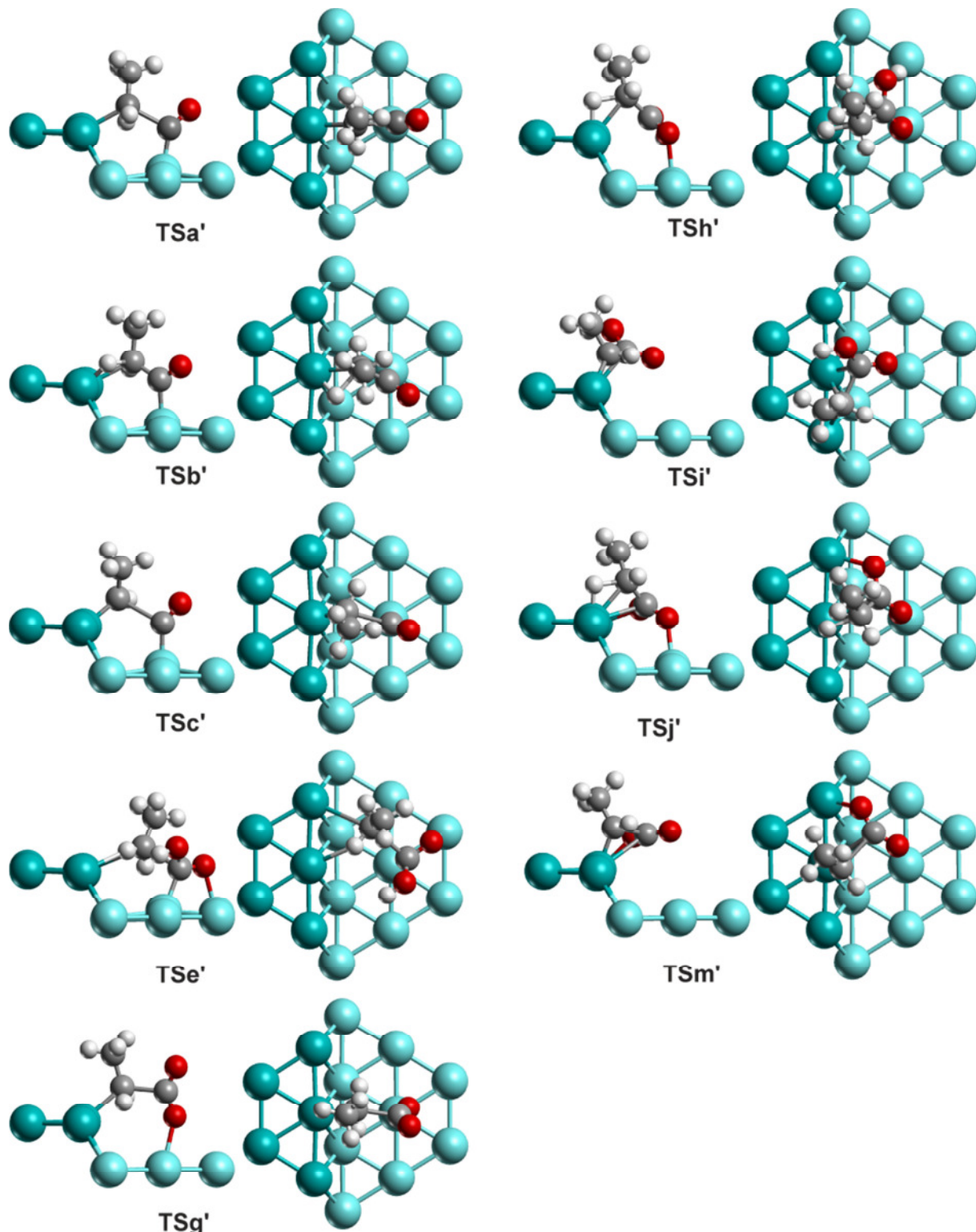


Figure 9.8 Calculated structures of transition states of propionyl conversion to ethane and CO₂ on the stepped surface Pt(221): top and side views.

(b) $\text{I} \rightarrow \text{4} + \text{H}$

This reaction on the flat surface has been detailed before (Section 8.2.4) in the part dedicated to dehydrogenation. Hence in this section only the values for the stepped surface will be discussed and compared to the results determined on the flat surface. On the stepped surface the hydrogen to be extracted is already oriented towards a Pt atom at the step-edge. This orientation rationalizes the shortened H–Pt distance, 228 pm, in the IS from that on the flat surface, H–Pt = 312 pm. The molecule **1'** starts bending towards the step-edge and the H atom starts to interact with the Pt atom, weakening the bond with the α -C. At **TSb'** (Figure 9.7) the H–Pt distance dropped to 162 pm and the C–H bond is elongated to 160 pm. On the flat surface the corresponding structure **TSb** has an H–Pt distance of 169 pm. On the stepped surface the C–H distance elongates to 150 pm and the α -C starts interacting with a Pt atom, C–Pt = 232 pm, as shown Figure 9.6. At **TSb'**, the α -C–Pt distance is 230 pm.

The reaction on the (111) surface is almost thermoneutral, 4 kJ mol⁻¹, and on the stepped surface it becomes slightly more endothermic, 16 kJ mol⁻¹. One part of this increase in the reaction energy is the difference in between the BE values of the propionyl **1** and methyl ketene **4** on the two surfaces; the BE values of both the reactant propionyl and the product methyl ketene decrease on the stepped surface. However the decrease on the product side is 10 kJ mol⁻¹ more. Although the reaction gets more endothermic on the stepped surface, the barrier that the reaction has to go over decreases from 91 kJ mol⁻¹ on the flat surface to 75 kJ mol⁻¹ on the stepped surface.

(c) $\text{4} \rightarrow \text{3} + \text{5}$

The decomposition of methyl ketene **4** proceeds through a C–C bond scission of the molecule. The C atoms involved in this bond already bind to surface, as seen from **4** and **4'** in Figures 9.2 and 9.3, respectively. The transition states of the reaction are depicted as **TSc** in Figure 9.6 on the flat surface and as **TSc'** in Figure 9.7 on the stepped surface. At the TS geometry there is little change from the reactant state geometry. The only significant difference is the C–C bond lengths as expected, on the flat surface the bond elongates to 222 pm and on the stepped surface to 228 pm. The close resemblance of the TS structures to those of the reactants suggests that the reactions are exothermic according to Hammond's postulate.¹²² Indeed the reaction energies are -33 kJ mol⁻¹ and -68 kJ mol⁻¹ on the flat and on the stepped surface, respectively. The activation energy for this C–C bond scission reaction is 91 kJ mol⁻¹ on the flat surface and 83 kJ mol⁻¹ on the stepped surface.

The products of reactions **(a)** and **(c)** are not those observed in the experiments. Ethyl **2** from reaction **(a)** and ethylidene **5** from reaction **(c)** have to be fully hydrogenated to ethane, which is experimentally detected in the product stream both in the presence and in the absence of H₂.^{25,172,178} Zhao et al.²¹ calculated the reaction energies and barriers for these hydrogenations in their work on ethylidyne formation from ethylene on Pt(111). Ethylene hydrogenation to ethyl at 1/9 coverage is thermodynamically almost neutral, -6 kJ mol⁻¹, going over a barrier of 68 kJ mol⁻¹. The highest hydrogenation barrier is that of ethyl to ethane, 77 kJ mol⁻¹, associated with a reaction energy of 12 kJ mol⁻¹. These barriers are comparable to the barriers of preceding C–C scissions and dehydrogenations; hence hydrogenation of the products will not be the rate-limiting step.

CO is the other product formed in both reactions **(a)** and **(c)**. In the absence of water CO adsorbs strongly on the surfaces of Pt catalysts, poisoning them by completely covering the surface.²⁴⁹ In the experiments^{21,154} the level of CO₂ obtained was as high as that of ethane. If the reaction proceeds via decarbonylation the CO adsorbed on the surface must be oxidized to CO₂. The water gas shift reaction is very likely under the experimental conditions of these APR conversions. Grabow et al. investigated the reaction mechanism for CO transformation into CO₂ and H₂ via the inclusion of a water molecule.²⁵⁰ From the network of reactions they considered, the optimal route proceeds over a COOH intermediate. In the conversion of adsorbed CO and H₂O to CO₂ and 2 H adsorbed at the surface, the highest barrier for an elementary reaction was that of water splitting calculated at ~85 kJ mol⁻¹. For the overall route the highest barrier was 104 kJ mol⁻¹, that of OH insertion into adsorbed CO, and the total conversion is 23 kJ mol⁻¹ endothermic, see Table 9.2.

9.2.2. *Insertion of a hydroxyl group*

Wawrzetz et al.,²⁵ Peng et al.,¹⁷² and Lobo et al.¹⁷⁸ conducted experiments on propanol in aqueous solution. These studies reported propionic acid in their product stream, although the various yields were not comparable. At the conditions the experiments were done, water dissociation is also probable, hence the possibility of hydroxyl groups adsorbed on the surface cannot be disregarded. First, an overlook will be given of how the hydroxyl groups might form.

The behavior of water on the solid surfaces is a subject of great interest in many fields; in chemistry especially electrochemistry, heterogeneous catalysis, and corrosion.^{209,251,252} Water adsorption/desorption and dissociation/formation play an important part in many catalytic processes such as steam reforming of natural gas, WGS, Fischer-Tropsch synthesis,

and the present case, APR of biomass.^{161,209,253} A vast amount of publications report experimental or theoretical works on water splitting. Yet this topic is still a matter of discussion about how this reaction proceeds under various different conditions.

On the clean Pt(111) surface water has been shown to be adsorbed molecularly rather than dissociatively.^{209,251,252} Impurities on the surface greatly affect the behavior of water molecules. When atomic oxygen is coadsorbed on the surface, the water molecule readily dissociates with an activation barrier of ~43 kJ mol⁻¹, reacting with the adsorbed water in a 1:2 ratio to produce hydroxyl groups on the surface.²⁵¹ Coadsorption of molecular oxygen at low temperature, however, does not promote dissociation. When CO is coadsorbed with water, CO molecules change their preferred site; instead of being adsorbed at an atop site which is the most stable site for the clean surface, the molecules are located at bridge sites.²⁵¹ Wang et al. modeled dissociation of a single molecule of a water double bilayer in the presence of CO and obtained lower activation barriers than without CO, by 44 kJ mol⁻¹. The reactions energies did not change considerably; it decreases only by 8 kJ mol⁻¹.²¹³

There are several theoretical studies dealing with the kinetics of water dissociation on Pt(111) surfaces. Some of these studies use a single water molecule to calculate the reaction energy and the activation barriers.^{161,250,253,254} The values computed in these works are listed in Table 9.3 along with the computational parameters employed. The reaction energies for the dissociation of a single molecule, see Figure 9.9 for the model system, into an adsorbed hydroxyl group and hydrogen are between 45 kJ mol⁻¹ and 71 kJ mol⁻¹ depending on details of the method used. Studies with a three-layer slab, kept at a fixed geometry, employing ultrasoft-pseudopotentials and PW91 as the functional, calculated the reaction energies as 45 kJ mol⁻¹ and 68 kJ mol⁻¹, with energy cut-offs at 300 eV and 340 eV, respectively.^{250,254} The corresponding barriers were 66 kJ mol⁻¹ and 85 kJ mol⁻¹, respectively. When the top layer of the slab was allowed to relax, reaction energies of 50 kJ mol⁻¹ and 63 kJ mol⁻¹ as well as barriers of 72 kJ mol⁻¹ and 87 kJ mol⁻¹ were obtained with an energy cutoff of 400 eV with the PW91 functional and 340 eV with RPBE functional.^{253,255} When the energy cutoff is kept at 300 eV along with PW91 functional, but the surface is modeled as a four-layer slab, with the atoms of the top layer relaxed, the reaction energy increases to 58 kJ mol⁻¹ with a barrier of 74 kJ mol⁻¹.²⁵⁴ A PAW study employing two types of GGA functionals, PW91 and PBE, reported the highest barrier for the case of a single water molecule, adsorbed on a slab of four-layers with top two layers allowed to relax.¹⁶¹ For both functionals the barrier was calculated to be 93 kJ mol⁻¹ with reaction energies of 65 kJ mol⁻¹ and 68 kJ mol⁻¹ in the case of PW91 and PBE functional, respectively.

Table 9.3 The reaction energies and activation barriers of water splitting available in the literature. Computational details are also shown.

| Reference | Unit cell | Slab/ opt | Core | Cut-off | k-points | Functional | #H ₂ O | E _r ^a | E _a ^a |
|-----------|---------------------|-----------|-----------------|---------|----------|-------------|--------------------------|-----------------------------|-----------------------------|
| Ref. 250 | 2x2 3-layers, fixed | PP | 340 | 18 | PW91 | 1 | 68, 71 ^b (50) | 85 (72) | |
| Ref. 254 | 2x2 3-layers, fixed | PP | 300 | 4x4 | PW91 | 1 | 45 | 66 | 74 |
| | 4-layers, top | | | | | 58 | | | |
| Ref. 253 | 3x3 3-layers, top | PP | 400 | 3x3 | PW91 | 1 | 50, 60b | 72 | |
| Ref. 255 | 2x2 3-layers, top | PP | 340 | 4x4 | RPBE | 1 | 63 | 87 | |
| Ref. 161 | 3x3 4-layers, 2 top | PAW | 400 | 3x3 | PW91 | 1 | 65 | 93 | |
| | | | | | PBE | 1 | 68 | 93 | |
| | | | | | PW91 | 2 | 43 | 86 | |
| | | | | | PBE | 2 | 46 | 85 | |
| Ref. 256 | 2x2 4-layers, 2 top | PAW | 0.18 Åc | 4x4 | RPBE | 2 | (49), exp. (50) | | |
| | 3x3 | | | | | | | | |
| Ref. 211 | √3x3 3-layers, top | PP | DZ ^d | 5x3 | PBE | 4 | 12.5 | | |
| Ref. 212 | 3x3 6-layers, top | PP | 340 | 2x2 | RPBE | 12 | 68 (homo) | 130 | |
| | | | | | | 58 (hetero) | | | 95 |

^a Numbers in parentheses include ZPE corrections. ^b Infinite separation of the products. ^c Real space grid. ^d Gaussian type basis set

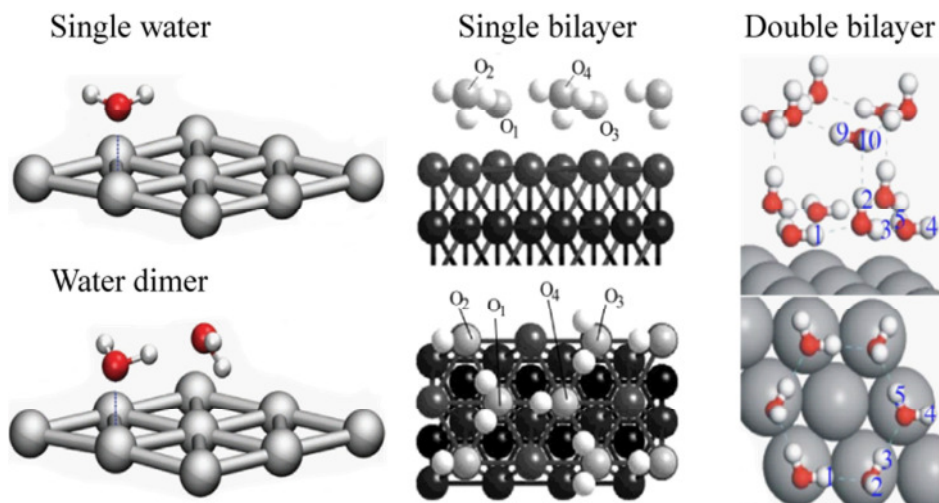


Figure 9.9 Several water models to investigate water splitting reaction. Adapted from Refs. 161 (right column), 211 (middle column), and 213 (left column).

Another PAW study calculated a ΔH value of 49 kJ mol^{-1} using a four-layer slab with two relaxed layers and two water molecules, employing an RPBE functional and a 0.18 \AA real grid-spacing.²⁵⁶ When two water molecules were arranged as a dimer as shown in Figure 9.9 the reaction energy was decreased by 22 kJ mol^{-1} , to 43 kJ mol^{-1} and 46 kJ mol^{-1} for PW91 and PBE functionals, respectively.¹⁶¹ The changes in the barriers, however, were only $\sim 7 \text{ kJ mol}^{-1}$. This shows that the reaction products H and OH, especially the latter, are stabilized by the presence of another water molecule on the surface.

In another study,²¹¹ a model of a water bilayer was placed on a three-layer slab surface with the atoms at the top layer relaxed in a $\sqrt{3}\times 3$ surface unit cell; the calculations were carried out with NC-pseudopotentials, a double zeta quality Gaussian type basis set, and the PBE functional. The water bilayer was composed of four water molecules as a saturated single overlayer. Half of the water molecules were oriented parallel to the surface, as this is the case for a single water molecule adsorbed, whereas the other half were oriented vertical to the surface. One of the H atoms in vertical oriented molecules interacts with the O atoms of the parallel oriented molecules forming a H-bonding network. The other H of a water molecule interacts with the surface Pt atom, Figure 9.9. Splitting of these latter H atoms from both molecules is a state, which is only 12.5 kJ mol^{-1} per water molecule less stable than the original water bilayer.

The double water bilayer was considered in another study.²¹³ This system was described by a slab model of six-layers (top layer relaxed), using PAW, 340 eV energy cut-off, and the RPBE functional. In this model, the H atoms of the lower bilayer do not orient

themselves towards the surface as in the single bilayer case, but point towards the second bilayer to enhance the H-bonding network of the water layer, Figure 9.9. This double bilayer is located at a longer vertical distance from the surface than the single bilayer. Water splitting was considered both heterolytically (a proton from adsorbed water shifts to the double bilayer, producing an adsorbed OH and a solvated proton) and homolytically (a hydrogen is separated from adsorbed water, forming a hydroxyl and a hydrogen atom adsorbed on the surface). The homolytic reaction goes over a barrier of 130 kJ mol^{-1} to a dissociated state 68 kJ mol^{-1} more endothermic whereas for the heterolytic pathway these values are 95 kJ mol^{-1} and 58 kJ mol^{-1} , respectively.

The studies presented so far inspected the water splitting reaction on or near the surface. One can also consider autoprotolysis of water, however modeling of the system is beyond the current computational possibilities as the reaction medium should consist of a proton per $\sim 10^9$ water molecules at neutral conditions.²⁵⁵ When one calculates the free energy difference of water splitting at room temperature from the dissociation constant, $pK_a = 14$, the value is 80 kJ mol^{-1} . However the dissociation constant decreases depending on the temperature until 250°C ,²⁵⁷ $pK_a = 11.2$, resulting in about two orders of higher concentrations of H^+ and OH^- ions at this temperature. An ab initio molecular dynamics study employing the Car-Parrinello method approached autoprotolysis of water with a kinetic energy consistent with room temperature.²⁵⁵ The specific connections of H-bonded substructures were formed and the energy differences were calculated with a separated proton from one water molecule, which is transferred along the water-chain. Barriers of $8\text{--}48 \text{ kJ mol}^{-1}$ were reported for water splitting.²⁵⁵ Hence OH groups might form in the solution and then be transferred and adsorbed on the Pt surface.

After summarizing the presented results about water splitting for both the situation on the surface and in the bulk water, one can estimate a reaction energy and barrier for the reaction to achieve OH groups adsorbed on the surface. The results presented depend on the amount of water molecules in the various models. As the model employed in this study does not employ additional water molecules for stabilization, a barrier of 90 kJ mol^{-1} will be taken for water splitting on Pt(111) as a cautious estimate. For the reaction energy, instead of assuming a value, a comparison between the energy of the coadsorbed structure of propionyl **1** + hydroxyl group **6** (along with a hydrogen atom adsorbed at infinite separation) and adsorbed propionyl **1** with a water molecule adsorbed at infinite separation was made. The resulting energies suggest the water splitting reaction energy to be 58 kJ mol^{-1} and 66 kJ mol^{-1} on the flat and stepped surfaces, respectively.

(d) $\mathbf{1} + \mathbf{6} \rightarrow \mathbf{7}$

When the reactants are brought together from “infinite separation” to a reactive distance that state is by 13 kJ mol^{-1} more stable. Recall that the (formally) “infinite” separation refers to the sum of their energies when they are adsorbed on the surfaces of two different unit cells ($E(\mathbf{1})/\text{M} + E(\mathbf{6})/\text{M}$), while otherwise both molecules are adsorbed within the same unit cell ($E(\mathbf{1+6})/\text{M}$). At the IS the distance between the C atom of the carbonyl moiety and the O atom of the OH group is 342 pm. At **TSd** (Figure 9.6) this distance shrinks to 194 pm, an interaction starts between the two molecules. The reaction energy is -46 kJ mol^{-1} and the activation barrier is 31 kJ mol^{-1} . The product propionic acid **7** binds weakly to the surface, as indicated by the low BE, 39 kJ mol^{-1} (Table 9.1), and discussed in detail in Section 9.1.7. Any C–C bond scission reaction of the intermediates formed from dehydrogenation of species **7** will be a decarboxylation reaction.

The active centers in this reaction are the CO moiety of **1** and **6** adsorbed on the surface, which are both bound to surface and in a very close interaction with the surface even before the reaction. As the aim to calculate the reactions on the stepped surface is to eliminate the geometric disadvantages, in this case there is no need to re-evaluate this reaction on the stepped surface. The values on the flat surface can be re-used for the reaction that occurs on the terrace of the stepped surface, where the geometrical effects would be most advantageous and similar to the flat surface Pt(111).

9.2.3. *Decarboxylation*

(e) $\mathbf{7} \rightarrow \mathbf{2} + \mathbf{8}$

The first decarboxylation reaction is the decomposition of propionic acid **7** formed via the energetically favorable insertion of hydroxyl **6** into propionyl **1**. The C–C bond, which is almost normal to the flat surface, see **7** Figure 9.2, is to be broken during this reaction. On the flat surface the α -C atom is far away, 519 pm, from the surface Pt atom it will interact with to break the bond and the vertical distance of this atom to the top crystal plane is 450 pm. The reaction is initiated by the molecule bending towards the surface so that the α -C starts interacting with the surface. At **TSe** (Figure 9.6) the C–C bond is elongated to 251 pm, whereas the C–Pt distance has shrunk to 295 pm; both key distances are remarkably long. As seen from Figure 9.6 the ethyl moiety **2** is still not interacting with the surface, the slight interaction is accomplished through a long C–Pt contact and a 213 pm H–Pt contact. The carboxyl group rearranges so that the C atom binds to the surface at a C–Pt of 199 pm, very close to its value in the stable adsorption mode. The reaction is thermoneutral with an energy

change of -5 kJ mol⁻¹. However, in order to break the C–C bond on the flat surface Pt(111), a barrier of 219 kJ mol⁻¹ has to be overcome.

On the stepped surface propionic acid **7** is adsorbed in such a fashion that the distance of the α -C to the Pt atom is by 78 pm shorter, 441 pm, than on the flat surface. The α -C starts to interact with the step-edge Pt atom of the upper terrace, the O atom migrates to bind with a Pt atom of the lower terrace and the C₁ atom starts an interaction with another lower terrace atom. In the **TSe'** structure the α -C–Pt has decreased to 305 pm, the C₁–Pt atom distance is 204 pm and the O–Pt distance is 225 pm, (cf. Figure 9.7). The C–C bond is elongated by 75 pm, from 151 pm at the IS to 226 pm at the TS. The C–C distance is 25 pm shorter than on the flat surface and the α -C–Pt distance is 10 pm longer. As there is no enhanced stabilization by the surface at the transition state, the activation barrier decreases only by 15 kJ mol⁻¹, to 204 kJ mol⁻¹, and the reaction energy is -14 kJ mol⁻¹.

(f) $7 \rightarrow 9 + H$

The hydroxyl H atom of species **7** is already oriented to the surface, H–Pt = 227 pm. The reaction starts by strengthening the interaction of these two atoms and **TSf** is reached when the H–Pt distance shrinks to 161 pm, O–H = 165 pm. As the O atom loses its H atom, it starts moving towards a surface Pt atom and at the TS the O–Pt distance reaches 318 pm. The reaction energy is -11 kJ mol⁻¹ and the barrier is only 44 kJ mol⁻¹, which makes the conversion favorable both thermodynamically and kinetically. Indeed experiments on the adsorption of propionic acid **7** on the Pt (111) surface in gas phase suggest carboxylate formation, which is detected in an EELS study by Avery²⁵⁸ and a helium atom scattering (HAS) study by Graham.²⁴⁷ Also on Pd(111) surfaces propionic acid **7** forms surface propionate as observed by TPD and indicated by HREELS.²⁵⁹

Also this reaction was not studied on the stepped (221) surface for the same reason as given in reaction **(d)**. In the energy profile of the stepped surface, the values for the flat surface are employed.

(g) $9 \rightarrow 2 + 10$

The α -C atom of species **9** is at a distance of at least 494 pm from a Pt atom and 417 pm from the surface. For this most stable adsorption mode of propionate no TS geometry could be located; the structures found as candidates for the TS do not meet the criteria set to confirm a plausible structure, i.e., the forces on the atoms are higher or there is more than one imaginary frequency. The structures that satisfy in part the criteria have activation barriers of ~300 kJ mol⁻¹. Such a structure, e.g., **TSg**, is depicted in Figure 9.6. An analysis of this

structure suggests that geometrical factors are the reasons underlying the high activation energy structures. The decomposing moieties at the flat surface do not have a contact with the surface, thus lack stabilization by the catalyst. The reactant molecule **9** is connected to the surface only via two O atoms, which would be part of the CO₂ **10** molecule when the decomposition is completed. As explained in Section 9.1.10, CO₂ adsorption on the surfaces of Pt is weak and CO₂ is located at a notable distance from the surface. As the reaction proceeds, the ethyl moiety that is pointing away from the surface in the IS, must approach and start to interact with the surface. However at the same time CO₂ also moves upwards and the molecule loses the stabilizing effects of the surface to a large extent. For the species **TSg** depicted in Figure 9.6 the distance of the CO₂ to the surface is ~265 pm, and the C atom of the ethyl moiety is 314 pm away from the surface. Lu et al.¹⁹⁰ explored the same decomposition on the Pd(111) surface but instead of employing the most stable bidentate form, they employed the monodentate form of **9**, which is 81 kJ mol⁻¹ less stable. Starting from that less stable species, they calculated the activation barrier to be 135 kJ mol⁻¹. Hence the effective barrier from the most stable species would be also very high, 216 kJ mol⁻¹.

This geometrical disadvantage can be overcome by the presence of a terrace of Pt atoms at a different height that will stabilize the species. For the species **9'** the α -C–Pt distance is 423 pm on the stepped surface; 71 pm shorter than on the flat surface. This difference in the distance is around the same value as in the case of **7** and **7'**. The reaction proceeds in a similar way as on the flat surface; the ethyl moiety approaches the surface Pt atom, but in this case an atom from the upper terrace is involved. The interaction of CO₂ with the surface also decreases during the reaction. However, even in the structure **TSg'** shown in Figure 9.7, the CO₂ moiety is still connected to the surface through one of its O atoms, O–Pt = 232 pm. The C–Pt distance drops to 230 pm; the ethyl moiety is significantly closer to the surface at the TS. Hence both moieties that end up as the products are stabilized by the surface at the TS structure, decreasing the activation barrier of the reaction, $E_a(\mathbf{g}') = 142$ kJ mol⁻¹. Even though the barrier is drastically lower than $E_a(\mathbf{g})$, this conversion is still a seldom event considering the experimental conditions.²⁵

(h) $\mathbf{7} \rightarrow \mathbf{II} + \mathbf{H}$

One may consider dehydrogenation of the species **7** at the α -C instead of the hydroxyl group prior to C–C bond scission. Thus one can benefit from the fact that C–C bond scission is normally less demanding when the ligand is more or less free of H and dehydrogenation barriers are generally lower when the ligand is still “rich” in H.²² Dehydrogenation of **7** will

also bind the α -C to the surface; the previously discussed high barriers in reactions (**e**) and (**g**) might be due to a large C–Pt separation, C–Pt > 500 pm, in the IS structures. The initial H–Pt distance is 478 pm and it decreases to 168 pm at **TSh**, Figure 9.6. For this interaction to occur, the molecule bends towards the surface, reaching almost a structure parallel to the surface at the **TSh** with α -C–Pt = 232 pm, close to the final state of the reaction. At **TSh** the C–H bond elongates to 154 pm. The activation barrier is 118 kJ mol⁻¹, indeed lower than that of direct C–C bond scission, $E_a(\mathbf{e})= 219$ kJ mol⁻¹, see Table 9.2, but quite high for a dehydrogenation reaction. The reaction is slightly endothermic with an energy change of 27 kJ mol⁻¹.

On the stepped surface the H atom to be separated is 93 pm closer to the Pt atom, H–Pt = 385 pm at IS. As the reaction proceeds this distance shrinks, α -C starts interacting with the same Pt atom as hydrogen and the TS occurs when the C–H bond elongates to 152 pm, see **TSh'** in Figure 9.7. At this geometry, the H–Pt bond is 161 pm and the C–Pt bond distance is reduced to 235 pm. On the stepped surface the activation barrier decreases significantly, by 72 kJ mol⁻¹, to 57 kJ mol⁻¹ and the reaction energy is 2 kJ mol⁻¹; thus one has an almost thermoneutral reaction.

(i) **11 → 5 + 8**

On the flat surface $\eta^2(\text{C},\text{O})$ adsorbed **11** undergoes a C–C bond scission to form ethylidene **5** bonded through the α -C atom of **11** and a COOH group **8** bonded through C₁ and the carbonyl O of **11**. The C₁ atom starts interacting with the surface when the species **11** bends towards the surface. The **TSi** occurs when the C–C bond elongates to 211 pm. The C of the carboxyl moiety, C₁, is bonded to a Pt atom at 205 pm, also the O–Pt bond remains intact; it is elongated by only 2 pm. It seems that the carboxyl moiety has reached the FS configuration, but the α -C of **5** is still bonded atop a single Pt atom with a C–Pt of 197 pm instead of the FS configuration, where this moiety is located at a bridge site. The activation barrier is lower than the previously discussed decarboxylation reactions on the flat surface, 108 kJ mol⁻¹ and the reaction is exothermic by 42 kJ mol⁻¹.

The initial state of the abstraction of the carboxyl group **8** on the stepped surface is not the one calculated as the most stable on that surface and described in Section 9.1.11, **11'** shown in Figure 9.3. Figure 9.10 shows the **ISi'** of the C–C scission reaction. As can be seen by comparing with the most stable adsorption structure, the binding mode is still $\eta^2(\text{C},\text{O})$, but the O atom is now that of the OH group and the molecule binds at the step-edge at two Pt atoms. The BE of this mode is 14 kJ mol⁻¹ lower than that of the most stable adsorption mode.

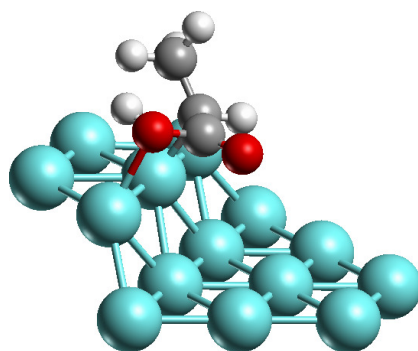


Figure 9.10 Initial state (IS) structure for **i'**.

During the migration process from the most stable adsorption state of **11'** shown in Figure 9.3 to the initial state of reaction (**i'**) shown in Figure 9.10, the molecule passes over a barrier, $E_a(\text{mig}') = 28 \text{ kJ mol}^{-1}$. The low value of this TS, **TSmig'**, makes the **ISi'** a metastable intermediate mode. In the structure **ISi'** the O–Pt bond is long, 237 pm and the C–Pt bond is 212 pm, 3 pm shorter than the corresponding bond in the most stable mode **11'**. The molecule starts to move from this adsorbed mode over the step-edge so that the α -C starts interacting with the Pt atom that O was bound to at the IS. At the same time the C atom of the carboxyl group also interacts with the same Pt atom and the OH moiety lifts from the surface, removing the O atom from the surface, O–Pt = 296 pm at **TSi'**. The α C is almost at a bridge site where α -C–C₁ = 180 pm. This reaction is essentially thermoneutral, $E_r(\text{i}') = 5 \text{ kJ mol}^{-1}$, over a barrier of $E_a(\text{i}') = 96 \text{ kJ mol}^{-1}$. Recall that this energy is with respect to a structure that is a metastable intermediate, **ISi'**. With respect to the stable intermediate **11'**, the effective reaction energy is $E_r^{\text{eff}}(\text{i}') = 18 \text{ kJ mol}^{-1}$ and the effective activation barrier is $E_a^{\text{eff}}(\text{i}') = 110 \text{ kJ mol}^{-1}$. Energetically the steps do not provide an advantage for this reaction. This conclusion can be corroborated by inspecting the geometry of the initial and final states; in spite of the fact that steps contribute actively in the C–C bond scission, they do not offer a reaction partner at the required height to the adsorbate. Hence the bond breaking takes place in the same fashion as it does on the flat (111) surface.

(j) **9 → 12 + H**

Following the same logic that prompted the calculation of the dehydrogenation of **7**, the dehydrogenation of the α -C of **9** was also inspected. The H–Pt distance at the IS is 491 pm, with the H center being 452 pm away from the surface. The TS structure, **TSj** in Figure 9.6, resembles very much **TSh**, with H–Pt 168 pm and 227 pm. The C–H distance is elongated to 153 pm in the TS. In order to form an interaction between the α -C and the surface, the C–Pt distance shrinks to 242 pm at **TSj**. The reaction is highly endothermic, 67

kJ mol^{-1} . The activation barrier is also the highest determined among the dehydrogenation reactions in this study, 142 kJ mol^{-1} . However considering that for C–C bond scission of this species no transition state lower than 300 kJ mol^{-1} is determined, dehydrogenation is favored over decomposition on the flat surface.

On the stepped surface the H atom to be extracted from **9'** is much closer to the Pt atom it gets into interaction, with $\text{H–Pt} = 392 \text{ pm}$; compare the situation in **7'**. Thus the reaction (**j'**) proceeds similarly as the reaction (**h'**). At the **TSj'** the H atom is at the top of the step-edge atom and the α -C is also bound to the same step-edge metal atom. The H–Pt distance drops to 160 pm whereas the C–Pt bond is 230 pm , shortening by almost 100 pm from its initial length. The C–H distance is elongated to 156 pm at **TSj'**, see Figure 9.7. Also one of the O atoms binds to the neighboring step-edge Pt atom, with $\text{O–Pt} = 218 \text{ pm}$ at the TS. The other O–Pt bond is elongated by 5 pm and at the TS it is also 218 pm . This bond eventually breaks completely to reach the geometry of **12'** in the FS. The reaction on the stepped surface is still endothermic, 31 kJ mol^{-1} , but its reaction energy has reduced radically. The barrier reduces to 83 kJ mol^{-1} , making dehydrogenation achievable.

(k) $\mathbf{11} \rightarrow \mathbf{12} + \mathbf{H}$

In a similar fashion as **7** is dehydrogenated to **9** via reaction (**f**), the α -dehydrogenated species **11** dehydrogenates to **12** via reaction (**k**). The OH group from which the H atom shall be extracted lies high above the surface in **11**. As the molecule bends towards the surface, the H atom relocates itself so that it can start to interact with the surface Pt atom. At the TS the O–H bond elongates to 150 pm and the H–Pt shrinks to 166 pm , which is depicted as **TSk** in Figure 9.6. The O of the hydroxyl group is also close to that surface Pt atom, $\text{O–Pt} 303 \text{ pm}$, that it will be bound to in the FS at $\sim 213 \text{ pm}$. The dehydrogenation reaction is mildly endothermic, with a reaction energy of 18 kJ mol^{-1} , and it proceeds over a low barrier of 50 kJ mol^{-1} . Such a low barrier of a mildly endothermic reaction increases the probability of the reverse reaction; the hydrogenation of **12** to **11**. The barrier will be much lower, 32 kJ mol^{-1} and the reaction product **11** will be energetically more stable than the combination of the reactants, **12** and H, coadsorbed on the surface. One should take this into account when considering the most probable pathway and also take into account the reaction will occur probably in both directions; see Section 9.3.4.

As the reaction (**k**) is already facile on the flat surface and no advantage can be foreseen on the stepped surface the same energetics can be employed on the stepped surface, assuming it takes place on a sufficiently wide terrace of the stepped Pt surface.

(m) $\text{I2} \rightarrow \text{5 + 10}$

The last reaction considered in this network is the C–C bond scission of **12**. Already in the IS, both products of the reaction are in contact with the surface; the ethylidene moiety via the α -C of **12** and CO_2 via both O atoms of **12**. The reaction proceeds as the groups start separating from each other and the TS is reached when the C–C distance has elongated to 210 pm (from 148 pm at the IS, see **TSm** in Figure 9.6). One of the O atoms has already lost contact to the surface Pt atom; in the TS structure, O–Pt is elongated by 161 pm, to 373 pm, while the other O–Pt bond is elongated to 232 pm. The α -C–Pt bond shrinks by 23 pm to 197 pm. It is also seen that the O–C–O angle increases from 122° at the IS to 147° . The reaction is exothermic, -43 kJ mol^{-1} , over an activation barrier of 119 kJ mol^{-1} . These values are very close to those of the decarboxylation (**i**); the CO_2 molecule loses its contact to the surface again too early in the reaction to be stabilized at the TS of C–C bond breaking.

On the stepped surface C_1 and C_2 centers of **12'**, the atoms that prospective products of (**m'**) interact with the surface, are already in contact with the step-edge of the (221) surface in the TS. At **TSm'** the structure still resembles the IS; the CO_2 moiety starts moving into the vacuum, Figure 9.7. The C–C distance is elongated to 210 pm, from 152 at the IS, the O–Pt distance is extended by 19 pm, and the α -C–Pt has shrunk by 14 pm, to 195 pm. Additionally, the carboxylic C interacts with the step-edge Pt atom, albeit via a long distance, 293 pm. As on the flat surface, the O–C–O angle increases to 146° . After the TS, species **5'** moves to the bridge site on the step-edge and CO_2 **10'** moves away from the surface. This final state structure is 41 kJ mol^{-1} more stable than the reactant **12'** (Table 9.2), similar to the case on the flat surface. The effect of the steps is a reduction of the activation energy by 33 kJ mol^{-1} ; the barrier decreases to 86 kJ mol^{-1} on the stepped surface.

9.3. Overview over the reaction pathways

After 1-propanol was dehydrogenated to its most stable intermediate propionyl on the (111) surface, the discussion now turns to possible conversion reactions to form ultimately the experimentally observed^{25,178} products CO_2 and ethane. This discussion addresses transformations on both the flat Pt(111) surface and the stepped Pt(221) surface, focusing on the C–C scission reactions. Out of a total of 12 reactions, six are C–C bond scissions, of which two are decarbonylation reactions and four are decarboxylation reactions. Five dehydrogenation reactions from O/C and one hydroxyl group insertion are also included in the network (Figure 9.1) to obtain different routes. The products of the C–C bond scission reactions investigated here are ethyl or ethylidene, both of which are further hydrogenated

into ethane and CO, COOH or CO₂, the first and second to be converted into the third via WGS as explained in Section 9.2. In this section the most probable conversions for the adsorbate will be visited, based on the energetics that has previously been presented. Figure 9.11 depicts the most favorable conversions, including the WGS reaction to convert CO into CO₂ and the water splitting (WS) reaction to provide OH groups adsorbed on the surface. The reaction energies, E_r^{inf} , at (formally) infinite separation of the products, in the case of reaction (d) the reaction energy at (formally) infinite separation of the reactants, are employed in this figure; for the corresponding numerical values, see Table 9.2.

9.3.1. *Decarbonylation route on the flat (111) surface*

The C–C bond scission to produce CO **3** adsorbed on the surface occurs through two stable intermediates on the surface, **1** and its α -C dehydrogenated form **4**. The decarbonylation of **1** via reaction (a) has to go over a barrier of 143 kJ mol⁻¹ whereas the dehydrogenation process (b) over $E_a(b) = 91$ kJ mol⁻¹ is almost thermally neutral, 4 kJ mol⁻¹. Hence, dehydrogenation is the more probable conversion of **1**. This dehydrogenation reaction can also easily be reversed in view of its thermoneutrality; both molecules are strongly bound on the surface. Their conversion into each other via dehydrogenation/hydrogenation should be in equilibrium. The C–C bond scission of the dehydrogenated species via reaction (c) proceeds over a barrier of the same height as that of dehydrogenation. This decarbonylation route is shown Figure 9.11a, represented by a dashed line; the feasible CO production from propionyl **1** produces ethylidene **5** as the hydrocarbon and the overall conversion energy is -41 kJ mol⁻¹, over an effective barrier of 91 kJ mol⁻¹. CO is further converted into CO₂ over the barrier of the rate-determining step (RDS) of WGS and finally ethylidene is coadsorbed with CO₂. The energetics is included from a study of the WGS reaction network where the most favorable pathway was found to be via a COOH intermediate.²⁵⁰

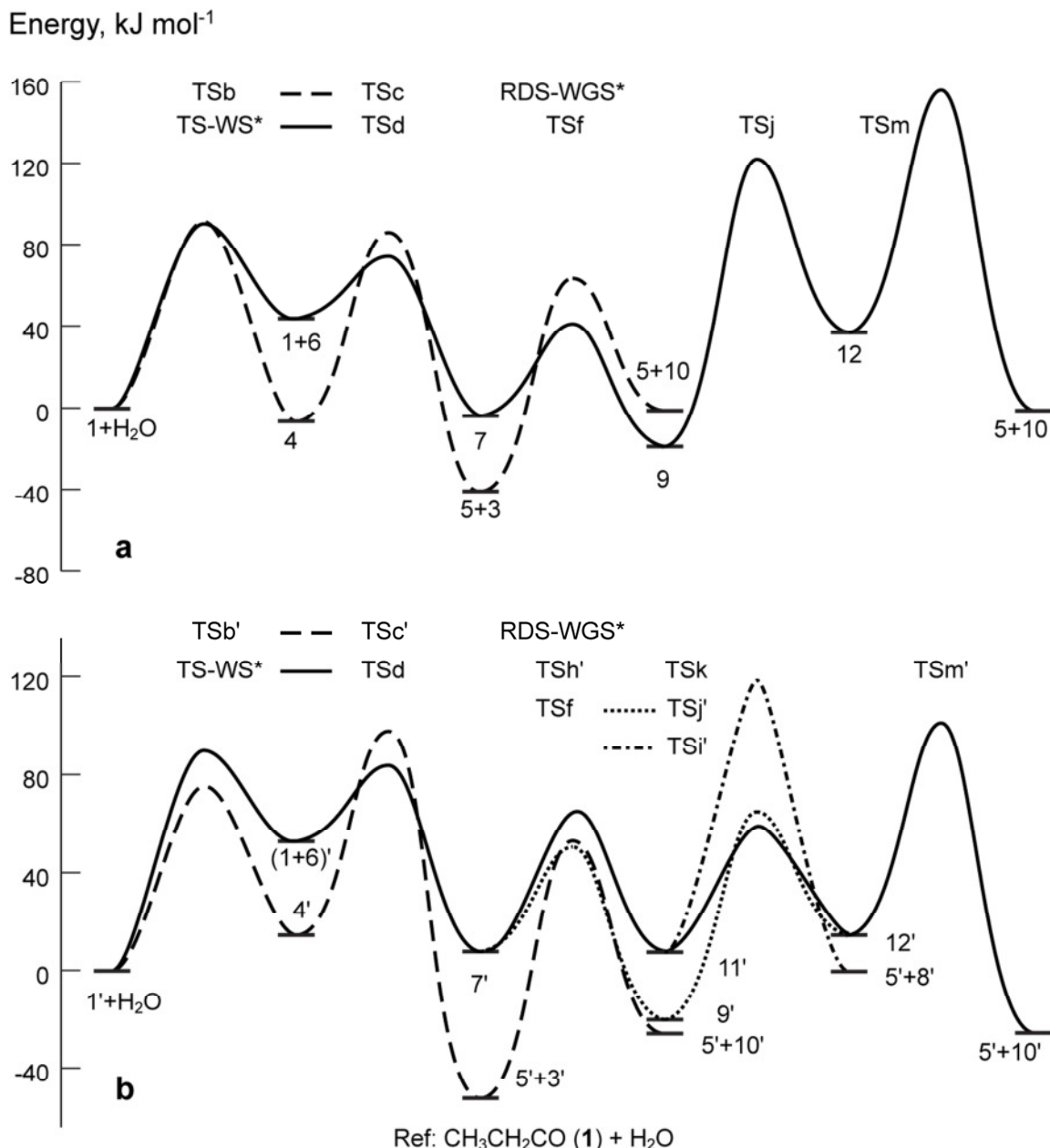


Figure 9.11 The competing decarbonylation (dashed lines) vs. decarboxylation pathways (solid lines) along with two alternative pathways (dotted and dot-dashed lines) for C-C scission on (a) a flat and (b) a stepped surface. H_2O , when not contributing to the reaction, is assumed to be co-adsorbed at (formally) infinite separation along with excess H atoms. Energies are relative to a system where propionyl **1** and H_2O are adsorbed at infinite separation. The barrier of the rate-determining step of the WGS reaction is included (Table 9.2). The migration step (**mig'**) preceding the reaction (**i**) is left out; the E_r^{inf} as listed in Table 9.2 are used.

For the starting molecule propionyl **1** the insertion of an OH group is studied apart from the conversion that would lead to decarbonylation. The possibility of OH groups forming on the surface has been presented earlier in the text; in Section 9.2.2, a barrier of 90 kJ mol⁻¹ is estimated for the WS barrier, and the reaction energy is 56 kJ mol⁻¹. The adsorbed OH groups are very reactive on the surface.²⁰¹ The barrier for diffusion and rotation about the surface normal for OH groups is low, 11 kJ mol⁻¹ and 5 kJ mol⁻¹, respectively, at coverages from 1/9 to 1/3.²⁴³ Therefore they can easily migrate to the vicinity of the propionyl groups. The interaction between the two species is already favorable when they are only coadsorbed on the surface; see the difference in the reaction energies when at close proximity, E_r , and at formally infinite separation, E_r^{inf} , is 13 kJ mol⁻¹ in Table 9.2. The addition of OH **6** to propionyl **1** produces propionic acid **7** over a low barrier $E_a(\mathbf{d}) = 31$ kJ mol⁻¹ and releases 46 kJ mol⁻¹. The products of the favorable decarbonylation route, **5** + **3**, lie 38 kJ mol⁻¹ lower in energy than propionic acid, **7**.

9.3.2. Decarboxylation route on the flat (111) surface

Formation of propionic acid by OH insertion into propionyl opens up the reaction network for decarboxylation reactions. Propionic acid itself is weakly adsorbed on the surface, BE = 39 kJ mol⁻¹, in agreement with the experiments in aqueous phase that report such species to be present in the product stream.^{25,178} On the flat surface dehydrogenation into propionate **9** via reaction (**f**) is also possible; the reaction is 11 kJ mol⁻¹ exothermic and its barrier $E_a(\mathbf{f}) = 44$ kJ mol⁻¹ is slightly higher than the desorption energy. This conversion is also supported by the findings of LEED studies conducted in the temperature range 100 – 300 K.²⁶⁰ Firment and Somorjai observed no ordered structure upon propionic acid adsorbed on clean Pt(111) surface and claimed that dissociative adsorption is the underlying reason.²⁶⁰ Avery's EELS study²⁵⁸ and Graham's HAS²⁴⁷ findings also indicate this dissociation, as presented in reaction (**f**). The barrier for dehydrogenation of propionic acid at the α -C, $E_a(\mathbf{h})$, is almost three times as much as that of $E_a(\mathbf{f})$ hence it is not shown in Figure 9.11a. The C–C bond scission of propionate **9** via (**g**) on the flat surface is also energetically not favorable; a barrier of ~300 kJ mol⁻¹ blocks this conversion. The dehydrogenation at the α -C is the preferred conversion of **9**; however $E_a(\mathbf{j})$ is also high, 142 kJ mol⁻¹, and the product **12** lies 67 kJ mol⁻¹ higher in energy, making the reverse reaction kinetically better accessible. The decarboxylation route, the solid line in Figure 9.11a, reaches an end with the C–C bond cleavage of **12**, $E_a(\mathbf{m}) = 119$ kJ mol⁻¹, producing CO₂ **10** and ethyldene **5**. The overall effective barrier height for decarboxylation is 156 kJ mol⁻¹ on the (111) surface, and the rate determining step is the final C-C scission reaction, reaction (**m**).

9.3.3. Decarbonylation route on the stepped (221) surface

The energy profile of the most likely pathways for conversions on the stepped surface is given in Figure 9.11b. Both dehydrogenation and decomposition reactions occur easier on the stepped surface and the differences in the heights of **TSa'** and **TSb'** decreases to 31 kJ mol⁻¹ from 43 kJ mol⁻¹ on the flat surface as the C–C bond scission barrier decreases by 28 kJ mol⁻¹ compared to a 16 kJ mol⁻¹ decrease in the dehydrogenation barrier. The barrier for the C–C scission of **4'** also decreases, but only slightly, by 8 kJ mol⁻¹. Hence on the stepped surface the preferred decarbonylation is again the combined reaction (**b'**) and (**c'**) with an effective reaction energy of -52 kJ mol⁻¹, $E_r^{inf}(\mathbf{b}') + E_r^{inf}(\mathbf{c}')$, over an effective barrier of 98 kJ mol⁻¹, the C–C bond scission of **4'** via reaction (**c'**). The following WGS reaction does not change the rate determining step of this decarbonylation pathway, as can be seen from the dashed line in Figure 9.11b, even though the effective barrier of WGS is 104 kJ mol⁻¹.

Water dissociation on stepped surfaces of Pt has not been studied as extensively as on flat surfaces. The presence of surface defects might increase the reactivity of Pt and lower the barrier and reaction energy of this process. However as there is no conclusive data about the reaction, the value estimated for the barrier at the flat surface, E_a (WS) = 90 kJ mol⁻¹, is also employed on the stepped surface. Coadsorbed **1'** and **6'** lie 53 kJ mol⁻¹ above the reference state of **1'** adsorbed with H₂O at a formally infinite separation. The following OH insertion into propionyl proceeds with a low barrier and the reaction geometry is so that the presence of a terrace at a different height will not stabilize the TS of that reaction. Hence the barrier and the reaction energy at the flat surface are employed, which is valid for the sufficiently wide terraces of the stepped surface. With these two assumptions, the water splitting barrier estimated on the flat surface applies to the stepped surface and the OH insertion occurs on the terraces of the stepped surface. The rate-determining steps of this route and of decarbonylation exhibit very similar activation barriers, as can be seen by comparing the solid and dashed lines Figure 9.11b. The difference in the effective barrier is only 8 kJ mol⁻¹ in favor of propionic acid **7'** formation. However the decarbonylation products **5' + 3'** are energetically more stable.

9.3.4. Decarboxylation route on the stepped (221) surface

The activation barriers of the reactions in the decarboxylation part of the network are affected a lot by the presence of surface defects. The conversions (**g**), (**h**), (**j**) and (**m**) all occur over lower barriers on the stepped surface. As explained earlier, the transition state structures are stabilized when they occur between two terraces of the stepped surface. Yet, for

the same reason as for OH insertion (**d**), the dehydrogenation of propionic acid **7** to propionate **9** via reaction (**f**) as well as 1-carboxy-ethyl **11** dehydrogenation to 1,1-propendiolate **12** via reaction (**k**), both from the hydroxyl O that is close to the surface, are not explicitly considered on steps.

Starting from propionic acid **7'** both decomposition barriers, $E_a(\mathbf{e}')$, and the α -H dehydrogenation barrier, $E_a(\mathbf{h}')$, decrease on stepped surfaces; however the decrease in the dehydrogenation barrier is much more pronounced, from 129 kJ mol⁻¹ on the flat surface to 57 kJ mol⁻¹ in the presence of the steps whereas the decomposition barrier drops only by 15 kJ mol⁻¹. As has been discussed in the description of this reaction in Section 9.2.3, the advantage of steps by stabilizing the molecule further at the transition state decreases the energy required to activate this transition. The reaction of O–H bond scission (**f**) is still the most favorable conversion for the species **7'** although not explicitly calculated on the stepped surface. The product of the most favorable conversion (**f**), **9'**, is also energetically more stable than the product of (**h'**), **11'**. However, there is no clear choice between the two reactions; both will occur to an extent.

When the conversion of the product **9'** is considered as the next step, the direct decomposition (**g'**) is also compared as an acceptable **TSg'** is obtained from the calculations. However the barrier is still high, $E_a(\mathbf{g}')$ = 142 kJ mol⁻¹, suggesting that **9'** will not be directly decomposed into **2'** and **10'**, when the competing conversion is α -H dehydrogenation with $E_a(\mathbf{j}')$ = 85 kJ mol⁻¹. The barrier of this dehydrogenation reaction producing **12** and H on the surface is also notably decreased, by ~60 kJ mol⁻¹, by the presence of steps.

For the species **11'** the direct scission of the C–C bond (**i'**) is explicitly considered on the stepped surface, starting from an adsorbate **ISi** on the surface that is 14 kJ mol⁻¹ less stable than **11'**. For the hydroxylic H dissociation (**k**), the values obtained for the flat surface are taken. Although the C–C bond cleavage on the stepped surface decreases the barrier of the individual step, there is no difference between the effective barriers of (**i**) and (**i'**). Hence also on the stepped surface the preference towards (**k**) is higher.

The only reaction remaining on the decarboxylation pathway is the decomposition of **12** to produce **5** and **10** on the surface, reaction (**m'**). The steps also decrease $E_a(\mathbf{m}')$ to 86 kJ mol⁻¹ via stabilizing **TSm'** on the Pt surface making the decarboxylation a competing C–C bond scission alternative to decarbonylation.

Having compared the possible conversions of the intermediates in the decarboxylation network, one can say that there is no clear choice for an optimal route. Any one of the three

routes represented by the solid line, the dashed-dotted line or the dotted line might be the preferred route to decarboxylate. The inter-conversion barriers of the species **7'**, **9'**, **11'**, and **12'** are uniformly low, represented by forward barriers E_a^{for} and reverse barriers E_a^{rev} in Figure 9.12. It is also remarkable that the barriers for the C–C bond scission reactions involving a fully saturated α -C, (**e'**) and (**g'**), are not sufficiently low to be the preferred route.

Hence one of the two C–C bond scission reactions, (**i'**) and (**m'**), should be the reaction to cleave the C–C bond. In order to assess the relative importance and selectivity of the two decarbonylation channels, a rough estimate on the rates of (**i'**) and (**m'**) is required. For that purpose a simplified reaction network is employed, Figure 9.12, and microkinetic modeling is applied to this network.

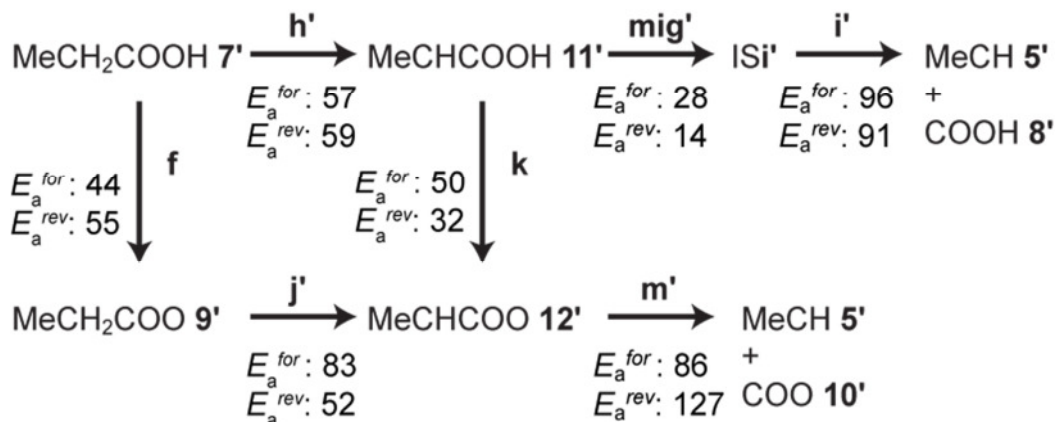


Figure 9.12 The reactions considered in determining the selectivity along the decarboxylation pathway. The forward and reverse activation barriers, E_a^{for} and E_a^{rev} , respectively, are given in kJ mol^{-1} .

In this reaction network one can assume that species **7'**, **9'**, **11'**, and **12'** are in equilibrium at the temperatures of the reactions, 473–523 K.^{25,178} The network also includes the migration step that converts the most stable adsorbate of **11'** that is obtained from dehydrogenating **7'** into **ISi'** over a barrier of 28 kJ mol⁻¹. Therefore this species should also be in equilibrium with **11'**.

When one analyses the simplified reaction network along with the forward and reverse barriers as given in Figure 9.12, it turns out that the C–C bond scission reactions (**i'**) and (**m'**) are reached via similar routes. Starting from **11'** there is a step with a low barrier that forms a metastable species that can react back to **11'** or undergo C–C bond scission, see Figure 9.13. On Route 1, species **11'** migrates to **ISi'** that is 14 kJ mol⁻¹ less stable over a low barrier, $E_a(\text{mig}') = 28 \text{ kJ mol}^{-1}$. When **ISi'** is formed the C–C bond scission goes over a barrier of 96

kJ mol^{-1} . The alternative Route 2 also starts from **11'**, proceeds via **TSk** that is 50 kJ mol^{-1} high to intermediate **12'** that lies 11 kJ mol^{-1} higher than **11'**, see E_r^{inf} in Table 9.2. The C–C bond scission of **12'** occurs over a barrier of 86 kJ mol^{-1} . On these two routes, intermediates **ISi'** and **12'** are accepted as metastable intermediates which enables one to calculate the rates from the composite properties of two consecutive reaction steps. In the search for a rate-limiting step, it is common to take the elementary step which has the highest barrier relative to its immediate reactants.²⁶¹ However in cases where there are metastable intermediates, as in the present case, this approach is not always correct.^{261,262} When the metastable intermediate is able to react back to the immediate reactant, one does not calculate the barrier of the rate determining step with respect to the energy of the metastable intermediate, but rather with respect to the preceding stable intermediate. This procedure yields an effective barrier, E_a^{eff} . For the routes under consideration, these values would be $E_a^{\text{eff}}(1) = E_r^{\text{inf}}(\mathbf{mig}') + E_a(\mathbf{i}') = (14+96) = 110 \text{ kJ mol}^{-1}$ and $E_a^{\text{eff}}(2) = E_r^{\text{inf}}(\mathbf{k}) + E_a(\mathbf{m}') = (11+86) = 97 \text{ kJ mol}^{-1}$. A justification of this approach is provided in Appendix A.

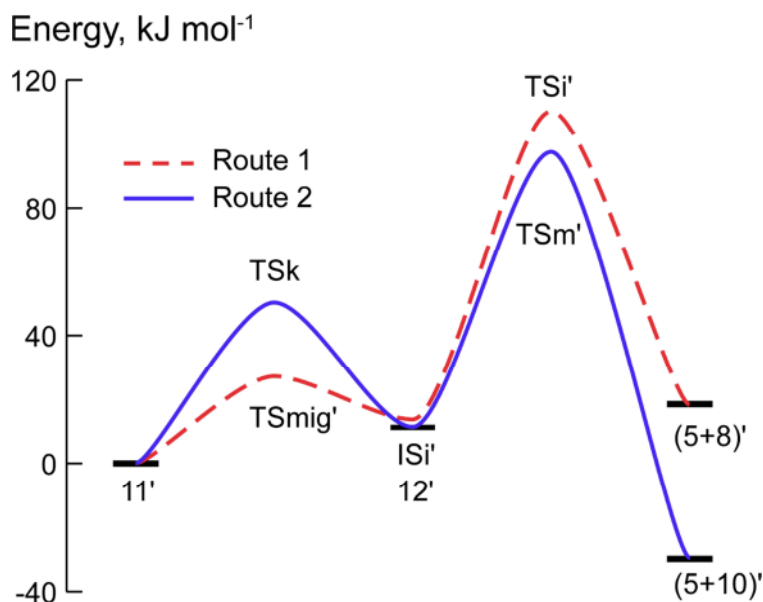


Figure 9.13 The energy profiles of C–C bond breaking steps for two routes of decarboxylation on the stepped surface Pt(221). Energies are relative to species **11'**.

The selectivity between the two C–C bond scission reactions is calculated as the ratio of the rates of these two routes.

$$\frac{r_1}{r_2} = \left(\frac{k_{\text{mig}} k_i}{k_{-\text{mig}}} \theta_{\mathbf{11}[*]} \right) \left(\frac{k_k k_m}{k_{-k}} \theta_{\mathbf{11}[*]} \right) = \frac{k^{\text{eff}}(1)}{k^{\text{eff}}(2)} \quad (9.1)$$

where r_q ($q = 1, 2$) is the rate of Route q , k_{rxn} is the rate constant of the elementary reaction step rxn , θ_x is the surface coverage of species x and $[*]$ is the number of available surface sites. In Appendix A the derivation of the effective rate constants k^{eff} is given. Hence by substituting the constants in Eq. (9.1) with those of Eqs. (A.6), (A.7), and (A.8) one obtains for the selectivity:

$$\frac{r_1}{r_2} = \exp\left(\frac{\Delta S^{0\ddagger eff}(1) - \Delta S^{0\ddagger eff}(2)}{R} + \frac{E_a^{eff}(2) - E_a^{eff}(1)}{RT}\right) \quad (9.2)$$

For the Routes 1 and 2 the initial state is the same species **11'**. As the effective entropy difference $\Delta S^{0\ddagger eff}$ is calculated relative to the initial stable species as given in Eq. (A.8), the first term in the exponential part of Eq.(9.2) is only determined by the entropies of the two rate-determining transition state structures of these routes, **TSi'** for Route 1 and **TSm'** for Route 2. These two species differ only by an H atom which is located at the hydroxyl group of **TSi'**, the frustrated translational and frustrated rotational modes can be taken to be similar for both species. Thus the variation of the effective entropy differences of Route 1 and Route 2 can be approximated by the difference of the vibrational contributions to entropy at the transition state structures, including the vibrational modes of an H atom adsorbed at a surface fcc site for the transition state structure in the Route 2:

$$\Delta S^{0\ddagger eff}(1) - \Delta S^{0\ddagger eff}(2) \approx S_{vib}(\mathbf{TSi}') - S_{vib}(\mathbf{TSm}') - S_{vib}(\text{H}) \quad (9.3)$$

The vibrational modes of the relevant species are supplied in Table 9.4. With the values reported in Table 9.4, one calculates the selectivity as defined in Eq.(9.2) at $T = 473$ K as $r_1/r_2 \approx 0.01$. Increasing the temperature to 523 K is in favor of Route 1, but the selectivity does not change significantly, $r_1/r_2 \approx 0.02$. Considering the approximations made during calculating this selectivity and the fact that the calculated reaction barriers and vibrational frequencies may not be of comparable accuracy, this value should not be regarded as a quantitative measure. However it enables one to estimate the second route, which is the combination of the dehydrogenation (**k**) and the decarboxylation (**m'**) would be favored over the migration (**mig'**) followed by decarboxylation (**i'**).

Table 9.4 Vibrational frequencies (cm^{-1}) of the initial states and the transition states, calculated vibrational contributions to entropy ($\text{J}\cdot\text{mol}^{-1}\cdot\text{K}^{-1}$).

| Structure | Vibrational frequencies | S_{vib} |
|-------------|--|-----------|
| TSi' | 3613, 3044, 3024, 2990, 2950, 1671, 1436, 1423, 1355, 1200, 1199, 1055, 1014, 980, 932, 887, 629, 565, 456, 412, 354, 274, 229, 198, 181 | 91 |
| TSk' | 3065, 3006, 2987, 2934, 1939, 1418, 1405, 1328, 1234, 1155, 1067 948, 913, 811, 582, 561, 501, 293, 254, 215, 194, 178 | 86 |
| H' | 1173, 553, 363 | 14 |

9.3.5. Effect of water dissociation energies on the preferred pathways

The favorable decarbonylation and decarboxylation pathways have been discussed in the previous sections, separately on each surface. On the flat Pt surface the decarbonylation pathway that forms CO first to be converted into CO_2 afterwards goes over an effective barrier of 91 kJ mol^{-1} whereas the decarboxylation pathway goes over an effective barrier of 156 kJ mol^{-1} . However both pathways depend on the values of the reaction and activation energies of water splitting. In the decarbonylation pathway, water splitting occurs within the WGS mechanism and the values found by Grabow et al. have been employed here, $E_r(\text{WS}) = 68 \text{ kJ mol}^{-1}$ and $E_a(\text{WS}) = 85 \text{ kJ mol}^{-1}$.²⁵⁰ The barrier is close to the estimated earlier water splitting barrier, $E_a(\text{WS}) = 90 \text{ kJ mol}^{-1}$, and the reaction energy is 10 kJ mol^{-1} higher than that used in the formation of OH for the decarboxylation pathway. The values from Grabow et al.'s work²⁵⁰ are employed to keep the values within the WGS conversion consistent. In the decarbonylation the water splitting occurs at the end of the pathway, following the exothermic C–C bond cleavage step, whereas in the decarboxylation pathway it is the first conversion, setting a new “reference energy level” for the conversions that follow.

As discussed extensively in Section 9.2.2, there is a wide range of energies reported in the literature depending on the water model used. The presence of additional water molecules stabilizes the fragments of the dissociation reaction through a H-bonding network, and the stabilization is different in each model. The reaction energy presented in this work does not take into account such a stabilizing effect due to a water network, it was calculated from the relative energy of IS **1 + 6** with respect to species **1**, with water adsorbed at (formally) infinite separation. Assuming that the water environment stabilizes in similar way all fragments along the remaining pathway, the position of the IS **1 + 6** on the energy scale induces a uniform

shift (of that part) of the reaction profile when the reaction energy of water dissociation changes. In other words, each energy level for the reactions that follow will be shifted by the same amount. Such a shift in positions of the energy levels influences the rate determining barriers of the decarbonylation vs. decarboxylation pathways.

The rate determining barrier of decarbonylation occurs prior to the estimated energies on both surfaces. For decarboxylation to be preferred – or at least to be competitive – on the flat surface, the effective barrier should at least be equal to that of decarbonylation. The effective barrier of decarboxylation is calculated by the summation of the reaction energies at infinite separation prior to the rate determining step plus the activation barrier of the rate determining step;

$$\begin{aligned} E_a^{\text{eff}}(\text{decarboxylation}) &= E_r^{\text{inf}}(\text{WS}) + E_r^{\text{inf}}(\mathbf{d}) + E_r^{\text{inf}}(\mathbf{f}) + E_r^{\text{inf}}(\mathbf{j}) + E_a(\mathbf{m}) \\ &= E_r^{\text{inf}}(\text{WS}) + 100 \text{ kJ} \cdot \text{mol}^{-1} \end{aligned}$$

Hence, the water splitting reaction must be exothermic, $E_r^{\text{inf}} = -9 \text{ kJ mol}^{-1}$, for the two pathways to have effective rate-determining barriers of equal height. As there is no study that reported an exothermic reaction for water dissociation on Pt surfaces, also not in the bulk, the decarbonylation is the clear pathway favored on the flat (111) surface.

A similar analysis is also applied for the conversions on the stepped surface. The effective barrier of the decarbonylation pathway is 98 kJ mol^{-1} , again occurring prior to the WGS conversion at the C–C scission step. Three alternative routes were found for this pathway, two of which share the same rate-determining step. The barrier of these two steps are calculated for the routes with the rate determining step (\mathbf{m}') as

$$\begin{aligned} E_a^{\text{eff}}(\text{decarboxylation}) &= E_r^{\text{inf}}(\text{WS}) + E_r^{\text{inf}}(\mathbf{d}) + E_r^{\text{inf}}(\mathbf{f}) + E_r^{\text{inf}}(\mathbf{j}') + E_a(\mathbf{m}') \\ &= E_r^{\text{inf}}(\text{WS}) + E_r^{\text{inf}}(\mathbf{d}) + E_r^{\text{inf}}(\mathbf{h}') + E_r^{\text{inf}}(\mathbf{k}) + E_a(\mathbf{m}') \\ &= E_r^{\text{inf}}(\text{WS}) + 35 \text{ kJ} \cdot \text{mol}^{-1} \end{aligned}$$

Or for the route with rate determining step (\mathbf{i}')

$$\begin{aligned} E_a^{\text{eff}}(\text{decarboxylation}) &= E_r^{\text{inf}}(\text{WS}) + E_r^{\text{inf}}(\mathbf{d}) + E_r^{\text{inf}}(\mathbf{h}') + E_a(\mathbf{i}') \\ &= E_r^{\text{inf}}(\text{WS}) + 52 \text{ kJ} \cdot \text{mol}^{-1} \end{aligned}$$

As the aim is to determine how endothermic the water dissociation reaction can be for decarboxylation to have an effective rate-determining barrier at the similar height as decarbonylation, the route over reaction (\mathbf{m}') is considered. Thus, one calculates the endothermicity of the water dissociation reaction at $\sim 63 \text{ kJ mol}^{-1}$. From the values reported in Section 9.2.2 the lowest value calculated for this process is 12.5 kJ mol^{-1} .²¹¹ At such low

values of endothermicity, decarboxylation clearly dominates over decarbonylation. Figure 9.14 shows an adapted version of Figure 9.11 for this lowest value, where the change in water splitting reaction energy is also applied for the water splitting within the decarbonylation. At such a value of the reaction energy of water splitting, the effective barrier is 90 kJ mol^{-1} corresponding to the estimated barrier of water dissociation. At higher endothermicities, e.g., 71 kJ mol^{-1} , which is the highest value reported in Table 9.3,²⁵⁰ the rate-determining barriers along each path are still within 8 kJ mol^{-1} .

To summarize, the selectivity between the decarbonylation and decarboxylation on the stepped surface depends very much on the energetics of the water dissociation.

9.3.6. *Remarks on the effect of water as solvent on the reaction network*

All calculations performed in this part of the thesis ignore the effect of the water as solvent, and treat it only as a source for adsorbed hydroxyl groups on the surface within the reaction network. In the dehydrogenation of 1- and 2-propanol in Chapter 8 the effect of water as a solvent was investigated by employing a water layer consisting of eight water molecules around the reactants of the decisive step, propanal and acetone, to investigate their desorption trends in the presence of an aqueous medium. Chapter 9 of the thesis deals with several steps of equal importance in the reaction network apart from desorption of a couple of adsorbates. Solvent effects are ignored the effects in computational studies on the reaction thermodynamics and kinetics of reactions at solid/liquid interfaces^{206,263-265} as the current standard software cannot account for long-range solvent effects. However one should not totally dismiss the possible effects of the aqueous medium, as water is known to have a significant role as a reactant in aqueous phase processing.¹⁶ Therefore several aspects of having a water network around the adsorbed species that might be important are listed here.

- Experimental observation with addition of water: When one reacts 1-propanol on Pt(111) surface without any water in the system, less than 10% of the alcohol adsorbs dissociatively.²¹⁶ In the end of the reaction the adsorbed species are CO, H, C and CH₃C; only CO and H are observed in the gas phase along with the alcohol itself as CH₃C also dissociates at 450 K into adsorbed H and C where the latter deposits on the surface. On a surface pre-covered by oxygen the selectivity does not change, the hydrogen produced is converted into water and no other products are observed. These findings along with the products observed from 1-butanol conversion establish, in the absence of water, C–C bond scission occurs only at the bond closest to the C–O bond. In Besson's group,^{179,199,266} experiments were conducted on the conversion of primary and secondary alcohols on Pt/C at

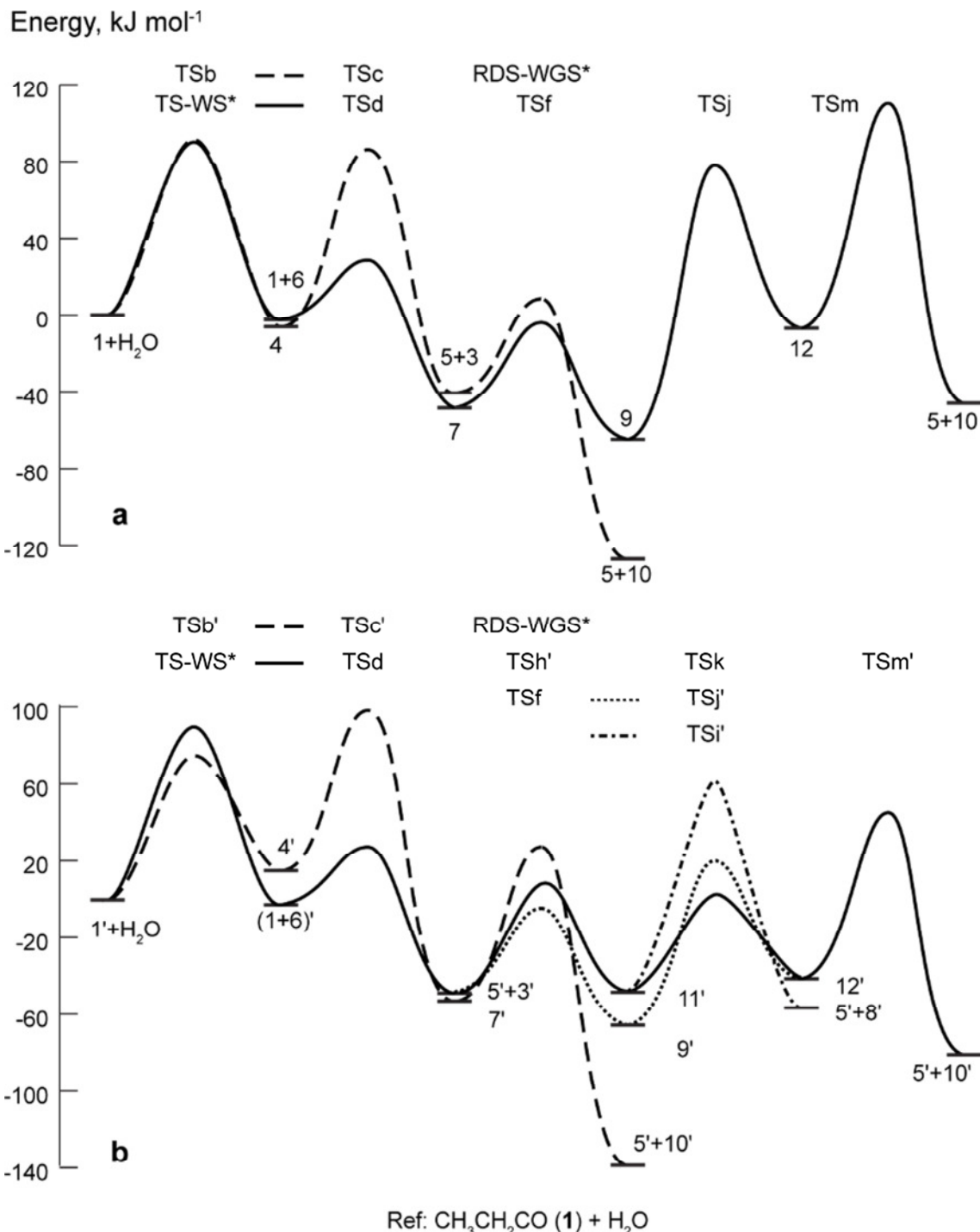


Figure 9.14 Alternative energy profiles when the water dissociation energy is taken at 12.5 kJ mol^{-1} (value from Ref. 208); cf. Figure 9.11.

normal air pressure. They used pure 1,4-dioxane as solvent and carried out supplementary experiments with water in the feed. When dioxane was the only solvent in the feed, the products of primary alcohols were the corresponding aldehydes which decarbonylated subsequently and secondary alcohols converted to the corresponding ketones. Addition of

water increased the activity of the catalyst, changing the selectivity of the primary alcohol to the corresponding carboxylic acid, but the ketone was still obtained in the case of the secondary alcohol.¹⁷⁹ Experiments with labeled oxygen also revealed that the source of the second O in the acid is water instead of the O₂ gas.²¹⁵ The presence of O₂ in the feed increases the amount of dissociation of water molecules on the surface, forming more OH groups adsorbed.²¹² Experiments by Lobo et al.,¹⁷⁸ done without oxygen in the feed, also indicate that propanal or propanol are not the source of the second O atom. The presence of CO groups also decreases the barrier of water dissociation on the surface,²⁰¹ however not as significantly as the presence of adsorbed O atoms.

The experimental data that this study is based on²⁵ were obtained in the absence of O₂ in the feed. Apart from 1-propanol, only water was present as a solvent and a reactant, otherwise approximately the same conditions were employed by Lobo et al.,¹⁷⁸ who have also included different supports for the Pt catalyst. As mentioned before, water has been identified as the source of the second oxygen. In the oxygenation of alcohols done by Besson's group, hydration of the aldehyde to a geminal diol is proposed, and the acid is formed afterwards from dehydrogenation of the said diol.²⁶⁶ Zope et al.²⁰¹ also considered the aldehyde as the molecule that OH inserts easily into on Pt(111). According to the present set of calculations, the conversion of the aldehyde, propanal, into the corresponding acyl, propionyl, was not only kinetically plausible, over a barrier of 11 kJ mol⁻¹; it was also thermodynamically very favorable, -74 kJ mol⁻¹.

Another important factor related to water dissociation is the different behavior of water on the flat and stepped surfaces. Árnadóttir²⁶⁷ recently reported that water dissociation on stepped Pt(221) surface is easier than on the flat surface; on the flat surface the reaction is 67 kJ mol⁻¹ endothermic over a barrier of 90 kJ mol⁻¹, on the stepped surface the reaction energy decreases to 20 kJ mol⁻¹ over a barrier of 80 kJ mol⁻¹. The calculations by Árnadóttir²⁶⁷ also show that water molecules adsorbed on the terrace are mobile; they tend to diffuse to step and kink sites. The calculations with a co-adsorbed O atom on the surface also showed that presence of the adsorbed O, which enhances water dissociation significantly on the flat surface, does not affect the barrier of the dissociation at the step sites but makes the conversion more favorable thermodynamically.

- Binding energies. The formation of H-bonding in the presence of a water network surrounding the molecules on the surfaces might lower the binding energies of some molecules and cause desorption, especially when the following conversions are higher in

energy. This is anticipated mostly for the intermediates that interact with the surface through oxygen atoms. In Section 8.3.3 it was shown that acetone, which is adsorbed on the surface through the O atom only in the gas phase (Section 8.1.3), loses interaction with the surface when there are water molecules present in the vicinity; the molecule is at a distance of 400 pm from the surface and connected to the water layer by a hydrogen bond of 168 pm length. This difference shows that the interaction with the water network stabilizes the molecule more than the interaction with the Pt surface. Chibani et al.¹⁹⁹ also reported similar stabilization effects of water on ethanol and 2-propanol adsorption, even via a single water molecule. One can expect a similar behavior for the intermediates **7** and **9**, where the major interactions are through the O atoms. Propionic acid **7** interacts weakly with the surface, BE = 39 kJ mol⁻¹. The acid has a dissociation constant pK_a of 4.87 at room temperature,²⁶⁸ this translates into a dissociation of ~0.5 % (assuming the concentration of the acid in solution is 0.5 M). Furthermore the experimental solvation energy of the acid is only 27 kJ mol⁻¹,²⁶⁹ i.e. quite similar to its binding energy. Thus, re-adsorption on the surface may be feasible and further conversion becomes possible. However if the acid does dissociate to propionate in the solution, it likely remains in solution. The solvation energy of this ion is higher, experimentally determined at 330 kJ mol⁻¹,²⁶⁹ than its binding energy on the surface, 232 kJ mol⁻¹. The dissociation product will be eventually re-protonated and observed as propionic acid.²⁵

- CO conversion via WGS. Water gas shift reaction converts CO that is strongly adsorbed on the surface into CO₂ and H₂ in the presence of water. In this reaction water does not act only as a solvent but it is also a reactant. The conversion of adsorbed CO into CO₂ is vital as the strong binding energy of CO on the surface blocks the surface sites, “poisoning” the catalyst.²⁴⁹ Especially at conditions of aqueous phase processing, the WGS reaction is very favorable.^{16,270} The experiments by Grabow et al.²⁵⁰ show that the favorable pathway via the intermediate COOH is facilitated when the amount of water in the feed is increased. These results support earlier experimental observations, which indicated that water has a promoter effect on WGS reaction over Pt(111)²⁷¹ and Pt/CeO₂.²⁷²

V. SUMMARY

In this thesis the transformations of hydrocarbons on transition metals as catalysts were explored employing methods based on density functional theory. The surfaces of the metals were described by periodic slab models. The close packed (111) surfaces of four transition metals – Pt, Pd, Rh, and Ni – and the stepped surface of one transition metal, Pt, were chosen as the catalyst models for exploring the reactions.

The first part of the thesis deals with systematic dehydrogenation of ethylene, which has been widely discussed as the simplest member of unsaturated hydrocarbons, on all four close-packed surfaces of the transition metals. In this part, the main concern was to explore how these four metals perform for the same reaction, most of the time with the same initial states and final states, in terms of geometry and reaction energetics. The dehydrogenation of the molecule was examined in a consecutive reaction and no alternative dehydrogenation mechanisms were explored; the C atom that is bonded to more H atoms was dehydrogenated first in the case of an odd number of H atoms. The set of model reactions included four dehydrogenation steps and one final C–C bond breaking: C_2H_4 (ethylene) \rightarrow C_2H_3 (vinyl) \rightarrow C_2H_2 (acetylene) \rightarrow C_2H (ethynyl) \rightarrow C_2 (carbon dimer) \rightarrow $\text{C} + \text{C}$. The dehydrogenation steps of ethylene and vinyl were found to be more facile than those of acetylene and ethynyl. Dehydrogenation reactions occur easier, both kinetically and thermodynamically, on Ni(111) and Rh(111) than on Pd(111) and Pt(111). C_2 decomposition is an exothermic process on Pd(111), Pt(111), and Rh(111), whereas the formation of C_2 , a precursor of graphene and coke, is kinetically and thermodynamically most plausible on Ni(111). The overall reaction to obtain two C atoms adsorbed on the surface is most exothermic on Rh(111), -53 kJ mol^{-1} , followed by Pd(111), -23 kJ mol^{-1} . On Ni(111) this overall conversion is thermoneutral, and on Pt(111) slightly endothermic, with energy changes of -3 kJ mol^{-1} and 12 kJ mol^{-1} , respectively. The highest overall barrier occurs in the C–C bond scission step on the surfaces studied here; the values calculated at 193 kJ mol^{-1} , 98 kJ mol^{-1} , 76 kJ mol^{-1} , and 68 kJ mol^{-1} on Pt(111), Pd(111), Rh(111), and Ni(111), respectively. The calculated results reveal trends of the binding energies (BE) of the species on the four metals in the order $\text{BE}(\text{C}_2\text{H}_4) < \text{BE}(\text{C}_2\text{H}_2) < \text{BE}(\text{C}_2\text{H}_3) < \text{BE}(\text{C}_2\text{H}) < \text{BE}(\text{C}_2) < \text{BE}(\text{C})$. The binding energies of ethylene and vinyl are largest on Pt(111) while other species with a lower hydrogen content exhibit the largest BE values on the surfaces Rh(111) and Ni(111).

The second part of the thesis deals with the conversion of simple alcohols, 1- and 2-propanol, on Pt surfaces. This conversion is presented in two different subsections. First the

dehydrogenation of two alcohols was examined to reveal differences in the reactivities, and then further conversion of adsorbed propionyl, the most stable product of 1-propanol dehydrogenation, was examined to clarify how the experimentally observed C–C bond scission products are being formed.

The dehydrogenation study was carried out only for the flat Pt surface. The experimental observation is rationalized as follows. 1-propanol undergoes C–C bond scission whereas 2-propanol desorbs after dehydrogenation reactions as acetone. Propanal and acetone are formed after the alcohols are dehydrogenated twice. The calculations revealed that different adsorption geometries on the surface for these two molecules are responsible for the unequal reactive behavior. The subsequent dehydrogenation of propanal forms a strongly adsorbed propionyl species over a low barrier, $E_a = 11 \text{ kJ mol}^{-1}$. In contrast, acetone adsorbs only weakly on the surface, BE = 18 kJ mol^{-1} , and the following dehydrogenation step exhibits a higher barrier, $E_a = 70 \text{ kJ mol}^{-1}$. These conclusions were confirmed by treating these two species, propanal and acetone, in a simple model of aqueous solution. Next, propionyl conversion into CO_2 and ethane was studied via C–C bond scission reactions of propionyl, its oxidized form propionic acid, and also their dehydrogenated intermediates. This study employs the flat surface as the reference surface whereas the Pt(221) surface was considered to include the effects of surface defects, the number of which increases significantly when the particle size of the catalyst decreases. The flat surface is active in decarbonylation reactions where the effective barrier is 91 kJ mol^{-1} . However higher barriers for decarboxylation reactions, ranging from 129 kJ mol^{-1} to 219 kJ mol^{-1} , make this latter pathway less likely. These high barriers are either due to a lack of stabilization by the surface at the transition state or due to a long initial distance between the dissociating atom and the surface. The (221) stepped surface provides terraces separated by monoatomic height steps to stabilize the species further at the surface and adsorb the intermediates so that the initial distances are reduced. Thus, the high barriers due to geometrical disadvantages are reduced to accessible levels. The highest barrier, 86 kJ mol^{-1} , was determined for the elementary reaction of C–C bond scission of 1,1-propendiolate along the decarboxylation route, making decarboxylation competitive with decarbonylation. A key point in this selectivity is, however, the energetics of the water dissociation on the surface or in the bulk producing OH groups. Depending on the reaction energy and the barrier of water dissociation on Pt surfaces, the preferred C–C bond scission route changes. According to the calculations presented in this work, C–C bond scission proceeds via decarboxylation only when the water dissociation

reaction is exothermic on the flat surface and at most 63 kJ mol^{-1} endothermic on the stepped surface.

The current thesis answers some of the important questions regarding the reaction network of C–C bond scission reactions on Pt surfaces. However, as the first part of the thesis advocates, various metals have different selectivities towards the same reactions. Hence, the mechanisms on other transition metals may feature different preferred reactions, such as C–O bond scissions, and may be governed by other routes. As the coverage of some of the intermediates in the conversion of simple alcohols is an important factor, kinetic studies of the reaction mechanisms may be valuable to assess better the governing mechanisms. Finally, as the experiments are carried out in aqueous phase, studying the adsorption and the reaction in solution with an improved computational strategy would provide more insights to the experimental findings. Thus, an adequate solvation model would be beneficial for treating the reactions on these surfaces.

APPENDIX A Microkinetic modeling

The rate r of a unimolecular reaction of a reactant adsorbed on the surface is given as

$$r = -\frac{d[\mathbf{R}]}{dt} = k\theta_{\mathbf{R}}[*] \quad (\text{A.1})$$

where $[\mathbf{R}]$ is the surface concentration of species \mathbf{R} , k is the rate constant for the reaction, $\theta_{\mathbf{R}}$ is the surface coverage of the reactant species \mathbf{R} and $[*]$ is the total number of sites available on the surface. The temperature dependency of the rate constant k of reaction (i) is given by the Arrhenius equation

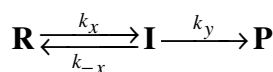
$$k_i = A_0(i) \exp\left(-\frac{E_a(i)}{RT}\right) \quad (\text{A.2})$$

with gas constant R and the temperature T and the pre-exponential factor A_0 defined as

$$A_0(i) = \frac{RT}{N_A h} \exp\left(\frac{\Delta S^{0\ddagger}(i)}{R}\right) \quad (\text{A.3})$$

where $\Delta S^{0\ddagger}(i)$ is the entropy difference between the transition state of reaction (i) and the initial state (i) and N_A is the Avogadro constant.

To support the claim that the effective barriers can be used for reactions involving an metastable intermediate one can consider the kinetics of a two-step reaction that converts reactant species \mathbf{R} to product species \mathbf{P} via intermediate \mathbf{I} :



with forward activation barriers $E_a(x)$ and $E_a(y)$. The rate of the conversion of \mathbf{R} into \mathbf{P} in steady-state is obtained from Eq.(A.1) by

$$r = \frac{k_x k_y}{k_{-x} + k_y} \theta_{\mathbf{R}}[*] \quad (\text{A.4})$$

If \mathbf{I} is an metastable intermediate the reverse reaction barrier $E_a(-x)$ is low, and according to Arrhenius equation, Eq. (A.2), k_{-x} is much bigger than k_y . Hence one may assume $k_{-x} + k_y \approx k_{-x}$. Therefore the reaction rate in Eq.(A.4) can be approximated as

$$r = \frac{k_x k_y}{k_{-x}} \theta_{\mathbf{R}}[*] = k^{eff} \theta_{\mathbf{R}}[*] \quad (\text{A.5})$$

Then Eq.(A.2) is invoked to calculate effective rate constant for the route from the ratio of the rate constants in Eq. (A.5).

$$k^{eff} = \frac{A_0(\mathbf{x})A_0(\mathbf{y})}{A_0(-\mathbf{x})} \exp\left[\frac{-E_a(\mathbf{x}) - E_a(\mathbf{y}) + E_a(-\mathbf{x})}{RT} \right] = A_0^{eff}(\mathbf{x}) \exp\left[-\frac{E_r(\mathbf{x}) + E_a(\mathbf{y})}{RT} \right] \quad (\text{A.6})$$

The effective pre-exponential factor, A_0^{eff} , is then

$$A_0^{eff}(\mathbf{x}) = \frac{RT}{N_A h} \exp\left(\frac{\Delta S^{0^\ddagger eff}(\mathbf{x})}{R} \right) \quad (\text{A.7})$$

where the difference in the entropies are calculated from the transition state with the adjusted barrier height and the stable initial state as shown in Eq.(A.8)

$$\Delta S^{0^\ddagger eff}(\mathbf{x}) = S(TS\mathbf{y}) - S(IS\mathbf{x}) \quad (\text{A.8})$$

The term in the exponential in Eq.(A.6) is defined in Section 9.3.4 as the effective activation barrier E_a^{eff} of the route.

The vibrational contribution to entropy of a molecular structure at temperature T is given by

$$\frac{S_{vib}}{R} = \sum \left(\frac{\Theta_{v,p}/T}{\exp(\Theta_{v,p}/T) - 1} - \ln \left[1 - \exp(-\Theta_{v,p}/T) \right] \right) \quad (\text{A.9})$$

where the characteristic temperature $\Theta_{v,p} = h\nu/k_B$ is obtained from the frequency n_p of vibrational mode p . The vibrational modes of **TSi'** and **TSm'** are given in Table 9.4.

REFERENCES

- (1) *BP Statistical Review of World Energy June 2012*; BP, bp.com/statisticalreview, **2012**
- (2) Shafiee, S.; Topal, E. *Energy Policy* **2009**, *37*, 181.
- (3) UNSD Demographic Statistics, *Demographic Yearbook*, available from United Nations Statistics Division, <http://unstats.un.org/unsd/demographic/products/dyb/dybcensusdata.htm> (accessed May 21st, 2013).
- (4) ERICTA, C. N. *The 2010 Census of Population and Housing Reveals the Philippine Population at 92.34 Million*, available from National Statistics Office, Republic of Philippines, <http://www.census.gov.ph/content/2010-census-population-and-housing-reveals-philippine-population-9234-million> (accessed May 21st, 2013).
- (5) *Zeitreihen zur Entwicklung der erneuerbaren Energien in Deutschland*; Bundesministerium für Umwelt, Naturschutz und Reaktorsicherheit - Federal Ministry for the Environment, Nature Conservation and Nuclear Safety http://www.erneuerbare-energien.de/erneuerbare_energien/datenservice/zeitreihen/doc/45919.php, **2012**
- (6) *Renewable Energy Sources in Figures: National and International Development*; Bundesministerium für Umwelt, Naturschutz und Reaktorsicherheit - Federal Ministry for the Environment, Nature Conservation and Nuclear Safety Berlin, http://www.erneuerbare-energien.de/english/renewable_energy/data_service/renewable_energy_in_figures/doc/5996.php, **2011**
- (7) Lynd, L. R.; Wyman, C. E.; Gerngross, T. U. *Biotechnol. Prog.* **1999**, *15*, 777.
- (8) Fernandes, S. D.; Trautmann, N. M.; Streets, D. G.; Roden, C. A.; Bond, T. C. *Global Biogeochem. Cycles* **2007**, *21*, GB2019.
- (9) *Energy Units*, available from American Physical Society Sites, <http://www.aps.org/policy/reports/popa-reports/energy/units.cfm> (accessed March 20th, 2013).
- (10) Seveda, M. S.; Rathore, N. S.; Kumar, V. In *Handbook of Renewable Energy Technology*; Zobaa, A. F., Bansal, R. C., Eds.; World Scientific Singapore, 2011, p 323.
- (11) Huber, G. W.; Dumesic, J. A. *Catal. Today* **2006**, *111*, 119.
- (12) Field, C. B.; Campbell, J. E.; Lobell, D. B. *Trends Ecol. Evol.* **2008**, *23*, 65.
- (13) Rostrup-Nielsen, J. R. *Phys. Chem. Chem. Phys.* **2001**, *3*, 283.

- (14) Modell, M. In *Fundamentals of Thermochemical Biomass Conversion*; Overend, R. P., Milne, T. A., Mudge, L. K., Eds.; Springer Netherlands 1985, p 95.
- (15) Milne, T. A.; Elam, C. C.; Evans, R. J. *Hydrogen from Biomass: State of the Art and Research Challenges*; National Renewable Energy Laboratory: Golden, CO, **2002** -and the references therein.
- (16) Cortright, R. D.; Davda, R. R.; Dumesic, J. A. *Nature* **2002**, *418*, 964.
- (17) Davda, R. R.; Shabaker, J. W.; Huber, G. W.; Cortright, R. D.; Dumesic, J. A. *Appl. Catal., B* **2005**, *56*, 171.
- (18) Moskaleva, L. V.; Chen, Z.-X.; Aleksandrov, H. A.; Mohammed, A. B.; Sun, Q.; Rösch, N. *J. Phys. Chem. C* **2009**, *113*, 2512.
- (19) Li, M.; Guo, W.; Jiang, R.; Zhao, L.; Lu, X.; Zhu, H.; Fu, D.; Shan, H. *J. Phys. Chem. C* **2010**, *114*, 8440.
- (20) Moskaleva, L. V.; Aleksandrov, H. A.; Basaran, D.; Zhao, Z.-J.; Rösch, N. *J. Phys. Chem. C* **2009**, *113*, 15373.
- (21) Zhao, Z.-J.; Moskaleva, L. V.; Aleksandrov, H. A.; Basaran, D.; Rösch, N. *J. Phys. Chem. C* **2010**, *114*, 12190.
- (22) Chen, Z.-X.; Aleksandrov, H. A.; Basaran, D.; Rösch, N. *J. Phys. Chem. C* **2010**, *114*, 17683.
- (23) Mei, D.; Sheth, P. A.; Neurock, M.; Smith, C. M. *J. Catal.* **2006**, *242*, 1.
- (24) Kozlov, S.; Yudanov, I. V.; Aleksandrov, H. A.; Rösch, N. *Phys. Chem. Chem. Phys.* **2009**, *11*, 10955.
- (25) Wawrzetz, A.; Peng, B.; Hrabar, A.; Jentys, A.; Lemonidou, A. A.; Lercher, J. A. *J. Catal.* **2010**, *269*, 411.
- (26) Kresse, G.; Furthmüller, J. *Comput. Mater. Sci.* **1996**, *6*, 15.
- (27) Kresse, G.; Hafner, J. *Phys. Rev. B: Condens. Matter Mater. Phys.* **1993**, *47*, 558.
- (28) Kresse, G.; Hafner, J. *Phys. Rev. B: Condens. Matter Mater. Phys.* **1994**, *49*, 14251.
- (29) Kresse, G.; Furthmüller, J. *Phys. Rev. B: Condens. Matter Mater. Phys.* **1996**, *54*, 11169.
- (30) Blöchl, P. E. *Phys. Rev. B: Condens. Matter Mater. Phys.* **1994**, *50*, 17953.
- (31) Kresse, G.; Joubert, D. *Phys. Rev. B: Condens. Matter Mater. Phys.* **1999**, *59*, 1758.

- (32) Perdew, J. P.; Chevary, J. A.; Vosko, S. H.; Jackson, K. A.; Pederson, M. R.; Singh, D. J.; Fiolhais, C. *Phys. Rev. B: Condens. Matter Mater. Phys.* **1992**, *46*, 6671.
- (33) Perdew, J. P.; Chevary, J. A.; Vosko, S. H.; Jackson, K. A.; Pederson, M. R.; Singh, D. J.; Fiolhais, C. *Phys. Rev. B: Condens. Matter Mater. Phys.* **1993**, *48*, 4978.
- (34) Monkhorst, H. J.; Pack, J. D. *Phys. Rev. B: Solid State* **1976**, *13*, 5188.
- (35) Methfessel, M.; Paxton, A. T. *Phys. Rev. B: Condens. Matter Mater. Phys.* **1989**, *40*, 3616.
- (36) Makov, G.; Payne, M. C. *Phys. Rev. B* **1995**, *51*, 4014.
- (37) Henkelman, G.; Jónsson, H. *J. Chem. Phys.* **1999**, *111*, 7010.
- (38) *Classical and Quantum Dynamics in Condensed Phase Simulations*; Jónsson, H.; Mills, G.; Jacobsen, K. W., Eds.; World Scientific: Singapore, 1998.
- (39) Mills, G.; Jónsson, H.; Schenter, G. K. *Surf. Sci.* **1995**, *324*, 305.
- (40) Nave, S.; Tiwari, A. K.; Jackson, B. *J. Chem. Phys.* **2010**, *132*, 054705.
- (41) Jeffrey, G. A. *An Introduction to Hydrogen Bonding*; Oxford University Press: New York, **1997**.
- (42) Wittcoff, H. A.; Reuben, B. G.; Plotkin, J. S. *Industrial Organic Chemicals*; John Wiley & Sons, Inc., **2012**.
- (43) Bond, G. C. *Metal-Catalysed Reactions of Hydrocarbons*; Springer: New York, **2005**.
- (44) Lang, B.; Joyner, R. W.; Somorjai, G. A. *Surf. Sci.* **1972**, *30*, 454.
- (45) Kesmodel, L. L.; Dubois, L. H.; Somorjai, G. A. *J. Chem. Phys.* **1979**, *70*, 2180.
- (46) Fernelius, C. W.; Wittcoff, H.; Varnerin, R. E. *J. Chem. Educ.* **1979**, *56*, 385.
- (47) Dubois, L. H.; Castner, D. G.; Somorjai, G. A. *J. Chem. Phys.* **1980**, *72*, 5234.
- (48) Kesmodel, L. L.; Gates, J. A. *Surf. Sci.* **1981**, *111*, L747.
- (49) Hills, M. M.; Parmeter, J. E.; Mullins, C. B.; Weinberg, W. H. *J. Am. Chem. Soc.* **1986**, *108*, 3554.
- (50) Zhu, X. Y.; White, J. M. *Surf. Sci.* **1989**, *214*, 240.
- (51) Dae Bok, K.; Anderson, A. B. *Surf. Sci.* **1985**, *155*, 639.
- (52) Marinova, T. S.; Kostov, K. L. *Surf. Sci.* **1987**, *181*, 573.
- (53) Ge, Q.; King, D. A. *J. Chem. Phys.* **1999**, *110*, 4699.

- (54) Mittendorfer, F.; Thomazeau, C.; Raybaud, P.; Toulhoat, H. *J. Phys. Chem. B* **2003**, *107*, 12287.
- (55) Vang, R. T.; Honkala, K.; Dahl, S.; Vestergaard, E. K.; Schnadt, J.; Lægsgaard, E.; Clausen, B. S.; Nørskov, J. K.; Besenbacher, F. *Surf. Sci.* **2006**, *600*, 66.
- (56) Neurock, M.; van Santen, R. A. *J. Phys. Chem. B* **2000**, *104*, 11127.
- (57) Ponec, V.; Bond, G. C. *Catalysis by Metals and Alloys*; Elsevier Science: Amsterdam, **1998**.
- (58) Bao, S.; Ph, H.; Schindler, K. M.; Fritzsche, V.; Bradshaw, A. M.; Woodruff, D. P.; Casado, C.; Asensio, M. C. *J. Phys.: Condens. Matter* **1994**, *6*, L93.
- (59) Zaera, F.; Janssens, T. V. W.; Öfner, H. *Surf. Sci.* **1996**, *368*, 371.
- (60) Stacchiola, D.; Azad, S.; Burkholder, L.; Tysoe, W. T. *J. Phys. Chem. B* **2001**, *105*, 11233.
- (61) Prentice, J. D.; Lesiunas, A.; Sheppard, N. *J. Chem. Soc., Chem. Commun.* **1976**, *0*, 76.
- (62) Ilbach, H.; Lehwald, S. *J. Vac. Sci. Technol.* **1978**, *15*, 407.
- (63) Krüger, B.; Benndorf, G. *Surf. Sci.* **1986**, *178*, 704.
- (64) Bent, B. E.; Mate, C. M.; Kao, C. T.; Slavin, A. J.; Somorjai, G. A. *J. Phys. Chem.* **1988**, *92*, 4720.
- (65) Raval, R. *Surf. Sci.* **1995**, *331–333, Part A*, 1.
- (66) Stacchiola, D.; Wu, G.; Kaltchev, M.; Tysoe, W. T. *Surf. Sci.* **2001**, *486*, 9.
- (67) Sock, M.; Eichler, A.; Surnev, S.; Andersen, J. N.; Klötzer, B.; Hayek, K.; Ramsey, M. G.; Netzer, F. P. *Surf. Sci.* **2003**, *545*, 122.
- (68) Zheng, T.; Stacchiola, D.; Poon, H. C.; Saldin, D. K.; Tysoe, W. T. *Surf. Sci.* **2004**, *564*, 71.
- (69) Cremer, P. S.; Su, X.; Shen, Y. R.; Somorjai, G. A. *J. Am. Chem. Soc.* **1996**, *118*, 2942.
- (70) Pallassana, V.; Neurock, M.; Lusvardi, V. S.; Lerou, J. J.; Kragten, D. D.; van Santen, R. A. *J. Phys. Chem. B* **2002**, *106*, 1656.
- (71) Andersin, J.; Lopez, N.; Honkala, K. *J. Phys. Chem. C* **2009**, *113*, 8278.
- (72) Okada, T.; Kim, Y.; Sainoo, Y.; Komeda, T.; Trenary, M.; Kawai, M. *J. Phys. Chem. Lett.* **2011**, *2*, 2263.
- (73) Hirschl, R.; Eichler, A.; Hafner, J. *J. Catal.* **2004**, *226*, 273.

- (74) Chen, Y.; Vlachos, D. G. *J. Phys. Chem. C* **2010**, *114*, 4973.
- (75) Pallassana, V.; Neurock, M. *J. Catal.* **2000**, *191*, 301.
- (76) Andersin, J.; Honkala, K. *Surf. Sci.* **2010**, *604*, 762.
- (77) Cremer, P.; Stanners, C.; Niemantsverdriet, J. W.; Shen, Y. R.; Somorjai, G. *Surf. Sci.* **1995**, *328*, 111.
- (78) Gates, J. A.; Kesmodel, L. L. *Surf. Sci.* **1983**, *124*, 68.
- (79) Koestner, R. J.; Van Hove, M. A.; Somorjai, G. A. *Surf. Sci.* **1982**, *121*, 321.
- (80) Papageorgopoulos, D. C.; Ge, Q.; King, D. A. *Surf. Sci.* **1998**, *397*, 13.
- (81) Bao, S.; Hofmann, P.; Schindler, K. M.; Fritzsch, V.; Bradshaw, A. M.; Woodruff, D. P.; Casado, C.; Asensio, M. C. *Surf. Sci.* **1994**, *307–309, Part B*, 722.
- (82) Aleksandrov, H. A.; Moskaleva, L. V.; Zhao, Z.-J.; Basaran, D.; Chen, Z.-X.; Mei, D.; Rösch, N. *J. Catal.* **2012**, *285*, 187.
- (83) Wang, L. P.; Tysoe, W. T.; Ormerod, R. M.; Lambert, R. M.; Hoffmann, H.; Zaera, F. *J. Phys. Chem.* **1990**, *94*, 4236.
- (84) Goda, A. M.; Bartea, M. A.; Chen, J. G. *J. Phys. Chem. B* **2006**, *110*, 11823.
- (85) Medlin, J. W.; Allendorf, M. D. *J. Phys. Chem. B* **2003**, *107*, 217.
- (86) Xu, J.; Saeys, M. *J. Phys. Chem. C* **2009**, *113*, 4099.
- (87) Bartholomew, C. H. *Appl. Catal., A* **2001**, *212*, 17.
- (88) Steininger, H.; Ibach, H.; Lehwald, S. *Surf. Sci.* **1982**, *117*, 685.
- (89) Lorenz, M. P. A.; Fuhrmann, T.; Streber, R.; Bayer, A.; Bebensee, F.; Gotterbarm, K.; Kinne, M.; Trankenschuh, B.; Zhu, J. F.; Papp, C.; Denecke, R.; Steinruck, H. P. *J. Chem. Phys.* **2010**, *133*, 014706.
- (90) Stöhr, J.; Sette, F.; Johnson, A. L. *Phys. Rev. Lett.* **1984**, *53*, 1684.
- (91) Watson, G. W.; Wells, R. P. K.; Willock, D. J.; Hutchings, G. J. *J. Phys. Chem. B* **2000**, *104*, 6439.
- (92) Watwe, R. M.; Cortright, R. D.; Mavrikakis, M.; Nørskov, J. K.; Dumesic, J. A. *J. Chem. Phys.* **2001**, *114*, 4663.
- (93) Ge, Q.; Neurock, M. *Chem. Phys. Lett.* **2002**, *358*, 377.

- (94) Essen, J. M.; Haubrich, J.; Becker, C.; Wandelt, K. *Surf. Sci.* **2007**, *601*, 3472.
- (95) Sheth, P. A.; Neurock, M.; Smith, C. M. *J. Phys. Chem. B* **2005**, *109*, 12449.
- (96) Shen, J.; Hill, J. M.; Watwe, R. M.; Spiewak, B. E.; Dumesic, J. A. *J. Phys. Chem. B* **1999**, *103*, 3923.
- (97) Jacob, T.; Goddard, W. A. *J. Phys. Chem. B* **2005**, *109*, 297.
- (98) Sesselmann, W.; Woratschek, B.; Ertl, G.; Küppers, J.; Haberland, H. *Surf. Sci.* **1983**, *130*, 245.
- (99) Baddeley, C. J.; Lee, A. F.; Lambert, R. M.; Giebel, T.; Schaff, O.; Fernandez, V.; Schindler, K. M.; Theobald, A.; Hirschmugl, C. J.; Lindsay, R.; Bradshaw, A. M.; Woodruff, D. P. *Surf. Sci.* **1998**, *400*, 166.
- (100) Matsumoto, C.; Kim, Y.; Okawa, T.; Sainoo, Y.; Kawai, M. *Surf. Sci.* **2005**, *587*, 19.
- (101) Gates, J. A.; Kesmodel, L. L. *J. Chem. Phys.* **1982**, *76*, 4281.
- (102) Lu, X.; Liu, L.; Li, Y.; Guo, W.; Zhao, L.; Shan, H. *Phys. Chem. Chem. Phys.* **2012**
- (103) Sheth, P. A.; Neurock, M.; Smith, C. M. *J. Phys. Chem. B* **2003**, *107*, 2009.
- (104) Mate, C. M.; Kao, C. T.; Bent, B. E.; Somorjai, G. A. *Surf. Sci.* **1988**, *197*, 183.
- (105) Casalone, G.; Cattania, M. G.; Merati, F.; Simonetta, M. *Surf. Sci.* **1982**, *120*, 171.
- (106) Viñes, F.; Neyman, K. M.; Görling, A. *J. Phys. Chem. A* **2009**, *113*, 11963.
- (107) Ford, D. C.; Xu, Y.; Mavrikakis, M. *Surf. Sci.* **2005**, *587*, 159.
- (108) Chen, Z.-X.; Neyman, K. M.; Lim, K. H.; Rösch, N. *Langmuir* **2004**, *20*, 8068.
- (109) Mavrikakis, M.; Rempel, J.; Greeley, J.; Hansen, L. B.; Nørskov, J. K. *J. Chem. Phys.* **2002**, *117*, 6737.
- (110) Isett, L. C.; Blakely, J. M. *Surf. Sci.* **1976**, *58*, 397.
- (111) Takeuchi, A.; Wise, H. *J. Phys. Chem.* **1983**, *87*, 5372.
- (112) Zhang, Q. M.; Wells, J. C.; Gong, X. G.; Zhang, Z. *Phys. Rev. B: Condens. Matter Mater. Phys.* **2004**, *69*, 205413.
- (113) Xu, J.; Saeys, M. *J. Catal.* **2006**, *242*, 217.
- (114) Klinke, D. J.; Wilke, S.; Broadbelt, L. J. *J. Catal.* **1998**, *178*, 540.
- (115) Cremer, P. S.; Su, X.; Shen, Y. R.; Somorjai, G. A. *J. Phys. Chem. B* **1997**, *101*, 6474.

- (116) Janssens, T. V. W.; Völkening, S.; Zambelli, T.; Wintterlin, J. *J. Phys. Chem. B* **1998**, *102*, 6521.
- (117) Ormerod, R. M.; Lambert, R. M.; Hoffmann, H.; Zaera, F.; Wang, L. P.; Bennett, D. W.; Tysoe, W. T. *J. Phys. Chem.* **1994**, *98*, 2134.
- (118) Brønsted, J. N. *Chem. Rev.* **1928**, *5*, 231.
- (119) Evans, M. G.; Polanyi, M. *Trans. Faraday Soc.* **1938**, *34*, 0011.
- (120) Rostrup-Nielsen, J. R.; Hansen, J. H. B. *J. Catal.* **1993**, *144*, 38.
- (121) Bengaard, H. S.; Nørskov, J. K.; Sehested, J.; Clausen, B. S.; Nielsen, L. P.; Molenbroek, A. M.; Rostrup-Nielsen, J. R. *J. Catal.* **2002**, *209*, 365.
- (122) Hammond, G. S. *J. Am. Chem. Soc.* **1955**, *77*, 334.
- (123) Michaelides, A.; Liu, Z. P.; Zhang, C. J.; Alavi, A.; King, D. A.; Hu, P. *J. Am. Chem. Soc.* **2003**, *125*, 3704.
- (124) Nørskov, J. K.; Bligaard, T.; Logadottir, A.; Bahn, S.; Hansen, L. B.; Bollinger, M.; Bengaard, H.; Hammer, B.; Sljivancanin, Z.; Mavrikakis, M.; Xu, Y.; Dahl, S.; Jacobsen, C. J. H. *J. Catal.* **2002**, *209*, 275.
- (125) Somorjai, G. A. *Introduction to Surface Chemistry and Catalysis*; first ed.; Wiley, John & Sons, Incorporated, **1994**.
- (126) Greeley, J.; Nørskov, J. K.; Mavrikakis, M. *Annu. Rev. Phys. Chem.* **2002**, *53*, 319.
- (127) Momirlan, M.; Veziroglu, T. N. *Int. J. Hydrogen Energy* **2005**, *30*, 795.
- (128) Murray, R. *Hydrogen as an energy carrier*,
<http://gasunie.eldoc.ub.rug.nl/root/1973/2038701/>, **1973**
- (129) *The Hydrogen Economy: Opportunities and Challenges*; 1st ed.; Ball, M.; Wietschel, M., Eds.; Cambridge University Press: Cambridge, 2009.
- (130) Klier, K. *Advances in Catalysis* **1982**, *31*, 243.
- (131) Van Der Laan, G. P.; Beenackers, A. A. C. M. *Catal. Rev.* **1999**, *41*, 255.
- (132) Tronconi, E.; Ferlazzo, N.; Forzatti, P.; Pasquon, I. *Industrial & Engineering Chemistry Research* **1987**, *26*, 2122.
- (133) Zona, K. *Fuel Cell Use in the Space Shuttle*, available from
http://www.nasa.gov/topics/technology/hydrogen/fc_shuttle.html (accessed January 30, 2013).

- (134) Züttel, A.; Remhof, A.; Borgschulte, A.; Friedrichs, O. *Philos. Trans. R. Soc., A* **2010**, *368*, 3329.
- (135) Nørskov, J. K.; Christensen, C. H. *Science* **2006**, *312*, 1322.
- (136) Energy Efficiency and Renewable Energy, *FCT Hydrogen Production: Current Technology*, available from U.S. Department of Energy,
http://www1.eere.energy.gov/hydrogenandfuelcells/production/current_technology.html (accessed July 23, 2012,
- (137) Ewan, B. C. R.; Allen, R. W. K. *Int. J. Hydrogen Energy* **2005**, *30*, 809.
- (138) Holladay, J. D.; Hu, J.; King, D. L.; Wang, Y. *Catal. Today* **2009**, *139*, 244, and references therein.
- (139) Navarro, R. M.; Peña, M. A.; Fierro, J. L. G. *Chem. Rev.* **2007**, *107*, 3952, and references therein.
- (140) Rostrup-Nielsen, J.; Rostrup-Nielsen, T. *CATTECH* **2002**, *6*, 150.
- (141) Kikuchi, E.; Tanaka, S.; Yamazaki, Y.; Morita, Y. *Bull. Jpn. Pet. Inst.* **1974**, *16*, 95.
- (142) Jones, G.; Jakobsen, J. G.; Shim, S. S.; Kleis, J.; Andersson, M. P.; Rossmeisl, J.; Abild-Pedersen, F.; Bligaard, T.; Helveg, S.; Hinnemann, B.; Rostrup-Nielsen, J. R.; Chorkendorff, I.; Sehested, J.; Nørskov, J. K. *J. Catal.* **2008**, *259*, 147.
- (143) Sehested, J.; Jacobsen, C. J. H.; Rokni, S.; Rostrup-Nielsen, J. R. *J. Catal.* **2001**, *201*, 206.
- (144) Claridge, J. B.; York, A. P. E.; Brungs, A. J.; Marquez-Alvarez, C.; Sloan, J.; Tsang, S. C.; Green, M. L. H. *J. Catal.* **1998**, *180*, 85.
- (145) Rostrup-Nielsen, J. R.; Christensen, T. S.; Dybkjaer, I. In *Studies in Surface Science and Catalysis*; Rao, T. S. R. P., Dhar, G. M., Eds.; Elsevier 1998; Vol. Volume 113, p 81.
- (146) Trimm, D. L.; Önsan, Z. I. *Catal. Rev.* **2001**, *43*, 31, and references therein.
- (147) Muradov, N. Z. *Energy Fuels* **1998**, *12*, 41.
- (148) Liszka, M.; Malik, T.; Manfrida, G. *Energy* **2012**, *45*, 142.
- (149) Turner, J. A. *Science* **2004**, *305*, 972.
- (150) Verne, J. *The Mysterious Island*, **1874** (available at
<http://www.gutenberg.org/files/1268/1268-h/1268-h.htm>, accessed January 30, 2013).

- (151) Badwal, S. P. S.; Giddey, S.; Munnings, C. *Hydrogen production via solid electrolytic routes*. **2012**, WIREs Energy Environ. doi: 10.1002/wene.50.
- (152) Bard, A. J.; Fox, M. A. *Acc. Chem. Res.* **1995**, 28, 141.
- (153) Khaselev, O.; Turner, J. A. *Science* **1998**, 280, 425.
- (154) Crabtree, G. W.; Dresselhaus, M. S.; Buchanan, M. V. *Phys. Today* **2004**, 57, 39.
- (155) Ni, M.; Leung, D. Y. C.; Leung, M. K. H.; Sumathy, K. *Fuel Process. Technol.* **2006**, 87, 461, and references therein.
- (156) Kaushik, N.; Debabrata, D. *Curr. Sci.* **2003**, 85, 265, and references therein.
- (157) *Roadmap for Bioenergy and Biobased Products in the United States*; ADA494661; Biomass Research and Development Technical Advisory Committee: WASHINGTON DC, <http://handle.dtic.mil/100.2/ADA494661>, **2007**
- (158) Demirbas, A. *Prog. Energy Combust. Sci.* **2004**, 30, 219.
- (159) Chheda, J. N.; Huber, G. W.; Dumesic, J. A. *Angew. Chem., Int. Ed.* **2007**, 46, 7164.
- (160) Prins, M. J.; Ptasinski, K. J.; Janssen, F. J. J. G. *Energy* **2007**, 32, 1248.
- (161) Michel, C.; Goltl, F.; Sautet, P. *Phys. Chem. Chem. Phys.* **2012**, 14, 15286.
- (162) Wang, D.; Czernik, S.; Chornet, E. *Energy Fuels* **1998**, 12, 19.
- (163) Davda, R. R.; Dumesic, J. A. *Angew. Chem., Int. Ed.* **2003**, 42, 4068.
- (164) Huber, G. W.; Shabaker, J. W.; Dumesic, J. A. *Science* **2003**, 300, 2075.
- (165) Huber, G. W.; Shabaker, J. W.; Evans, S. T.; Dumesic, J. A. *Appl. Catal., B* **2006**, 62, 226.
- (166) Shabaker, J. W.; Davda, R. R.; Huber, G. W.; Cortright, R. D.; Dumesic, J. A. *J. Catal.* **2003**, 215, 344.
- (167) Davda, R. R.; Shabaker, J. W.; Huber, G. W.; Cortright, R. D.; Dumesic, J. A. *Appl. Catal., B* **2003**, 43, 13.
- (168) Kunkes, E. L.; Soares, R. R.; Simonetti, D. A.; Dumesic, J. A. *Appl. Catal., B* **2009**, 90, 693.
- (169) Cortright, R. D.; Vollendorf, N. W.; Hornemann, C. C.; McMahon, S. P. (Virent, INC.). Catalysts and methods for reforming oxygenated compounds. US Patent 8,231,857 B2, July 31, 2012.

- (170) Pagliaro, M.; Rossi, M. *The Future of Glycerol: New Uses of a Versatile Raw Material*, **2008** (available at <http://dx.doi.org/10.1039/9781847558305>, accessed February 20, 2013).
- (171) King, D. L.; Zhang, L.; Xia, G.; Karim, A. M.; Heldebrant, D. J.; Wang, X.; Peterson, T.; Wang, Y. *Appl. Catal., B* **2010**, *99*, 206.
- (172) Peng, B.; Zhao, C.; Mejía-Centeno, I.; Fuentes, G. A.; Jentys, A.; Lercher, J. A. *Catal. Today* **2012**, *183*, 3.
- (173) Ciftci, A.; Peng, B.; Jentys, A.; Lercher, J. A.; Hensen, E. J. M. *Appl. Catal., A* **2012**, *431–432*, 113.
- (174) Soares, R. R.; Simonetti, D. A.; Dumesic, J. A. *Angew. Chem.* **2006**, *118*, 4086.
- (175) Zhou, C.-H.; Beltramini, J. N.; Fan, Y.-X.; Lu, G. Q. *Chem. Soc. Rev.* **2008**, *37*, 527.
- (176) Gong, C.; Du, J.; Cao, N.; Tsao, G. *Appl Biochem Biotechnol* **2000**, *84-86*, 543.
- (177) van den Brand, J.; Snijders, P. C.; Sloof, W. G.; Terryn, H.; de Wit, J. H. W. *J. Phys. Chem. B* **2004**, *108*, 6017.
- (178) Lobo, R.; Marshall, C. L.; Dietrich, P. J.; Ribeiro, F. H.; Akatay, C.; Stach, E. A.; Mane, A.; Lei, Y.; Elam, J.; Miller, J. T. *ACS Catal.* **2012**, *2*, 2316.
- (179) Frassoldati, A.; Pinel, C.; Besson, M. *Catal. Today* **2011**, *173*, 81.
- (180) Mavrikakis, M.; Bartea, M. A. *J. Mol. Catal. A: Chem.* **1998**, *131*, 135.
- (181) Shorthouse, L. J.; Roberts, A. J.; Raval, R. *Surf. Sci.* **2001**, *480*, 37.
- (182) Alcalá, R.; Greeley, J.; Mavrikakis, M.; Dumesic, J. A. *J. Chem. Phys.* **2002**, *116*, 8973.
- (183) Avery, N. R. *Surf. Sci.* **1983**, *125*, 771.
- (184) Vannice, M. A.; Erley, W.; Ibach, H. *Surf. Sci.* **1991**, *254*, 1.
- (185) Liu, Z. M.; Vannice, M. A. *Surf. Sci.* **1994**, *316*, 337.
- (186) Jeffery, E. L.; Mann, R. K.; Hutchings, G. J.; Taylor, S. H.; Willock, D. J. *Catal. Today* **2005**, *105*, 85.
- (187) Delbecq, F.; Sautet, P. *Surf. Sci.* **1993**, *295*, 353.
- (188) Vargas, A.; Bürgi, T.; Baiker, A. *J. Catal.* **2004**, *222*, 439.
- (189) Loffreda, D.; Delbecq, F.; Vigné, F.; Sautet, P. *J. Am. Chem. Soc.* **2006**, *128*, 1316.
- (190) Lu, J.; Behtash, S.; Heyden, A. *J. Phys. Chem. C* **2012**, *116*, 14328.

- (191) Lee, A. F.; Gawthrop, D. E.; Hart, N. J.; Wilson, K. *Surf. Sci.* **2004**, *548*, 200.
- (192) Medlin, J. W. In *Chemical and Biochemical Catalysis for Next Generation Biofuels*; Simmons, B., Ed.; The Royal Society of Chemistry 2011, p 33.
- (193) Rioux, R. M.; Vannice, M. A. *J. Catal.* **2005**, *233*, 147.
- (194) Jones, G. S.; Mavrikakis, M.; Bartheau, M. A.; Vohs, J. M. *J. Am. Chem. Soc.* **1998**, *120*, 3196.
- (195) Zhang, J.; Cao, X. M.; Hu, P.; Zhong, Z.; Borgna, A.; Wu, P. *J. Phys. Chem. C* **2011**, *115*, 22429.
- (196) Alcalá, R.; Mavrikakis, M.; Dumesic, J. A. *J. Catal.* **2003**, *218*, 178.
- (197) Greeley, J.; Mavrikakis, M. *J. Am. Chem. Soc.* **2004**, *126*, 3910.
- (198) Chiu, C.-c. *Density Functional Studies on Catalysis of Alcohols on Noble Metal Surfaces*. M.S. Thesis, Technische Universität München, 02 November 2010.
- (199) Chibani, S.; Michel, C.; Delbecq, F.; Pinel, C.; Besson, M. *Catal. Sci. Technol.* **2012**, *3*, 339.
- (200) Michel, C.; Auneau, F.; Delbecq, F.; Sautet, P. *ACS Catal.* **2011**, *1*, 1430.
- (201) Zope, B. N.; Hibbitts, D. D.; Neurock, M.; Davis, R. J. *Science* **2010**, *330*, 74.
- (202) Cao, D.; Lu, G. Q.; Wieckowski, A.; Wasileski, S. A.; Neurock, M. *J. Phys. Chem. B* **2005**, *109*, 11622.
- (203) Andersin, J.; Parkkinen, P.; Honkala, K. *J. Catal.* **2012**, *290*, 118.
- (204) Jacob, T.; Goddard, W. A. *ChemPhysChem* **2006**, *7*, 992.
- (205) Faheem, M.; Suthirakun, S.; Heyden, A. *J. Phys. Chem. C* **2012**
- (206) Liu, B.; Greeley, J. *J. Phys. Chem. C* **2011**, *115*, 19702.
- (207) Waghray, A.; Blackmond, D. G. *J. Phys. Chem.* **1993**, *97*, 6002.
- (208) Englisch, M.; Jentys, A.; Lercher, J. A. *J. Catal.* **1997**, *166*, 25.
- (209) Thiel, P. A.; Madey, T. E. *Surf. Sci. Rep.* **1987**, *7*, 211, and references therein.
- (210) Ogasawara, H.; Brena, B.; Nordlund, D.; Nyberg, M.; Pelmenschikov, A.; Pettersson, L. G. M.; Nilsson, A. *Phys. Rev. Lett.* **2002**, *89*, 276102.
- (211) Jacob, T.; Goddard, W. A. *J. Am. Chem. Soc.* **2004**, *126*, 9360.

- (212) Fisher, G. B.; Sexton, B. A. *Phys. Rev. Lett.* **1980**, *44*, 683.
- (213) Wang, J. G.; Hammer, B. *J. Phys. Chem.* **2006**, *124*, 184704.
- (214) Shavorskiy, A.; Gladys, M. J.; Held, G. *Phys. Chem. Chem. Phys.* **2008**, *10*, 6150.
- (215) Rottenberg, M.; Baertschi, P. *Helv. Chim. Acta* **1956**, *39*, 1973.
- (216) Sexton, B. A.; Rendulic, K. D.; Huges, A. E. *Surf. Sci.* **1982**, *121*, 181.
- (217) Davis, J. L.; Barreau, M. A. *Surf. Sci.* **1987**, *187*, 387.
- (218) Bond, G. C. *Surf. Sci.* **1985**, *156, Part 2*, 966.
- (219) Somorjai, G. A. *J. Phys. Chem.* **1990**, *94*, 1013.
- (220) Somorjai, G. A.; Van Hove, M. A.; Bent, B. E. *J. Phys. Chem.* **1988**, *92*, 973.
- (221) Hammer, B.; Nielsen, O. H.; Nørskov, J. K. *Catal. Lett.* **1997**, *46*, 31.
- (222) Zambelli, T.; Wintterlin, J.; Trost, J.; Ertl, G. *Science* **1996**, *273*, 1688.
- (223) Yudanov, I. V.; Genest, A.; Schauermann, S.; Freund, H.-J.; Rösch, N. *Nano Lett.* **2012**, *12*, 2134.
- (224) Nørskov, J. K.; Bligaard, T.; Hvolbaek, B.; Abild-Pedersen, F.; Chorkendorff, I.; Christensen, C. H. *Chem. Soc. Rev.* **2008**, *37*, 2163.
- (225) Zhao, Z.-J.; Moskaleva, L. V.; Rösch, N. *J. Catal.* **2012**, *285*, 124.
- (226) Ogletree, D. F.; Van Hove, M. A.; Somorjai, G. A. *Surf. Sci.* **1986**, *173*, 351.
- (227) Blackman, G. S.; Xu, M. L.; Ogletree, D. F.; Van Hove, M. A.; Somorjai, G. A. *Phys. Rev. Lett.* **1988**, *61*, 2352.
- (228) Steininger, H.; Lehwald, S.; Ibach, H. *Surf. Sci.* **1982**, *123*, 264.
- (229) Hopster, H.; Ibach, H. *Surf. Sci.* **1978**, *77*, 109.
- (230) Luo, J. S.; Tobin, R. G.; Lambert, D. K.; Fisher, G. B.; DiMaggio, C. L. *Surf. Sci.* **1992**, *274*, 53.
- (231) Stroscio, J. A.; Eigler, D. M. *Science* **1991**, *254*, 1319.
- (232) Pedersen, M. Ø.; Bocquet, M. L.; Sautet, P.; Lægsgaard, E.; Stensgaard, I.; Besenbacher, F. *Chem. Phys. Lett.* **1999**, *299*, 403.
- (233) Gajdoš, M.; Eichler, A.; Hafner, J. *J. Phys.: Condens. Matter* **2004**, *16*, 1141.

- (234) Feibelman, P. J.; Hammer, B.; Nørskov, J. K.; Wagner, F.; Scheffler, M.; Stumpf, R.; Watwe, R.; Dumesic, J. *J. Phys. Chem. B* **2000**, *105*, 4018.
- (235) Gil, A.; Clotet, A.; Ricart, J. M.; Kresse, G.; Garcia-Hernández, M.; Rösch, N.; Sautet, P. *Surf. Sci.* **2003**, *530*, 71.
- (236) Kresse, G.; Gil, A.; Sautet, P. *Phys. Rev. B* **2003**, *68*, 073401.
- (237) Mason, S. E.; Grinberg, I.; Rappe, A. M. *Phys. Rev. B* **2004**, *69*, 161401.
- (238) Doll, K. *Surf. Sci.* **2004**, *573*, 464.
- (239) Stroppa, A.; Termentzidis, K.; Paier, J.; Kresse, G.; Hafner, J. *Phys. Rev. B* **2007**, *76*, 195440.
- (240) Stroppa, A.; Kresse, G. *New J. Phys.* **2008**, *10*, 063020.
- (241) Abild-Pedersen, F.; Andersson, M. P. *Surf. Sci.* **2007**, *601*, 1747.
- (242) Luo, S.; Zhao, Y.; Truhlar, D. G. *J. Phys. Chem. Lett.* **2012**, *3*, 2975.
- (243) Michaelides, A.; Hu, P. *J. Phys. Chem.* **2001**, *114*, 513.
- (244) Lew, W.; Crowe, M. C.; Karp, E.; Lytken, O.; Farmer, J. A.; Árnadóttir, L. n.; Schoenbaum, C.; Campbell, C. T. *J. Phys. Chem. C* **2011**, *115*, 11586.
- (245) Bournel, F.; Laffon, C.; Parent, P.; Tourillon, G. *Surf. Sci.* **1996**, *350*, 60.
- (246) Bournel, F.; Laffon, C.; Parent, P.; Tourillon, G. *Surf. Sci.* **1996**, *359*, 10.
- (247) Graham, A. P. *J. Phys. Chem.* **2001**, *115*, 524.
- (248) Alavi, A.; Hu, P.; Deutsch, T.; Silvestrelli, P. L.; Hutter, J. *Phys. Rev. Lett.* **1998**, *80*, 3650.
- (249) Lemons, R. A. *J. Power Sources* **1990**, *29*, 251.
- (250) Grabow, L. C.; Gokhale, A. A.; Evans, S. T.; Dumesic, J. A.; Mavrikakis, M. *J. Phys. Chem. C* **2008**, *112*, 4608.
- (251) Henderson, M. A. *Surf. Sci. Rep.* **2002**, *46*, 1, and references therein.
- (252) Hodgson, A.; Haq, S. *Surf. Sci. Rep.* **2009**, *64*, 381, and references therein.
- (253) Phatak, A. A.; Delgass, W. N.; Ribeiro, F. H.; Schneider, W. F. *J. Phys. Chem. C* **2009**, *113*, 7269.
- (254) Michaelides, A.; Hu, P. *J. Am. Chem. Soc.* **2001**, *123*, 4235.

- (255) Geissler, P. L.; Dellago, C.; Chandler, D.; Hutter, J.; Parrinello, M. *Science* **2001**, *291*, 2121.
- (256) Karp, E. M.; Campbell, C. T.; Studt, F.; Abild-Pedersen, F.; Nørskov, J. K. *J. Phys. Chem. C* **2012**, *116*, 25772.
- (257) Holzapfel, W. B. *J. Phys. Chem.* **1969**, *50*, 4424.
- (258) Avery, N. R. *J. Vac. Sci. Technol.* **1982**, *20*, 592.
- (259) Davis, J. L.; Barreau, M. A. *Langmuir* **1989**, *5*, 1299.
- (260) Firment, L. E.; Somorjai, G. A. *J. Vac. Sci. Technol.* **1980**, *17*, 574.
- (261) Murdoch, J. R. *J. Chem. Educ.* **1981**, *58*, 32.
- (262) Laidler, K. J. *Chemical Kinetics*; third ed.; Harper Collins: New York, **1987**.
- (263) Coll, D.; Delbecq, F.; Aray, Y.; Sautet, P. *Phys. Chem. Chem. Phys.* **2011**, *13*, 1448.
- (264) Ferrin, P.; Simonetti, D.; Kandoi, S.; Kunkes, E.; Dumesic, J. A.; Nørskov, J. K.; Mavrikakis, M. *J. Am. Chem. Soc.* **2009**, *131*, 5809.
- (265) Chen, Y.; Salciccioli, M.; Vlachos, D. G. *J. Phys. Chem. C* **2011**, *115*, 18707.
- (266) Korovchenko, P.; Donze, C.; Gallezot, P.; Besson, M. *Catal. Today* **2007**, *121*, 13.
- (267) Árnadóttir, L. In *ECS Meeting Abstracts* Honolulu, Hawaii, 2012; Vol. MA2012-02, p 3765, <http://ma.ecsdl.org/content/MA2012-02/54/3765.abstract>.
- (268) Stark, J. G.; Wallace, H. G. *Chemistry Data Book*; 2nd ed.; John Murray: London, **2001**.
- (269) Jayaram, B.; Sprous, D.; Beveridge, D. L. *J. Phys. Chem. B* **1998**, *102*, 9571.
- (270) Grenoble, D. C.; Estadt, M. M.; Ollis, D. F. *J. Catal.* **1981**, *67*, 90.
- (271) Bergeld, J.; Kasemo, B.; Chakarov, D. V. *Surf. Sci.* **2001**, *495*, L815.
- (272) Luengnaruemitchai, A.; Osuwan, S.; Gulari, E. *Catalysis Communications* **2003**, *4*, 215.